2007

Measurements of inclusive *W* and *Z* cross sections in *pp* collisions at √ s = 1.96TeV

A. Abulenci
University of Illinois at Urbana-Champaign

Kenneth A. Bloom
University of Nebraska-Lincoln, kbloom2@unl.edu

CDF Collaboration

J. Phys. G: Nucl. Part. Phys. **34** (2007) 2457–2544 doi:10.1088/0954-3899/34/12/001

Measurements of inclusive W and Z cross sections in $p\bar{p}$ collisions at $\sqrt{s} = 1.96$ TeV

A Abulencia[1], D Acosta[2], J Adelman[3], T Affolder[4], T Akimoto[5], M G Albrow[6], D Ambrose[6], S Amerio[7], D Amidei[8], A Anastassov[9], K Anikeev[6], A Annovi[10], J Antos[11], M Aoki[5], G Apollinari[6], J-F Arguin[12,13], T Arisawa[14], A Artikov[15], W Ashmanskas[6], A Attal[16], F Azfar[17], P Azzi-Bacchetta[7], P Azzurri[10], N Bacchetta[7], H Bachacou[18], W Badgett[6], A Barbaro-Galtieri[18], V E Barnes[19], B A Barnett[20], S Baroiant[21], V Bartsch[22], G Bauer[23], F Bedeschi[10], S Behari[20], S Belforte[24], G Bellettini[10], J Bellinger[25], A Belloni[23], E Ben-Haim[6], D Benjamin[26], A Beretvas[6], J Beringer[18], T Berry[27], A Bhatti[28], M Binkley[6], D Bisello[7], M Bishai[6], R E Blair[29], C Blocker[30], K Bloom[8], B Blumenfeld[20], A Bocci[28], A Bodek[31], V Boisvert[31], G Bolla[19], A Bolshov[23], D Bortoletto[19], J Boudreau[32], S Bourov[6], A Boveia[4], B Brau[4], C Bromberg[33], E Brubaker[3], J Budagov[15], H S Budd[31], S Budd[1], K Burkett[6], G Busetto[7], P Bussey[34], K L Byrum[29], S Cabrera[26], M Campanelli[35], M Campbell[8], F Canelli[16], A Canepa[19], D Carlsmith[25], R Carosi[10], S Carron[26], M Casarsa[24], A Castro[36], P Catastini[10], D Cauz[24], M Cavalli-Sforza[37], A Cerri[18], L Cerrito[17], S H Chang[38,39,40], J Chapman[8], Y C Chen[11], M Chertok[21], G Chiarelli[10], G Chlachidze[15], F Chlebana[6], I Cho[38,39,40], K Cho[38,39,40], D Chokheli[15], J P Chou[41], P H Chu[1], S H Chuang[25], K Chung[42], W H Chung[25], Y S Chung[31], M Ciljak[10], C I Ciobanu[1], M A Ciocci[10], A Clark[35], D Clark[30], M Coca[26], A Connolly[18], M E Convery[28], J Conway[21], B Cooper[22], K Copic[8], M Cordelli[43], G Cortiana[7], A Cruz[2], J Cuevas[44], R Culbertson[6], D Cyr[25], S DaRonco[7], S D'Auria[34], M D'onofrio[35], D Dagenhart[30], P de Barbaro[31], S De Cecco[45], A Deisher[18], G De Lentdecker[31], M Dell'Orso[10], S Demers[31], L Demortier[28], J Deng[26], M Deninno[36], D De Pedis[45], P F Derwent[6], C Dionisi[45], J Dittmann[46], P DiTuro[9], C Dörr[47], A Dominguez[18], S Donati[10], M Donega[35], P Dong[16], J Donini[7], T Dorigo[7], S Dube[9], K Ebina[14], J Efron[48], J Ehlers[35], R Erbacher[21], D Errede[1], S Errede[1], R Eusebi[31], H C Fang[18], S Farrington[27], I Fedorko[10], W T Fedorko[3], R G Feild[49], M Feindt[47], J P Fernandez[19], R Field[2], G Flanagan[33], L R Flores-Castillo[32], A Foland[41], S Forrester[21], G W Foster[6], M Franklin[41], J C Freeman[18], Y Fujii[50], I Furic[3], A Gajjar[27], M Gallinaro[28], J Galyardt[42], J E Garcia[10], M Garcia Sciverez[18], A F Garfinkel[19], C Gay[49], H Gerberich[1], E Gerchtein[42], D Gerdes[8], S Giagu[45], P Giannetti[10], A Gibson[18], K Gibson[42], C Ginsburg[6], K Giolo[19], M Giordani[24], M Giunta[10], G Giurgiu[42], V Glagolev[15], D Glenzinski[6], M Gold[51], N Goldschmidt[8], J Goldstein[17], G Gomez[44], G Gomez-Ceballos[44], M Goncharov[52], O González[19], I Gorelov[51], A T Goshaw[26], Y Gotra[32], K Goulianos[28], A Gresele[7],

M Griffiths[27], S Grinstein[41], C Grosso-Pilcher[3], U Grundler[1], J Guimaraes da Costa[41], C Haber[18], S R Hahn[6], K Hahn[53], E Halkiadakis[31], A Hamilton[12,13], B-Y Han[31], R Handler[25], F Happacher[43], K Hara[5], M Hare[54], S Harper[17], R F Harr[55], R M Harris[6], K Hatakeyama[28], J Hauser[16], C Hays[26], H Hayward[27], A Heijboer[53], B Heinemann[27], J Heinrich[53], M Hennecke[47], M Herndon[25], J Heuser[47], D Hidas[26], C S Hill[4], D Hirschbuehl[47], A Hocker[6], A Holloway[41], S Hou[11], M Houlden[27], S-C Hsu[56], B T Huffman[17], R E Hughes[48], J Huston[33], K Ikado[14], J Incandela[4], G Introzzi[10], M Iori[45], Y Ishizawa[5], A Ivanov[21], B Iyutin[23], E James[6], D Jang[9], B Jayatilaka[8], D Jeans[45], H Jensen[6], E J Jeon[38,39,40], M Jones[19], K K Joo[38,39,40], S Y Jun[42], T R Junk[1], T Kamon[52], J Kang[8], M Karagoz-Unel[57], P E Karchin[55], Y Kato[58], Y Kemp[47], R Kephart[6], U Kerzel[47], V Khotilovich[52], B Kilminster[48], D H Kim[38,39,40], H S Kim[38,39,40], J E Kim[38,39,40], M J Kim[42], M S Kim[38,39,40], S B Kim[38,39,40], S H Kim[5], Y K Kim[3], M Kirby[26], L Kirsch[30], S Klimenko[2], M Klute[23], B Knuteson[23], B R Ko[26], H Kobayashi[5], K Kondo[14], D J Kong[38,39,40], J Konigsberg[2], A Korytov[2], A V Kotwal[26], A Kovalev[53], J Kraus[1], I Kravchenko[23], M Kreps[47], A Kreymer[6], J Kroll[53], N Krumnack[46], M Kruse[26], V Krutelyov[52], S E Kuhlmann[29], Y Kusakabe[14], S Kwang[3], A T Laasanen[19], S Lai[12,13], S Lami[28], S Lami[28], S Lammel[6], M Lancaster[22], R L Lander[21], K Lannon[48], A Lath[9], G Latino[10], I Lazzizzera[7], C Lecci[47], T LeCompte[29], J Lee[31], J Lee[31], S W Lee[52], R Lefèvre[37], N Leonardo[23], S Leone[10], S Levy[3], J D Lewis[6], K Li[49], C Lin[49], C S Lin[6], M Lindgren[6], E Lipeles[56], T M Liss[1], A Lister[35], D O Litvintsev[6], T Liu[6], Y Liu[35], N S Lockyer[53], A Loginov[59], M Loreti[7], P Loverre[45], R-S Lu[11], D Lucchesi[7], P Lujan[18], P Lukens[6], G Lungu[2], L Lyons[17], J Lys[18], R Lysak[11], E Lytken[19], P Mack[47], D MacQueen[12,13], R Madrak[6], K Maeshima[6], P Maksimovic[20], G Manca[27], F Margaroli[36], R Marginean[6], C Marino[1], A Martin[49], M Martin[20], V Martin[57], M Martínez[37], T Maruyama[5], H Matsunaga[5], M E Mattson[55], R Mazini[12,13], P Mazzanti[36], K S McFarland[31], D McGivern[22], P McIntyre[52], P McNamara[9], R McNulty[27], A Mehta[27], S Menzemer[23], A Menzione[10], P Merkel[19], C Mesropian[28], A Messina[45], M von der Mey[16], T Miao[6], N Miladinovic[30], J Miles[23], R Miller[33], J S Miller[8], C Mills[4], M Milnik[47], R Miquel[18], S Miscetti[43], G Mitselmakher[2], A Miyamoto[50], N Moggi[36], B Mohr[16], R Moore[6], M Morello[10], P Movilla Fernandez[18], J Mülmenstädt[18], A Mukherjee[6], M Mulhearn[23], Th Muller[47], R Mumford[20], P Murat[6], J Nachtman[6], S Nahn[49], I Nakano[60], A Napier[54], D Naumov[51], V Necula[2], C Neu[53], M S Neubauer[56], J Nielsen[18], T Nigmanov[32], L Nodulman[29], O Norniella[37], T Ogawa[14], S H Oh[26], Y D Oh[38,39,40], T Okusawa[58], R Oldeman[27], R Orava[61], K Osterberg[61], C Pagliarone[10], E Palencia[44], R Paoletti[10], V Papadimitriou[6], A Papikonomou[47], A A Paramonov[3], B Parks[48], S Pashapour[12,13], J Patrick[6], G Pauletta[24], M Paulini[42], C Paus[23], D E Pellett[21], A Penzo[24], T J Phillips[26], G Piacentino[10], J Piedra[44], K Pitts[1], C Plager[16], L Pondrom[25], G Pope[32], X Portell[37], O Poukhov[15], N Pounder[17], F Prakoshyn[15], A Pronko[6], J Proudfoot[29], F Ptohos[43], G Punzi[10], J Pursley[20], J Rademacker[17], A Rahaman[32],

A Rakitin[23], S Rappoccio[41], F Ratnikov[9], B Reisert[6], V Rekovic[51], N van Remortel[61], P Renton[17], M Rescigno[45], S Richter[47], F Rimondi[36], K Rinnert[47], L Ristori[10], W J Robertson[26], A Robson[34], T Rodrigo[44], E Rogers[1], S Rolli[54], R Roser[6], M Rossi[24], R Rossin[2], C Rott[19], A Ruiz[44], J Russ[42], V Rusu[3], D Ryan[54], H Saarikko[61], S Sabik[12,13], A Safonov[21], W K Sakumoto[31], G Salamanna[45], O Salto[37], D Saltzberg[16], C Sanchez[37], L Santi[24], S Sarkar[45], K Sato[5], P Savard[12,13], A Savoy-Navarro[6], T Scheidle[47], P Schlabach[6], E E Schmidt[6], M P Schmidt[49], M Schmitt[57], T Schwarz[8], L Scodellaro[44], A L Scott[4], A Scribano[10], F Scuri[10], A Sedov[19], S Seidel[51], Y Seiya[58], A Semenov[15], F Semeria[36], L Sexton-Kennedy[6], I Sfiligoi[43], M D Shapiro[18], T Shears[27], P F Shepard[32], D Sherman[41], M Shimojima[5], M Shochet[3], Y Shon[25], I Shreyber[59], A Sidoti[10], P Sinervo[12,13], A Sisakyan[15], J Sjolin[17], A Skiba[47], A J Slaughter[6], K Sliwa[54], D Smirnov[51], J R Smith[21], F D Snider[6], R Snihur[12,13], M Soderberg[8], A Soha[21], S Somalwar[9], V Sorin[33], J Spalding[6], F Spinella[10], P Squillacioti[10], M Stanitzki[49], A Staveris-Polykalas[10], R St Denis[34], B Stelzer[16], O Stelzer-Chilton[12,13], D Stentz[57], J Strologas[51], D Stuart[4], J S Suh[38,39,40], A Sukhanov[2], K Sumorok[23], H Sun[54], T Suzuki[5], A Taffard[1], R Tafirout[12,13], R Takashima[60], Y Takeuchi[5], K Takikawa[5], M Tanaka[29], R Tanaka[60], M Tecchio[8], P K Teng[11], K Terashi[28], S Tether[23], J Thom[6], A S Thompson[34], E Thomson[53], P Tipton[31], V Tiwari[42], S Tkaczyk[6], D Toback[52], K Tollefson[33], T Tomura[5], D Tonelli[10], M Tönnesmann[33], S Torre[10], D Torretta[6], S Tourneur[6], W Trischuk[12,13], R Tsuchiya[14], S Tsuno[60], N Turini[10], F Ukegawa[5], T Unverhau[34], S Uozumi[5], D Usynin[53], L Vacavant[18], A Vaiciulis[31], S Vallecorsa[35], A Varganov[8], E Vataga[51], G Velev[6], G Veramendi[1], V Veszpremi[19], T Vickey[1], R Vidal[6], I Vila[44], R Vilar[44], I Vollrath[12,13], I Volobouev[18], F Würthwein[56], P Wagner[52], R G Wagner[29], R L Wagner[6], W Wagner[47], R Wallny[16], T Walter[47], Z Wan[9], M J Wang[11], S M Wang[2], A Warburton[12,13], B Ward[34], S Waschke[34], D Waters[22], T Watts[9], M Weber[18], W C Wester III[6], B Whitehouse[54], D Whiteson[53], A B Wicklund[29], E Wicklund[6], H H Williams[53], P Wilson[6], B L Winer[48], P Wittich[53], S Wolbers[6], C Wolfe[3], S Worm[9], T Wright[8], X Wu[35], S M Wynne[27], A Yagil[6], K Yamamoto[58], J Yamaoka[9], Y Yamashita[60], C Yang[49], U K Yang[3], W M Yao[18], G P Yeh[6], J Yoh[6], K Yorita[3], T Yoshida[58], I Yu[38,39,40], S S Yu[53], J C Yun[6], L Zanello[45], A Zanetti[24], I Zaw[41], F Zetti[10], X Zhang[1], J Zhou[9] and S Zucchelli[36] (CDF Collaboration)

[1] University of Illinois, Urbana, IL 61801, USA
[2] University of Florida, Gainesville, FL 32611, USA
[3] Enrico Fermi Institute, University of Chicago, Chicago, IL 60637, USA
[4] University of California, Santa Barbara, Santa Barbara, CA 93106, USA
[5] University of Tsukuba, Tsukuba, Ibaraki 305, Japan
[6] Fermi National Accelerator Laboratory, Batavia, IL 60510
[7] University of Padova, Istituto Nazionale di Fisica Nucleare, Sezione di Padova-Trento, I-35131 Padova, Italy
[8] University of Michigan, Ann Arbor, MI 48109, USA
[9] Rutgers University, Piscataway, NJ 08855, USA
[10] Istituto Nazionale di Fisica Nucleare Pisa, Universities of Pisa, Siena and Scuola Normale Superiore, I-56127 Pisa, Italy
[11] Institute of Physics, Academia Sinica, Taipei, Taiwan 11529, Republic of China

[12] Institute of Particle Physics: McGill University, Montréal, Canada H3A 2T8
[13] University of Toronto, Toronto, Canada M5S 1A7
[14] Waseda University, Tokyo 169, Japan
[15] Joint Institute for Nuclear Research, RU-141980 Dubna, Russia
[16] University of California, Los Angeles, Los Angeles, CA 90024, USA
[17] University of Oxford, Oxford OX1 3RH, UK
[18] Ernest Orlando Lawrence Berkeley National Laboratory, Berkeley, CA 94720, USA
[19] Purdue University, West Lafayette, IN 47907, USA
[20] The Johns Hopkins University, Baltimore, MD 21218, USA
[21] University of California, Davis, Davis, CA 95616, USA
[22] University College London, London WC1E 6BT, UK
[23] Massachusetts Institute of Technology, Cambridge, MA 02139, USA
[24] Istituto Nazionale di Fisica Nucleare, University of Trieste/ Udine, Italy
[25] University of Wisconsin, Madison, WI 53706, USA
[26] Duke University, Durham, NC 27708, USA
[27] University of Liverpool, Liverpool L69 7ZE, UK
[28] The Rockefeller University, New York, NY 10021, USA
[29] Argonne National Laboratory, Argonne, IL 60439, USA
[30] Brandeis University, Waltham, MA 02254, USA
[31] University of Rochester, Rochester, NY 14627, USA
[32] University of Pittsburgh, Pittsburgh, PA 15260, USA
[33] Michigan State University, East Lansing, MI 48824, USA
[34] Glasgow University, Glasgow G12 8QQ, UK
[35] University of Geneva, CH-1211 Geneva 4, Switzerland
[36] Istituto Nazionale di Fisica Nucleare, University of Bologna, I-40127 Bologna, Italy
[37] Institut de Fisica d'Altes Energies, Universitat Autonoma de Barcelona, E-08193, Bellaterra (Barcelona), Spain
[38] Center for High Energy Physics: Kyungpook National University, Taegu 702-701, South Korea
[39] Seoul National University, Seoul 151-742, South Korea
[40] SungKyunKwan University, Suwon 440-746, Korea
[41] Harvard University, Cambridge, MA 02138, USA
[42] Carnegie Mellon University, Pittsburgh, PA 15213, USA
[43] Laboratori Nazionali di Frascati, Istituto Nazionale di Fisica Nucleare, I-00044 Frascati, Italy
[44] Instituto de Fisica de Cantabria, CSIC-University of Cantabria, 39005 Santander, Spain
[45] Istituto Nazionale di Fisica Nucleare, Sezione di Roma 1, University of Rome 'La Sapienza', I-00185 Roma, Italy
[46] Baylor University, Waco, TX 76798, USA
[47] Institut für Experimentelle Kernphysik, Universität Karlsruhe, 76128 Karlsruhe, Germany
[48] The Ohio State University, Columbus, OH 43210, USA
[49] Yale University, New Haven, CT 06520, USA
[50] High Energy Accelerator Research Organization (KEK), Tsukuba, Ibaraki 305, Japan
[51] University of New Mexico, Albuquerque, NM 87131, USA
[52] Texas A&M University, College Station, TX 77843, USA
[53] University of Pennsylvania, Philadelphia, PA 19104, USA
[54] Tufts University, Medford, MA 02155, USA
[55] Wayne State University, Detroit, MI 48201, USA
[56] University of California, San Diego, La Jolla, CA 92093, USA
[57] Northwestern University, Evanston, IL 60208, USA
[58] Osaka City University, Osaka 588, Japan
[59] Institution for Theoretical and Experimental Physics, ITEP, Moscow 117259, Russia
[60] Okayama University, Okayama 700-8530, Japan
[61] Division of High Energy Physics, Department of Physics, University of Helsinki and Helsinki Institute of Physics, FIN-00014, Helsinki, Finland

Received 28 August 2007
Published 5 November 2007
Online at stacks.iop.org/JPhysG/34/2457

Abstract

We report the first measurements of inclusive W and Z boson cross-sections times the corresponding leptonic branching ratios for $p\overline{p}$ collisions at $\sqrt{s} = 1.96$ TeV based on the decays of the W and Z bosons into electrons and muons. The data were recorded with the CDF II detector at the Fermilab Tevatron and correspond to an integrated luminosity of 72.0 ± 4.3 pb^{-1}. We test e-μ lepton universality in W decays by measuring the ratio of the $W \to \mu\nu$ to $W \to e\nu$ cross sections and determine a value of $0.991 \pm 0.004(\text{stat.}) \pm 0.011(\text{syst.})$ for the ratio of $W - \ell - \nu$ couplings (g_μ/g_e). Since there is no sign of non-universality, we combine our cross-section measurements in the different lepton decay modes and obtain $\sigma_W \times \text{Br}(p\overline{p} \to W \to \ell\nu) = 2.749 \pm 0.010(\text{stat.}) \pm 0.053(\text{syst.}) \pm 0.165(\text{lum.})$ nb and $\sigma_{\gamma^*/Z} \times \text{Br}(p\overline{p} \to \gamma^*/Z \to \ell\ell) = 254.9 \pm 3.3(\text{stat.}) \pm 4.6(\text{syst.}) \pm 15.2(\text{lum.})$ pb for dilepton pairs in the mass range between 66 GeV/c^2 and 116 GeV/c^2. We compute the ratio R of the $W \to \ell\nu$ to $Z \to \ell\ell$ cross sections taking all correlations among channels into account and obtain $R = 10.84 \pm 0.15(\text{stat.}) \pm 0.14(\text{syst.})$ including a correction for the virtual photon exchange component in our measured $\gamma^*/Z \to \ell\ell$ cross section. Based on the measured value of R, we extract values for the W leptonic branching ratio, $\text{Br}(W \to \ell\nu) = 0.1082 \pm 0.0022$; the total width of the W boson, $\Gamma(W) = 2092 \pm 42$ MeV; and the ratio of W and Z boson total widths, $\Gamma(W)/\Gamma(Z) = 0.838 \pm 0.017$. In addition, we use our extracted value of $\Gamma(W)$ whose value depends on various electroweak parameters and certain CKM matrix elements to constrain the V_{cs} CKM matrix element, $|V_{cs}| = 0.976 \pm 0.030$.

(Some figures in this article are in colour only in the electronic version)

1. Introduction

Measurements of the production cross sections for both W and Z bosons in high-energy $p\overline{p}$ collisions are important tests of the Standard Model (SM) of particle physics. At hadron colliders the W and Z bosons can most easily be detected through their leptonic decay modes. This paper presents measurements of $\sigma_W \cdot \text{Br}(W \to \ell\nu)$, $\sigma_Z \cdot \text{Br}(Z \to \ell\ell)$, and their ratio

$$R = \frac{\sigma_W \cdot \text{Br}(W \to \ell\nu)}{\sigma_Z \cdot \text{Br}(Z \to \ell\ell)} \tag{1}$$

for $\ell = e$ and μ based on 72.0 pb^{-1} of $p\overline{p}$ collision data collected in 2002–2003 by the upgraded collider detector at Fermilab (CDF) at a center-of-mass energy of 1.96 TeV. These measurements are also described in [1]. These measurements provide a test of SM predictions for the W and Z boson production cross sections, σ_W and σ_Z, as well as a precise indirect measurement of the total decay width of the W boson, $\Gamma(W)$, within the framework of the SM. This analysis is sensitive to deviations in $\Gamma(W)$ from the SM predictions at the level of about 2%. We also use our results to extract the leptonic branching fraction, $\text{Br}(W \to \ell\nu)$, and the Cabibbo–Kobayashi–Maskawa (CKM) matrix element, V_{cs}. Finally, we test the lepton universality hypothesis for the couplings of the W boson to e and μ leptons.

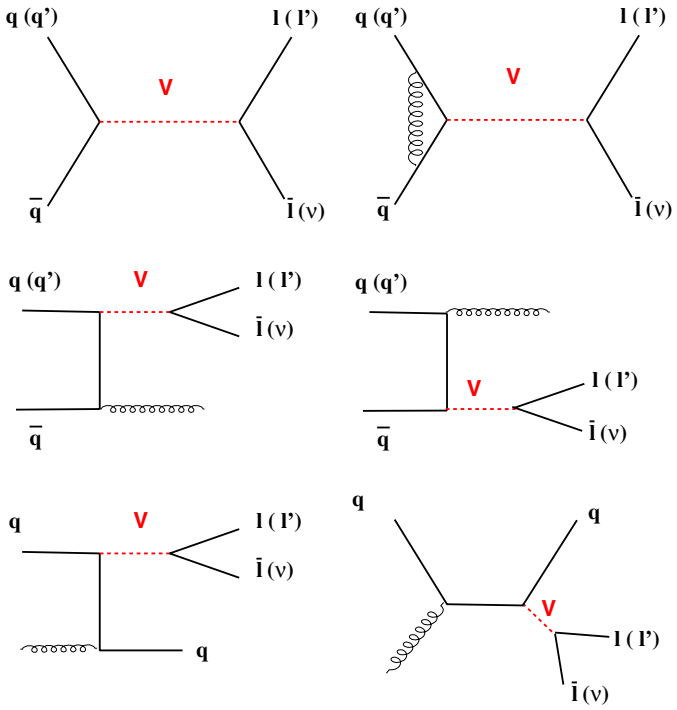

Figure 1. Diagrams for production and leptonic decay of a vector boson $V = W, Z$ at leading (upper left) and next-to-leading order (others).

1.1. W/Z production and decay

The W and Z bosons, together with the massless photon (γ), compose the bosonic fields of the unified electroweak theory proposed by Weinberg [2], Salam [3] and Glashow [4]. The W and Z bosons were discovered in 1983 using the UA1 and UA2 detectors [5–8] which were designed and built for this very purpose. The transverse momentum (p_T) distribution of the reconstructed leptons in $W \to \ell\nu$ events was used to determine the W mass, while the Z mass was determined by directly reconstructing the invariant mass of dilepton pairs in $Z \to \ell\ell$ events.

Present experimental measurements of electroweak parameters including vector boson masses and decay widths are precise enough to provide tests of quantum chromodynamics (QCD) and the electroweak part of the Standard Model beyond leading order. These precise measurements not only test the electroweak theory but also provide possible windows to sectors of the theory at mass scales higher than those directly observable at current accelerator energies. These sectors enter into the electroweak observables through radiative corrections. While the parameters of the Z boson have been well studied [9], the properties of the charged current carriers, the W bosons, are known with less precision. In hadron–antihadron collisions the W and Z are predominantly produced via the processes illustrated in figure 1. The production of $p\overline{p} \to \gamma^*/Z$ where a quark in one hadron annihilates with an antiquark in the other hadron to produce the resulting vector boson is often referred to as the Drell–Yan [10] production process.

Calculations of the total production cross sections for W and Z bosons incorporate parton cross sections, parton distribution functions, higher order QCD effects and factors for the couplings of the different quarks and antiquarks to the W and Z bosons. Beyond the leading order Born processes, a vector boson V can also be produced by $q(\bar{q})g$ interactions, so the parton distribution functions (PDFs) of the proton and antiproton play an important role at higher orders. Theoretical calculations of the W and Z production cross sections have been carried out in next-to-leading order (NLO) [11, 12] and next-to-next-to-leading order (NNLO) [13–17]. The NLO and NNLO computations used in this paper are in the modified minimal-subtraction ($\overline{MS}$) [18, 19] renormalization prescription framework. The full order α_s^2 calculation has been made and includes final states containing the vector boson V and up to two additional partons. The two-loop splitting function is used and the running of α_s includes thresholds for heavy flavors. The NLO cross section is ∼25% larger than the Born-level cross section, and the NNLO cross section is an additional ∼3% higher. The main contribution to the calculated cross section is from $q\overline{q}$ interactions. The contribution of $q(\bar{q})g$ interactions to the calculated cross section is negative at the Tevatron collision energy.

The decay modes of the W boson are $W \to \ell\nu$ ($\ell = e, \mu$ and τ) and $q\bar{q}'$, where the main modes $u\bar{d}$, $u\bar{s}$, $c\bar{s}$ and $c\bar{d}$ have branching ratios proportional to their corresponding CKM matrix elements. The measured value for the branching fraction of the three combined leptonic modes is $32.0 \pm 0.4\%$ [20], where the remaining fraction is assigned to the hadronic decay modes. The partial width into fermion pairs is calculated at lowest order to be [20]

$$\Gamma_0(W \to \mathrm{f}\bar{\mathrm{f}}') = |V_{\mathrm{ff}'}|^2 N_C G_F M_W^3 / (6\sqrt{2}\pi), \tag{2}$$

where $V_{\mathrm{ff}'}$ is the corresponding CKM matrix element for quark pairs or one for leptons. M_W is the W boson mass and G_F is the Fermi coupling constant. N_C is the corresponding color factor which is 3 for quarks and 1 for leptons.

The expression for the partial decay widths into quark pairs also has an additional QCD correction due to vertex graphs involving gluon exchange and electroweak corrections due to next-to-leading order graphs which alter the effective coupling at the W-fermion vertex for all fermions. Within the context of the Standard Model, there are also vertex and bremsstrahlung corrections [21] that depend on the top quark and Higgs boson masses. The corrections can be summarized in the equation

$$\Gamma(W \to \mathrm{f}\bar{\mathrm{f}}')_{\mathrm{SM}} = \Gamma_0(W \to \mathrm{f}\bar{\mathrm{f}}')[1 + \delta_V + \delta_{W(0)} + \delta_\mu], \tag{3}$$

where $\delta_{W(0)}$ is the correction to the width from loops at the W-fermion vertex involving the Z boson or a SM Higgs boson, δ_V arises from the boson self-energies, and δ_μ is a correction required when the couplings are parametrized using the W mass and the value of G_F from muon-decay measurements [22, 23]. Since all of these corrections are small (∼0.35%), the measurement of $\Gamma(W)$ is not very sensitive to these higher order effects. Higher order QCD corrections originating from quark mass effects are also small.

1.2. Measurement of $\Gamma(W)$ *from the* W *and* Z *cross sections*

The width of the W boson can be extracted from the measurement of the ratio R, which is defined in equation (1). This method was first proposed by Cabibbo in 1983 as a method to determine the number of light neutrino species [24] and has been adopted as a method to indirectly measure the branching ratio for the $W \to \ell\nu$ decay mode. The ratio R can be expressed as

$$R = \frac{\sigma_W}{\sigma_Z} \frac{\Gamma(W \to \ell\nu)}{\Gamma(Z \to \ell\ell)} \frac{\Gamma(Z)}{\Gamma(W)}. \tag{4}$$

Table 1. Previous measurements of the W and Z production cross-sections times branching ratios along with the measured values of R and the extracted values of $\Gamma(W)$.

Experiment	$\sqrt{s}$ (TeV)	Mode	$\sigma_W \cdot \mathrm{Br}(W \to \ell\nu)$ (nb)	$\sigma_Z \cdot \mathrm{Br}(Z \to \ell\ell)$ (pb)	R	$\Gamma(W)$(GeV)
CDF(Run I) [25–29]	1.80	e	2.49 ± 0.12	231 ± 12	10.90 ± 0.43	2.064 ± 0.084
DØ(Run IA) [30]	1.80	e	2.36 ± 0.15	218 ± 16		
DØ(Run IA) [30]	1.80	μ	2.09 ± 0.25	178 ± 31		
DØ(Run IA) [30, 31]	1.80	$e + \mu$			10.90 ± 0.49	2.044 ± 0.093
DØ(Run IB) [32]	1.80	e	2.31 ± 0.11	221 ± 11	10.43 ± 0.27	2.17 ± 0.07

On the right hand side of equation (4), the ratio of the W and Z production cross sections can be calculated from the boson couplings and knowledge of the proton structure. The Z boson total width, $\Gamma(Z)$, and leptonic partial width, $\Gamma(Z \to \ell\ell)$, have been measured very precisely by the LEP experiments [9]. With the measured value of R the branching ratio $\mathrm{Br}(W \to \ell\nu) = \Gamma(W \to \ell\nu)/\Gamma(W)$ can be extracted directly from equation (4). The total width of the W boson, $\Gamma(W)$, can also be determined indirectly using the SM prediction for the partial width, $\Gamma(W \to \ell\nu)$. As shown in equation (2), $\Gamma(W)$ depends on electroweak parameters and certain CKM matrix elements. We also use our measurement of the total W width to constrain the associated sum over CKM matrix elements in the formula for $\Gamma(W)$ and derive an indirect value for V_{cs} which is the least experimentally constrained element in the sum. Finally, the ratios of the muon and electron $W \to \ell\nu$ cross-section measurements are used to determine the ratios of the coupling constants of the W boson to the different lepton species, providing a test of the lepton universality hypothesis. For reference, table 1 provides a summary of previous experimental results for $\sigma_W \cdot \mathrm{Br}(W \to \ell\nu)$ and $\sigma_Z \cdot \mathrm{Br}(Z \to \ell\ell)$ along with the measured values for R and the extracted values of $\Gamma(W)$. The most recent direct measurement of $\Gamma(W)$ obtained by LEP is 2.150 ±0.091GeV [9].

1.3. Overview of this measurement

The signature of high transverse momentum leptons from W and Z decay is very distinctive in the environment of hadron collisions. As such, the decay of W and Z bosons into leptons provides a clean experimental measurement of their production rate. Experimentally, the cross-sections times branching ratios are calculated from

$$\sigma_W \cdot \mathrm{Br}(W \to \ell\nu) = \frac{N_W^{\mathrm{obs}} - N_W^{\mathrm{bck}}}{A_W \cdot \epsilon_W \cdot \int \mathcal{L}\,\mathrm{d}t} \tag{5}$$

$$\sigma_Z \cdot \mathrm{Br}(Z \to \ell\ell) = \frac{N_Z^{\mathrm{obs}} - N_Z^{\mathrm{bck}}}{A_Z \cdot \epsilon_Z \cdot \int \mathcal{L}\,\mathrm{d}t}, \tag{6}$$

where N_W^{obs} and N_Z^{obs} are the numbers of $W \to \ell\nu$ and $Z \to \ell\ell$ candidates observed in the data; N_W^{bck} and N_Z^{bck} are the numbers of expected background events in the W and Z boson candidate samples; A_W and A_Z are the acceptances of the W and Z decays, defined as the fraction of these decays satisfying the geometric constraints of our detector and the kinematic constraints of our selection criteria; ϵ_W and ϵ_Z are the combined efficiencies for identifying W and Z decays falling within our acceptances; and $\int \mathcal{L}\,\mathrm{d}t$ is the integrated luminosity of our data samples.

In measuring the ratio of the cross sections some of the inputs and their experimental uncertainties cancel. The strategy of this measurement is to select W and Z boson decays

with one or both leptons (e or μ) falling within the central region of the CDF detector. This region is well instrumented and understood and has good detection efficiencies for both lepton species. Using common lepton selection criteria (contributing to the factors ϵ_W and ϵ_Z) for the W and Z channels has the great advantage of decreasing the systematic uncertainty in the measurement of R. The resulting smaller systematic uncertainty offsets the expected increase in statistical uncertainty originating from the requirement of a common central lepton. For each lepton species, the selection criteria are optimized to obtain the least overall experimental uncertainty.

The measurement of the ratio R is sensitive to new physics processes which change the W or Z production cross sections or the $W \to \ell\nu$ branching ratio. The $W \to \ell\nu$ branching ratio could be directly affected by new decay modes of the W boson, such as supersymmetric decays that do not similarly couple to the Z boson. A new resonance at a higher mass scale that decays to W or Z bosons may change the production cross sections. One example of a particle with a larger mass is the top quark at $m_{\rm t} = 174.3 \pm 5.1$ GeV/c^2, which decays to a W boson and a bottom quark [20]. In $p\overline{p}$ collisions at $\sqrt{s}$ = 1.8 TeV the production cross section for $\mathrm{t\bar{t}}$ pairs is $6.5^{+1.7}_{-1.4}$ pb [33], about 3000 times smaller than direct W boson production [25]. The decays of $t\bar{t}$ pairs which result in the production of two W bosons should change the measured value of R by about 7×10^{-4}, which is well below our sensitivity. The total width of the W boson can also get contributions from processes beyond the SM. For example, in supersymmetry, the decay $\mathrm{W}^+ \to \chi^+\chi^0$ may be possible if the charginos and neutralinos are light [34] and so a precise measurement of $\Gamma(W)$ can constrain the properties of these particles.

1.4. Outline of the paper

This paper is organized as follows: in section 2 the CDF detector is described, with particular attention given to the subdetectors essential in the identification of charged leptons and the inference of neutrinos. Section 3 describes the data samples used in this analysis, and the selection of the W and Z candidate events is described in section 4. Section 5 describes the calculation of the geometric and kinematic acceptances of our candidate samples, and the methods used to determine the efficiencies for identifying events within our acceptances are presented in section 6. The estimation of the contributions to our candidate samples from background processes are discussed in section 7, and finally the calculation of the cross sections along with the resulting value of R and other extracted quantities are summarized in section 8.

2. The experimental apparatus

The data used for the measurements reported in this note were collected with the upgraded Collider Detector (CDF) [35] at the Fermilab Tevatron $p\overline{p}$ collider. Detector upgrades were made to accommodate the higher luminosities and new beam conditions resulting from concurrent upgrades to the Tevatron accelerator complex. In addition to the increases in luminosity, the $p\overline{p}$ center-of-mass energy was also increased from $\sqrt{s} = 1.80$ TeV to $\sqrt{s} = 1.96$ TeV. The relatively small change in beam energies leads to a substantial increase in the production cross sections for high-mass objects such as W/Z bosons ($\sim$9%) and top quark pairs ($\sim$30%). We highlight the upgrades to the Run I detectors and electronics in the following sections.

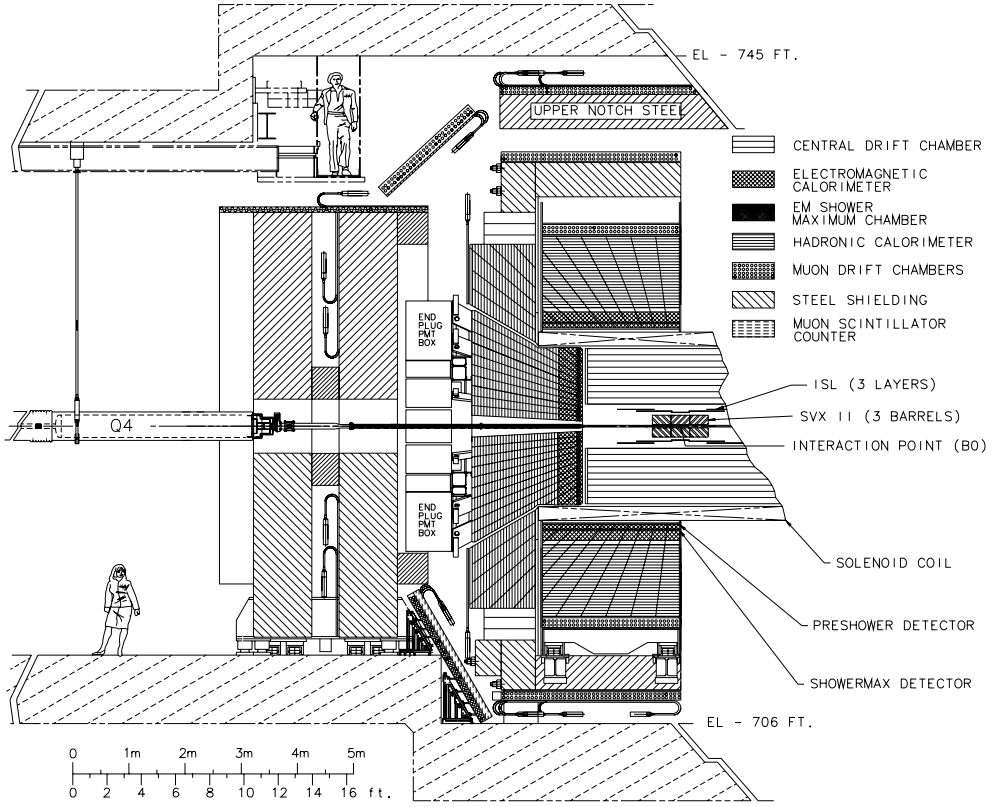

Figure 2. Elevation view of half of the CDF Run II detector.

2.1. The CDF II detector

CDF is a general-purpose detector [35–37] designed to detect particles produced in $p\overline{p}$ collisions. As illustrated in figure 2, the detector has a cylindrical layout centered on the accelerator beamline. Tracking detectors are installed in the region directly around the interaction point to reconstruct charged-particle trajectories inside a 1.4 T uniform magnetic field (along the proton beam direction). The field is produced by a 5 m long superconducting solenoid located at the outer radius of the tracking region (1.5 m). Calorimeter modules are arranged in a projective tower geometry around the outside of the solenoid to provide energy measurements for both charged and neutral particles. The outermost part of the detector consists of a series of drift chambers used to detect muons which are minimum-ionizing particles that typically pass through the calorimeter.

The z-axis of the CDF coordinate system is defined to be along the direction of the incoming protons. A particle trajectory is then described by θ, the polar angle relative to the incoming proton beam; ϕ, the azimuthal angle about this beam axis; and z_0, the intersection point of the particle trajectory with the beam axis. The pseudorapidity of a particle trajectory is defined as $\eta = -\ln(\tan(\theta/2))$. The transverse momentum, p_T, is the component of the momentum projected on a plane perpendicular to the beam axis. Similarly, the transverse energy, E_T, of a shower or an individual calorimeter tower is given by $E \cdot \sin\theta$. The total transverse energy in an event is given by a sum over all calorimeter towers $\sum_i E_T^i \hat{n}_i$ where E_T^i

is the transverse energy measured in the ith tower and $\hat{n}_i$ is the projection of the vector pointing from the event vertex to the ith calorimeter tower onto the plane perpendicular to the beam axis (unit normalized). The vector sum of transverse energies measured in the calorimeter is corrected to account for muons which deposit only a fraction of their energy in the calorimeter. The missing transverse energy in an event is the equal magnitude vector opposite to this vector sum of transverse energies. Fixed points on the detector are described using polar coordinates (r,ϕ,z) where r is the radial distance from the beam axis, ϕ is the azimuthal direction about the beam axis and z is the distance from the detector center in the direction along the beam axis. In some cases we also use a detector pseudorapidity variable, $\eta_{\rm det}$, to refer to fixed locations within the detector. This variable is based on the standard definition of pseudorapidity given above where the angle θ is redefined in the context of a fixed location as $\theta = \arctan(r/z)$.

2.2. *Tracking system*

All of the detectors in the inner tracking region have been replaced for Run II. The new silicon tracking system consists of three concentric detectors located just outside the beam interaction region. In combination, these detectors provide high resolution tracking coverage out to $|\eta_{\rm det}| < 2$. For the measurements presented here, silicon tracking information is incorporated solely to aid in the rejection of cosmic ray events from our muon samples. The relevant hit information comes from the Silicon Vertex Detector (SVX-II) [38] which contains five layers of double-sided micro-strip detectors at radii of 2.4 to 10.7 cm from the center of the detector. The SVX-II detector consists of three barrels divided into 12 wedges in ϕ. In total, the three barrels cover roughly 45 cm along the z-axis on each side of the detector interaction point.

The new open-cell drift chamber referred to as the central outer tracker (COT) [39, 40] sits directly outside of the silicon tracking detectors in the radial direction. The measured momenta and directions of the high p_T lepton candidates in our event samples are obtained from track reconstruction based solely on COT hit information. The chamber consists of eight superlayers of 310 cm length cells at radii between 40 and 132 cm from the beam axis. Each superlayer contains 12 layers of sense wires strung between alternating layers of potential wires. The wires in four of the superlayers (axial layers) are strung to be parallel to the beam axis, providing particle track reconstruction in the transverse plane. In the other four superlayers (stereo layers), the wires are strung at $\pm 2^\circ$ angles with respect to the beam axis to allow also for particle tracking in the z-direction. The two superlayer types are alternated in the chamber within the eight radial layers starting with the innermost stereo layer. The COT chamber has over 30 000 readout channels, roughly five times the number in the Run I tracking chamber [41]. Particles traversing the central region of the detector ($|\eta_{\rm det}| < 1$) are expected to be measured by all eight superlayers.

The COT is filled with a gas mixture of 50% argon and 50% ethane. This mixture was chosen to ensure a fast drift velocity ($\sim$50 μm ns^{-1}) compatible with the short interval between beam bunch crossings and the expected rise in instantaneous luminosity. The maximum drift distance in the chamber is 0.88 cm corresponding to a drift time on the order of 200 ns. The single-hit resolution in the chamber has been studied using the high p_T muon tracks in $Z \to \mu\mu$ candidate events. The measured offset between the individual hits associated with these muons and the reconstructed path of the muon track is shown in figure 3. Based on this distribution, we measure a COT single-hit resolution of 180 μm.

The solenoid produces a 1.4 T magnetic field inside the tracking volume that is uniform to 0.1% in the region $|z| < 150$ cm and $|r| < 150$ cm. The transverse momentum of a reconstructed track, p_T (in GeV/c), is determined from $p_T = 0.3qBr_c$, where B (in T) is the magnetic field strength, the total particle charge is qe (e is the magnitude of the electron charge)

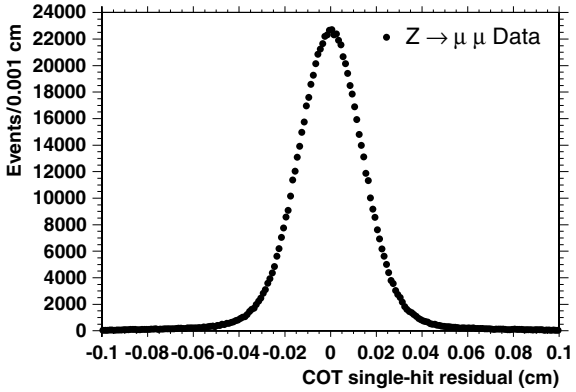

Figure 3. COT single-hit residual distribution obtained from $Z \rightarrow \mu\mu$ events.

and r_c (in m) is the measured radius of curvature of the track. The resolution of the COT track momentum measurement decreases for high p_T tracks which bend less in the magnetic field. The curvature resolution has been studied by comparing the inward and outgoing track legs of reconstructed cosmic ray events. The difference in the measured curvature for the two track legs in these events is shown on the top of figure 4. We determine a COT curvature resolution of $3.6 \times 10^{-6}\text{cm}^{-1}$, estimated from the σ of this distribution divided by $\sqrt{2}$. This corresponds to a momentum resolution of $\sigma_{p_T}/p_T^2 \simeq 1.7 \times 10^{-3}(\text{GeV}/c)^{-1}$. The COT track momentum resolution is also studied using the E/p distribution (see section 4) of electron candidates in $W \rightarrow e\nu$ events. This distribution is shown on the bottom of figure 4. Since the COT track momentum resolution measurement is less precise at high p_T than the corresponding calorimeter energy measurement, the Gaussian width of this distribution for $0.8 < E/p < 1.08$ provides an additional measure of the curvature resolution. The resulting value is in good agreement with that obtained from studying cosmic ray events.

2.3. Calorimeters

Calorimeter modules used to measure the energy of both charged and neutral particles produced in $p\overline{p}$ collisions are arranged around the outer edges of the central tracking volume. These modules are sampling scintillator calorimeters with a tower based projective geometry. The inner electromagnetic sections of each tower consist of lead sheets interspersed with scintillator, and the outer hadronic sections are composed of scintillator sandwiched between sheets of steel. The CDF calorimeter consists of two sections: a central barrel calorimeter ($|\eta_{\text{det}}| < 1$) and forward end plug calorimeters ($1.1 < |\eta_{\text{det}}| < 3.64$). The scintillator planes in the central barrel lie parallel to the beam line, while those in the forward end plugs are arranged in the transverse direction. The central barrel consists of projective readout towers, each subtending 0.1 in η_{det} and 15° in ϕ. Each end plug also has projective readout towers, the sizes of which vary as a function of η_{det} (0.1 in η_{det} and 7.5° in ϕ at $|\eta_{\text{det}}| = 1.1$ to 0.5 in η_{det} and 15° in ϕ at $|\eta_{\text{det}}| = 3.64$).

The central barrel section of the CDF calorimeter is unchanged from Run I. It consists of an inner electromagnetic (CEM) calorimeter and an outer hadronic (CHA) calorimeter [42]. The end-wall hadronic (WHA) calorimeter completes the coverage of the central barrel calorimeter in the region $0.6 < |\eta_{\text{det}}| < 1.0$ and provides additional forward coverage out to $|\eta_{\text{det}}| = 1.3$ [43]. As part of the CDF Run 2 upgrade, the original gas calorimetry of the end

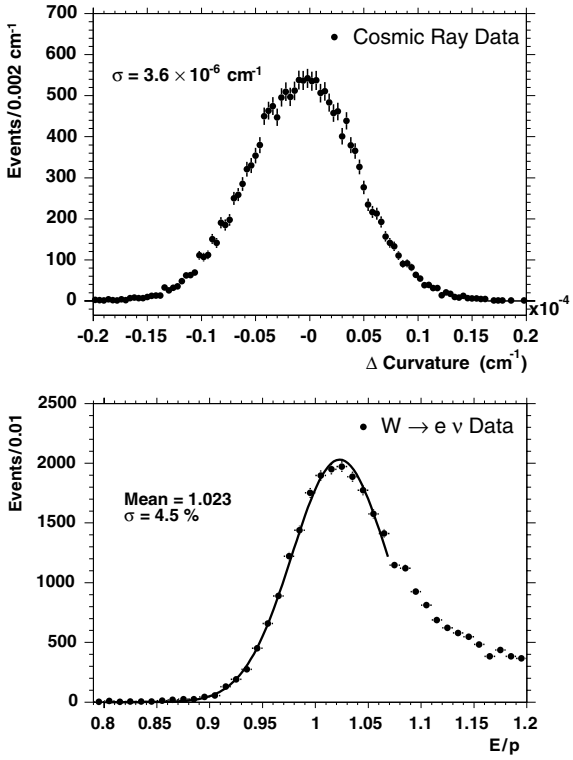

Figure 4. Distribution of the difference in curvature for the two tracks associated with a cosmic ray event as reconstructed by the COT, using cosmic ray data (top). Distribution of the E/p variable defined in section 4 for $W \to e\nu$ events (bottom). The mean and σ are obtained from the Gaussian fit in the range $0.8 < E/p < 1.08$.

plug region ($|\eta_{\text{det}}| > 1.1$) was replaced with scintillator plate calorimetry using scintillator tiles read out by wavelength shifting fibers embedded in the scintillator [44, 45]. The new design has an improved sampling fraction and reduces forward gaps that existed in the old gas calorimeter system. The new plug electromagnetic (PEM) calorimeter provides coverage in the $1.1 < |\eta_{\text{det}}| < 3.6$ region and the new plug hadronic (PHA) calorimeter provides coverage in the $1.3 < |\eta_{\text{det}}| < 3.6$ region [46]. Both the PEM and PHA incorporate the same polystyrene based scintillator and similar photomultiplier tubes used in the CEM.

Calorimeter energy resolutions are measured using test-beam data. The measured energy resolutions for electrons in the electromagnetic calorimeters are $14\%\sqrt{E_T}$ (CEM) and $16\%\sqrt{E} \oplus 1\%$ (PEM) [35], where the units of E_T and E are GeV. We also measure the single-particle (pion) energy resolution in the hadronic calorimeters to be $75\%/\sqrt{E}$ (CHA), $80\%/\sqrt{E}$ (WHA) and $80\%\sqrt{E} \oplus 5\%$ (PHA) [35]. The energy resolution in the electromagnetic calorimeters is also determined using $Z \to ee$ candidate events. The calorimeter energy scale is set so that the mean of the Gaussian fit to the dielectron invariant mass peak is 91.1 GeV/c^2. This procedure results in a CEM energy resolution of $13.5\%\sqrt{E_T} \oplus 1.5\%$, in good agreement with the test-beam result [47]. Jet energy resolution in the hadronic calorimeter sections [48] is determined using photon-jet balancing. In events in which a photon recoils against a jet and no other activity is observed, the transverse energies associated with the

two objects must be equal and opposite. The photon energy measured in the electromagnetic section of the calorimeter provides a reference point against which the energy deposition associated with the jet can be compared. The resolution of the large component of jet energy deposition in the hadronic calorimeters can be determined based on this comparison. The vast majority of hadronic particle showers are completely contained within the calorimeter. The combined longitudinal depth of the central calorimeter module in interaction lengths is roughly 5.5λ and the equivalent depth in the plug modules is roughly 8.0λ. However, some small fraction of hadronic particle showers does leak out from the back end of the calorimeter, complicating muon identification.

Proportional chambers (CES) are embedded in the electromagnetic section of the central barrel at a radiation length depth of roughly $6X_0$ corresponding to the region of maximum shower intensity for electrons. These chambers are used to measure the profile of a shower and extract the location of the incident particle within a given tower. The increased shower position resolution provides additional selection criteria for electron candidates based on track-shower matching. The chambers, two per calorimeter wedge, utilize wires in the r–ϕ view and cathode strips in the z view to determine the three-dimensional position of each shower. The resolution of the CES position measurement in r–ϕ is roughly 0.2 cm. Each calorimeter module also has a second set of chambers (CPR) situated on the front of the corresponding electromagnetic section which presamples each shower to provide additional information useful in electron identification and pion-photon separation.

The first layer of the plug electromagnetic calorimeter is used as a preshower detector (PPR). Its scintillator is polyvinyltoluene-based, and it is twice as thick as the other sampling layers in the PEM. It has the same transverse segmentation as the PEM, but each scintillator tile in the PPR is read out individually. The PEM also has a shower maximum detector (PES) embedded in it at a depth of $\sim 6X_0$ [49]. The PES consists of two layers of 5 mm wide polyvinyltoluene-based scintillator strips, with each layer having a 45° crossing angle relative to the other. The PES provides coverage in the $1.1 < |\eta_{\rm det}| < 3.5$ region.

2.4. Muon detectors

In order for a muon to pass through the calorimeter and into the most central portion of the CDF muon detector ($|\eta_{\rm det}| \leqslant 0.6$), it must have a minimum p_T on the order of 1.4 GeV/c. In order to reach the outer portion of the central detector or the more forward detectors ($0.6 < |\eta_{\rm det}| < 1.0$), the muon is required to pass through an additional layer of steel absorber. Muons with a momentum above 3.0 GeV/c are essentially 100% efficient for traversing the steel absorber over the entire solid angle of the combined muon detector coverage. The amount of energy deposited in the calorimeter by high p_T muons produced in W and Z boson decays is observed to be Landau distributed with means of 0.3 GeV for deposits in the electromagnetic section and 2.0 GeV for those in the hadronic section. Reconstructed particle tracks in the COT matched to minimum ionizing-like energy deposits in the calorimeter are treated as 'stubless' muon candidates even in cases where the tracks are not matched with any hits in the muon detectors. The muon offline reconstruction forms stubs based on hit information in the muon detector and matches found stubs with the reconstructed COT tracks to determine our highest quality muon candidates. This final set of muon candidates includes only a small percentage of non-muon fakes originating from other hadronic particles that are not fully contained within the calorimeter (hadronic punchthrough). Despite the fact that a non-negligible number of hadrons (on the order of 1 in 220) pass through the entire calorimeter, the majority of those that enter the muon detector are absorbed in the filtering steel and do not produce associated hits in the outer sections of the detectors. Conversely, 'stubless' muon candidates include a

substantially larger fraction of non-muon fakes, and the presence of additional physics objects (such as a second higher quality muon) associated with these candidates is typically required to increase the purity of the sample.

The CDF muon detector is made up of four independent detector systems outside the calorimeter modules. The central muon detector (CMU) [50] is mounted directly around the outer edge of the central calorimeter module. The CMU is an original Run I detector component containing 2304 single-wire drift chambers arranged in four concentric radial layers. The drift chamber wires are strung parallel to the direction of the incoming beams, and wire pairs on layers 1 and 3 and layers 2 and 4 project radially back to the nominal beam interaction point, allowing for a coarse p_T measurement based on the difference in signal arrival times on the two wires within a pair. The CMU system provides symmetrical coverage in ϕ in the central part of the detector ($|\eta_{\text{det}}| \leqslant 0.6$). The drift chambers have been upgraded to operate in proportional mode (in Run I these chambers were run in streamer mode). Operating in this mode reduces the high voltage settings for the chambers and helps to prevent voltage sagging which is an issue due to the higher hit rates at Run II luminosities. Precision position measurements in the ϕ direction are made by converting signal arrival times into drift distances in the plane orthogonal to the wire direction. The wires of cells in neighboring stacks are connected via resistive wires at the non-readout end of cells to also provide a coarse measurement of each hit position along the direction of the wire (z coordinate). The measurement is made by comparing time-over-threshold for the signals observed at the readout end of the two neighboring stacks. The maximum drift time within a CMU cell is 800 ns which is longer than the 396 ns spacing between bunch crossings in the accelerator. The ambiguity as to which beam crossing a particular CMU hit originates from is resolved in both the trigger and the offline reconstruction using timing information associated with a matched COT track and/or matching energy in the calorimeter.

The Central muon upgrade detector (CMP) and central muon extension detector (CMX) were also part of the CDF Run I configuration [51]. The individual wire drift chambers of these detectors are identical except for their lengths along the direction of the wire which is larger for CMP chambers. These drift cells are roughly a factor of 2 wider than those in the CMU detector resulting in a longer maximum drift time of 1.8 μs. Matching scintillator detectors (CSP, CSX) installed on the outer edges of these systems can in principle provide timing information to resolve the three beam-crossing ambiguity arising from the long drift time. In practice, however, occupancies in these chambers are small enough at current luminosities to uniquely determine the appropriate beam crossing from COT track matching. CSX timing information is used in the trigger to eliminate out-of-time hits from the beam halo associated with particle losses in the accelerator tunnel, but information from the scintillator systems is not currently utilized in muon reconstruction in this analysis. The CMP/CMX drift chambers are also run in proportional mode. The CMP chambers are arranged in a box-like structure around the outside of the CMU detector and an additional 3λ of steel absorber which is sandwiched between the two detectors. The additional steel greatly reduces hadronic punchthrough into the CMP chambers and allows for cleaner muon identification. A total of 1076 drift cells arranged in four staggered layers form the four-sided CMP structure which provides additional coverage for the central part of the detector ($|\eta_{\text{det}}| \leqslant 0.6$) with variable coverage in ϕ. Drift cells in the CMX detector are arranged in conical arrays of eight staggered layers to extend muon coverage up to $|\eta_{\text{det}}| \leqslant 1.0$. The partial overlap between drift tubes in the CMX conical arrangement allows for a rough hit position measurement in the z coordinate utilizing the different stereo angles of each cell with respect to the beam axis. The Run I configuration consisted of 1536 drift cells arranged in four 120° sections providing coverage between $-45°$ to 75° and 105° to 225° in ϕ on both ends of the detector. An additional 60°

of CMX coverage on the bottom of the detector at both ends has been added for Run II, but these new components were still being commissioned in early running and are not utilized in the measurements reported here. The barrel muon upgrade detector (BMU) is another new addition for Run II which provides additional muon coverage in the regions $1.0 < |\eta_{\rm det}| < 1.5$. This new detector system was also being commissioned in the initial part of Run II and is not used in these measurements.

2.5. Cherenkov luminosity counters

The small-angle Cherenkov luminosity counters (CLC) detector is used to measure the instantaneous and integrated luminosity of our data samples. This detector system is an additional Run II upgrade [52] that allows for high-precision luminosity measurements up to the highest expected instantaneous luminosities.

The CLC consists of two modules installed around the beampipe at each end of the detector, which provide coverage in the regions $3.6 < |\eta_{\rm det}| < 4.6$. Each module consists of 48 long, conical gas Cherenkov counters pointing to the collision region. The counters are arranged in three concentric layers of 16 counters each, around the beam-pipe. The counters in the two outer layers are about 1.8 m and those in the inner layer are 1.1 m long. Each counter is made of highly reflective aluminized Mylar with a light collector that gathers the Cherenkov light into fast, radiation hard photomultiplier tubes with good ultraviolet quantum efficiency. The modules are filled with isobutane gas at about 22 psi which is an excellent radiator while having good ultraviolet transparency.

The Cherenkov light cone half-angle, $\theta_{\rm c}$, is 3.1° corresponding to a momentum threshold for light emission of 9.3 MeV/c for electrons and 2.6 GeV/c for pions. The expected number of photoelectrons, $N_{\rm pe}$, for a single counter is given by $N_{\rm pe} = N_{\rm o} \cdot L \cdot \sin^2\theta_{\rm c}$ where L is the distance traversed by the particle in the medium and $N_{\rm o} = 370\,{\rm cm}^{-1}\,{\rm eV}^{-1} \int \epsilon_{\rm col}(E)\epsilon_{\rm det}(E)\,{\rm d}E$. The $\epsilon_{\rm det}$ and $\epsilon_{\rm col}$ terms are defined as the light detection and collection efficiencies, respectively, and are functions of the energy E of the Cherenkov photon (in eV). Our design results in $N_{\rm o} \sim 200\,{\rm cm}^{-1}$ corresponding to $N_{\rm pe} \sim 0.6\,{\rm cm}^{-1}$ [53].

The details of the luminosity measurement are described in section 3.

2.6. Trigger systems

The CDF trigger system [54, 55] was redesigned for Run II because of the changes in accelerator operating conditions. The upgraded trigger system reduces the raw event rate in the detector (the nominal 2.5 MHz beam crossing rate) to 75 Hz, the typical rate at which events can be recorded.

The corresponding event rejection factor of roughly 3×10^4 is obtained using a three-level system where each level is designed to provide sufficient rejection to allow for processing with minimal deadtime at the subsequent level. The first level of the trigger system (level 1) utilizes custom hardware to select events based on information in the calorimeters, tracking chambers and muon detectors. Three parallel, synchronous hardware processing streams are used to create the trigger primitive data required to make the level 1 decision. All detector data are fed into 6 μs pipelines to allow for processing time required at level 1. The global level 1 decision must be made and returned to the front-end detector hardware before the corresponding collision data reach the end of the pipeline. Trigger decisions are made at the 2.5 MHz crossing rate, providing dead-time free operation.

One set of level 1 hardware is used to find calorimeter objects (electrons and jets) and calculate the missing transverse energy and total transverse energy seen by the calorimeter in

each event. At level 1, electron and jet candidates are defined as single-tower energy deposits above some threshold in the electromagnetic or electromagnetic plus hadronic sections of trigger towers, respectively. Calorimeter energy quantities are calculated by summing the transverse components of all single tower deposits assuming a collision vertex of $z = 0$. A second set of hardware is utilized to select muon candidates from observed hits in the muon detector wire chamber and scintillator systems. A loose p_T threshold is applied based on differences in signal arrival times on pairs of projective wires in the CMU and CMX chambers. CMP primitives obtained from a simple pattern finding algorithm using observed hits on the four drift cell layers are matched to high p_T CMU candidates, and CSX hits within a certain time window consistent with collision-produced particles are matched to CMX candidates.

An important element of the Run II CDF trigger upgrade is the third set of hardware which identifies COT track candidates within the tight level 1 timing constraints. The eXtremely Fast Tracker (XFT) [56] hardware examines hits on each axial superlayer of the COT and combines them into track segments. The found segments on the different layers are then linked to form tracks. The triggers used to collect the data samples utilized in these measurements are based on XFT tracks with reconstructed segments on all four COT axial superlayers. As discussed in more detail in section 4, this requirement has a small effect on the geometrical acceptance for lepton track candidates in our samples. The hit requirement for XFT track segments was changed from hits on 10/12 layers to hits on 11/12 layers during the data collection period for the samples used in these measurements. This change led to a few percent drop in the trigger efficiency for high p_T tracks but provided a substantial increase in overall level 1 event rejection. The XFT hardware reports tracks in 1.25° bins in ϕ. If more than one track is reconstructed within a given ϕ bin, the track with the highest p_T is used. The XFT feeds its lists of found tracks to another piece of hardware known as the track extrapolation unit (XTRP). The XTRP determines the number of tracks above certain p_T thresholds and makes this information available for the global level 1 decision. It also extrapolates each track based on its reconstructed p_T into the calorimeter and muon detectors to determine into which ϕ slices of each system the track points based on the potential effects of multiple scattering. This information is passed to the calorimeter and muon parts of the level 1 trigger hardware in two sets of 2.5° ϕ bins corresponding to groups of tracks above two programmable p_T thresholds. Using this information, tracks are then matched to electron and muon primitives identified in those pieces of the level 1 hardware to produce the final lists of electron and muon objects.

The final level 1 trigger decision is made based on the number of physics objects (electrons, muons, jets and tracks) found by the hardware and the calculated global calorimeter energy quantities. The maximum level 1 event accept rate is roughly 20 kHz corresponding to an available level 2 processing time of 50 μs per event. Events accepted at level 1 are stored in one of four buffers in the front-end readout hardware. Multiple event buffers allow for additional level 1 triggers to be accepted during the level 2 processing of a previously accepted event. The level 2 trigger system utilizes a combination of dedicated hardware and modified commercial processors to select events. There are two main pieces of dedicated level 2 hardware. The first is the cluster finder hardware which merges the observed energy deposits in neighboring calorimeter towers to form clusters, and the second is the silicon vertex tracking hardware (SVT) [57] which uses silicon detector hit information to search for tracks with displaced vertices. These systems are asynchronous in that processing time is dependent on the amount of input data associated with a given event. The output of these systems is passed to the global level 2 processor along with the input data utilized in the level 1 decision and additional hit information from the CES to aid in low E_T electron selection. The data are fed into the level 2 processor board and simple selection algorithms, optimized for speed, are run to determine which events are passed to level 3. The processor board has been designed to simultaneously

read in one event while processing another which streamlines operation and helps to keep data acquisition deadtime at a minimum [55].

Events selected by the level 2 trigger hardware are read out of the front-end detector buffers into the level 3 processor farm. The current maximum level 2 accept rate for events into level 3 is roughly 300 Hz. Level 3 processors run a speed-optimized version of the offline reconstruction code and impose loose sets of selection cuts on the reconstructed objects to select the final 75 Hz of events which are recorded for further processing. The level 3 processor farm is made up of roughly 300 commercial dual processor computers running Linux to allow for one second of processing time for each event. The software algorithms run at level 3 take advantage of the full detector information and improved resolution unavailable at the lower trigger levels. The level 3 algorithms are based on full three-dimensional track reconstruction (including silicon hit information) which allows for tighter track matching with electromagnetic calorimeter clusters and reconstructed stubs in the muon detector for improved lepton identification.

3. Data samples and luminosity

The $W \to \ell\nu$ and $Z \to \ell\ell$ candidate event samples used to make the measurements reported here are selected from datasets collected using high E_T lepton trigger requirements. Additional data samples used in the evaluation of efficiencies and backgrounds are discussed in further detail in the corresponding subsequent sections. Here, we present the trigger requirements for events contained within the datasets from which our candidate samples are selected. We also briefly describe data processing, the event quality criteria applied to our data samples and the measurement of the integrated luminosities corresponding to our datasets.

3.1. Trigger requirements

The datasets used to select our candidate events are composed of events collected with well-defined trigger requirements at each of the three levels within the CDF trigger architecture (see section 2). The specific trigger requirements associated with the datasets used to make our measurements are summarized here. The measured efficiencies of these trigger requirements are presented in section 6.

3.1.1. Central electron trigger. The trigger requirements for the dataset used to select $W \to e\nu$ and $Z \to ee$ candidate events are described here. Both candidate samples are selected from central, high E_T electron triggered events, corresponding to the region $|\eta_{\rm det}| < 1.0$.

At level 1, energies in physical calorimeter towers of $0.1\times15^\circ$ in $\eta_{\rm det}$-ϕ space are first summed into $0.2 \times 15^\circ$ trigger towers. At least one trigger tower is required to have $E_T >$ 8 GeV and the ratio of the hadronic to electromagnetic energies in that tower, $E_{\rm had}/E_{\rm em}$, must be less than 0.125 (for measured $E_T < 14$ GeV). In addition, at least one COT track with $p_T > 8$ GeV/c pointing in the direction of the tower must be found by the XFT hardware.

A clustering algorithm is run at level 2 to combine associated energy deposits in neighboring calorimeter towers. Adjacent 'shoulder' towers with $E_T > 7.5$ GeV are added to the central 'seed' tower found at level 1. The total E_T of the cluster is required to be above 16 GeV and the $E_{\rm had}/E_{\rm em}$ ratio of the cluster is required to be less than 0.125. The presence of an XFT track with $p_T > 8$ GeV/c matched to the seed tower of the central cluster is also reconfirmed. Finally, in level 3 an electromagnetic cluster with $E_T > 18$ GeV and $E_{\rm had}/E_{\rm em} <$ 0.125 must be found by the offline reconstruction algorithm. A track pointing at the cluster

with $p_T > 9\,\text{GeV}/c$ must also be found by the full three-dimensional COT track reconstruction algorithm run in the level 3 processors.

At each level of the trigger, the rate of accepted events is significantly reduced. At typical luminosities ($\sim 2.5 \times 10^{31}\text{cm}^{-2}\text{s}^{-1}$), the accepted rate of events for the above trigger requirements are 25 Hz, 3 Hz and 1 Hz for levels 1, 2 and 3, respectively.

3.1.2. Central muon triggers. The dataset used to select our $W \to \mu\nu$ and $Z \to \mu\mu$ candidate samples is made of events collected using two analogous sets of trigger requirements. In the most central region of the detector ($|\eta_{\text{det}}| < 0.6$), trigger requirements are designed to select high p_T muon candidates which deposit hits in both the CMU and CMP wire chambers. An independent but similar set of requirements is used to collect high p_T candidates in the extended central region ($0.6 < |\eta_{\text{det}}| < 1.0$) which produce hits in CMX wire chambers.

The specific trigger requirements for the central region at level 1 are matched hits in one or more CMU projective wire pairs with arrival times within 124 ns of each other, a pattern of CMP hits on three of four layers consistent in ϕ with the observed CMU hits, and a matching COT track found by the XFT with $p_T > 4\,\text{GeV}/c$. For the early part of the run period corresponding to our datasets we make no additional requirements at level 2, but for the later portion we require at least one COT track with $p_T > 8\,\text{GeV}/c$ in the list of level 1 XFT tracks passed to the level 2 processor boards. Because no muon trigger information was available at level 2 during this run period, the higher p_T track was not required to match the CMU or CMP hits associated with the level 1 trigger. Finally for level 3, a reconstructed three-dimensional COT track with $p_T > 18\,\text{GeV}/c$ matched to reconstructed stubs in both the CMU and CMP chambers is required based on the offline reconstruction algorithms for muons.

The analogous trigger requirements for the extended central region at level 1 are matched hits in one or more CMX projective wire pairs with arrival times within 124 ns of each other and a matching COT track found by the XFT with $p_T > 8\,\text{GeV}/c$. For the latter part of our data collection period, a matching hit in the CSX scintillator counters consistent in time with a beam-produced particle is also required to help reduce the trigger rate from non-collision backgrounds. No additional requirements are made at level 2. In level 3, a reconstructed three-dimensional COT track with $p_T > 18\,\text{GeV}/c$ matched to a reconstructed stub in the CMX chambers is required based on the offline reconstruction algorithms for muons.

At typical luminosities ($\sim 2.5 \times 10^{31}\text{cm}^{-2}\,\text{s}^{-1}$), the accepted rate of events for the central trigger requirements is 30 Hz, 4 Hz and 0.15 Hz for levels 1, 2 and 3, respectively. For the extended central muon trigger requirements, the corresponding rates are 2 Hz, 2 Hz and 0.1 Hz.

3.2. Luminosity measurement

The total integrated luminosity (L) is derived from the rate of the inelastic $p\overline{p}$ events measured with CLC, $R_{p\overline{p}}$, the CLC acceptance, ϵ_{CLC} and the inelastic $p\overline{p}$ cross section at 1.96 TeV, σ_{in}, according to the expression

$$L = \frac{R_{p\overline{p}}}{\epsilon_{\text{CLC}} \cdot \sigma_{\text{in}}}. \tag{7}$$

The CLC acceptance is measured from tuned simulation and compared against the value obtained from a second method that relies on both data and simulation through the formula

$$\epsilon_{\text{CLC}} = \frac{N_{\text{EW}}}{N_{\text{CLC+Plug}}} \cdot \frac{N_{\text{CLC+Plug}}}{N_{\text{inelastic}}}, \tag{8}$$

Table 2. Systematic uncertainties in the luminosity calculation based on the CLC measurement and the combined value of the CDF and E811 inelastic cross-section measurements at $\sqrt{s} = 1.80$ TeV extrapolated to $\sqrt{s} = 1.96$ TeV. The total uncertainty in the CLC measurement is dominated by the uncertainty in the CLC acceptance. The detector instability and calibration uncertainties are components of the overall CLC measurement uncertainty and therefore not included in the calculation of the total uncertainty.

Effect	Uncertainty estimate
Inelastic cross section	4.0%
CLC Measurement	4.4%
Detector instability	<2.0%
Detector calibration	<1.5%
Total uncertainty	~6.0%

where $N_{\text{CLC+Plug}}$ is the number of inelastic events tagged by the CLC and plug calorimeter, N_{EW} is a subset of those which contain an east-west hit coincidence and pass the online selection criteria and $N_{\text{inelastic}}$ is the total number of inelastic collisions. The fraction $N_{\text{CLC+Plug}}/N_{\text{inelastic}}$ is extracted from simulation while the ratio $N_{\text{EW}}/N_{\text{CLC+Plug}}$ is measured from data. The acceptance calculated using this procedure is $\epsilon_{\text{CLC}} = 60.2 \pm 2.6\%$ which is in good agreement with the value obtained directly from simulation.

The value $\sigma_{\text{in}} = 60.7 \pm 2.4$ mb is obtained by extrapolating the combined result for the inelastic $p\overline{p}$ cross section at $\sqrt{s} = 1.8$ TeV based on CDF and E811 measurements (59.3 ± 2.3 mb) [58] to 1.96 TeV. Using these numbers and restricting ourselves to runs with a good detector status, the total luminosity of our datasets is estimated to be 72.0 ± 4.3 pb^{-1}. The 6% quoted uncertainty is dominated by the uncertainty in the absolute normalization of the CLC acceptance for a single $p\overline{p}$ inelastic collision [58]. The complete list of systematic uncertainties, including uncertainties from the inelastic cross section and luminosity detector, is given in table 2.

4. Event selection

We search for W bosons decaying into a highly energetic charged lepton ($\ell = e, \mu$) and a neutrino, which is identified via large $\not\!\!E_T$ in the detector. The $Z \to \ell\ell$ ($\ell = e, \mu$) events are selected based on the two energetic, isolated leptons originating from a single event vertex. The two leptons produced in the decays are oppositely charged, and the charge information for leptons is included as part of the selection criteria when available. The reconstructed dilepton invariant mass is also required to lie within a mass window consistent with the measured Z boson mass.

The complete set of selection criteria used to identify $W \to \ell\nu$ and $Z \to \ell\ell$ events are described here. As the selection of W and Z bosons proceeds from lepton identification, we also describe in some detail the variables used to select good lepton candidates.

4.1. Track selection

The track quality requirements are common to electron and muon selection. As the silicon tracking information is not vital to our measurements, we remove all silicon hits from the tracks and refit them, including the position of the beamline in the transverse direction as an

additional constraint in the fit. The beamline position is measured independently for each run period contributing to our datasets using the reconstructed COT track data contained within events from that period. The removal of silicon hits from tracks makes our measurements insensitive to the time-dependent efficiencies of the individual pieces of the silicon detector and allows us to include data from run periods when the silicon detector was not operational. The resulting beam-constrained COT tracks are used in the subsequent analysis work presented here. All of the kinematic track parameters used in these analyses with the one exception of the r–ϕ track impact parameter variable, d_0, used in muon selection, are based on these beam-constrained COT tracks.

The reconstructed tracks obtained using the method described above have small residual curvature biases primarily due to COT misalignments that are not currently corrected for in our offline tracking algorithms. We correct our track p_T measurement for misalignment effects based on the observed ϕ-dependence of the electron candidate E/p distribution (see section 4.2). The form of the correction is

$$\frac{Q}{p_T'} = \frac{Q}{p_T} - 0.000\,37 - 0.001\,10 \cdot \sin(\phi + 0.28), \tag{9}$$

where p_T' and p_T are the transverse momenta in GeV/c of the corrected and uncorrected track, respectively, Q is the charge of the track and ϕ is given in radians.

We apply additional selection criteria on our reconstructed tracks to ensure that only high-quality tracks are assigned to lepton candidates. Each track is required to pass a set of minimum hit criteria. The reconstructed tracks are required to have a minimum of seven out of twelve possible hits on at least three of four axial and stereo superlayers within the COT. The minimum hit criteria for reconstructed tracks is less restrictive than that used to select level 1 trigger track candidates (see section 2.6) to ensure high selection efficiencies for both triggerable and non-triggerable track candidates in our events. In addition, to restrict ourselves to a region of high track reconstruction efficiency, we require the z coordinate of the lepton track intersection with the beam axis in the r–z plane, z_0, be within 60 cm of the center of the detector.

To help reduce real muon backgrounds from cosmic rays and π/K decays, we impose additional quality requirements on muon track candidates. For muon track candidates only, we incorporate silicon hit information in track reconstruction when available to calculate a more precise value for the r–ϕ impact parameter of the track, d_0. Cosmic ray muons and muons produced in π/K decays are less likely to point back to the event vertex and therefore will typically have larger measured impact parameters. We apply different cuts on the d_0 of muon track candidates depending on whether or not the tracks contain any silicon hit information; $|d_0| < 0.2$ cm for tracks with no silicon hits and $|d_0| < 0.02$ cm for tracks with silicon hits. We also make a requirement on the quality of the final COT beam-constrained track fit for muon candidates. The track fit for muon backgrounds not originating from the event vertex will typically be worse when the additional constraint of the beamline position is included. For muon track candidates we require that $\chi^2/n_{\text{df}} < 2.0$ where n_{df} is the number of degrees of freedom in the track fit (the number of hits on the fitted track minus the five free parameters of the fit).

We additionally restrict muon track candidates in θ to ensure that the tracks lie in a fiducial region of high trigger and reconstruction efficiency well modeled by our detector simulation. We require that each muon track passes through all eight COT superlayers by making a minimum requirement on the exit radius of the track at the endplates of the COT tracking chamber. The exit radius is defined as

$$\rho_{\text{COT}} = (z_{\text{COT}} - z_0) \cdot \tan\theta, \tag{10}$$

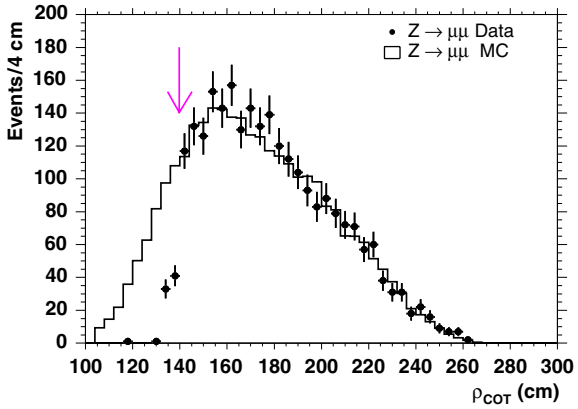

Figure 5. The COT exit radius for CMX muons in $Z \rightarrow \mu\mu$ candidate events. The points are the data and the histogram is simulation. The selected CMX muons from data events are required to satisfy the high p_T muon trigger criteria, but no trigger requirement is made on the muons selected from simulation. The two histograms are normalized to have the same number of events over the region 150 cm $< \rho_{\rm COT} <$ 280 cm. The arrow indicates the location of the muon track selection cut made on the $\rho_{\rm COT}$ variable.

Table 3. Summary of track selection requirements.

Variable	Cut
All tracks:	
# Axial COT superlayers	$\geqslant$3 with $\geqslant$7 hits
# Stereo COT superlayers	$\geqslant$3 with $\geqslant$7 hits
$\lvert z_0 \rvert$	$<$60 cm
Muon tracks:	
$\lvert d_0 \rvert$	$<$0.2 cm (no silicon hits)
$\lvert d_0 \rvert$	$<$0.02 cm (silicon hits)
$\chi^2/n_{\rm df}$	$<$2.0
$\rho_{\rm COT}$	$>$140 cm

where $z_{\rm COT}$ is the distance of the COT endplates from the center of the detector (155 cm for tracks with $\eta > 0$ and -155 cm for those with $\eta < 0$). Here, η and θ are the previously defined pseudorapidity and polar angle of the track with respect to the directions of the colliding beams. A comparison of the $\rho_{\rm COT}$ distribution for CMX muons from $Z \rightarrow \mu\mu$ candidate events in data and Monte Carlo (MC) simulation (see section 5) is shown in figure 5. The distributions do not match in the region $\rho_{\rm COT} < 140$ cm due to a loss of data events in this region originating from the XFT track trigger requirements, at least ten (or eleven) hits out of a possible twelve for each of the four axial COT superlayers, which is not accounted for in the simulation. Based on this comparison, we require $\rho_{\rm COT} > 140$ cm for muon track candidates.

Track selection requirements are summarized in table 3. Distributions of the track quality variables used in the selection of all lepton tracks are shown in figure 6, and those used solely in the selection of muon tracks are shown in figure 7. The distributions are constructed from second, unbiased lepton legs in $Z \rightarrow \ell\ell$ candidate data events. Based on these distributions, we expect the measured inefficiencies of our track selection criteria (see section 6) to be on the order of a few percent.

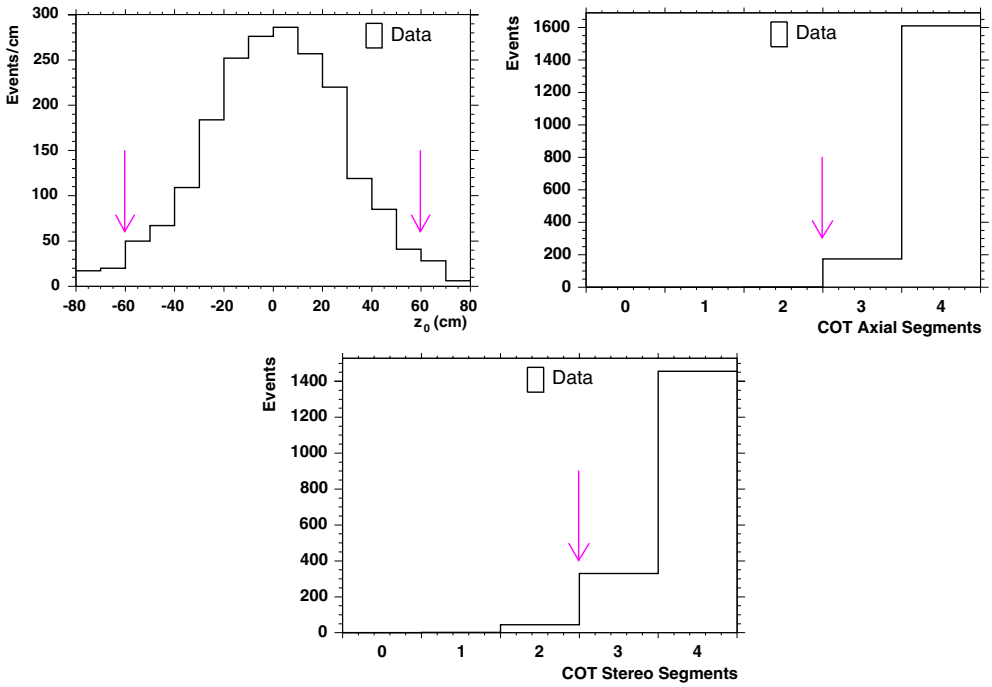

Figure 6. Distributions of the z_0 and number of axial and stereo COT superlayers contributing seven or more hits. These track quality variables are from unbiased, second lepton legs of $Z \to \ell\ell$ candidate events in data. The arrows indicate the locations of selection cuts applied on these variables.

4.2. Electron selection

Electron candidates are reconstructed in either the central barrel or forward plug calorimeters. The clustering algorithms and selection criteria used to identify electrons in the two sections are different, as we do not make use of tracking information in the forward detector region ($|\eta_{\text{det}}| > 1$) where stand-alone track reconstruction is less reliable due to the smaller number of available tracking layers. Here, we discuss the specific identification criteria for both central and plug electrons.

4.2.1. Central electron identification. Electron objects are formed from energy clusters in neighboring towers of the calorimeter. An electron cluster is made from an electromagnetic seed tower and at most one additional tower that is adjacent to the seed tower in η_{det} and within the same ϕ wedge. The seed tower must have $E_T > 2$ GeV and a reconstructed COT track which extrapolates to that tower. The hadronic energy in the corresponding towers is required to be less than 0.125 times the electromagnetic energy of the cluster.

Electron candidates for these measurements must lie within the well-instrumented regions of the calorimeter. The cluster position within the calorimeter is determined by the location of the associated CES shower. The CES shower must lie within 21 cm of the tower center in the r–ϕ view for the shower to be fully contained within the active region. We also exclude electrons reconstructed in the region where the two halves of the central calorimeter meet ($|z| < 9$ cm) and the outer half of the most forward CEM towers ($|z| > 230$ cm) where

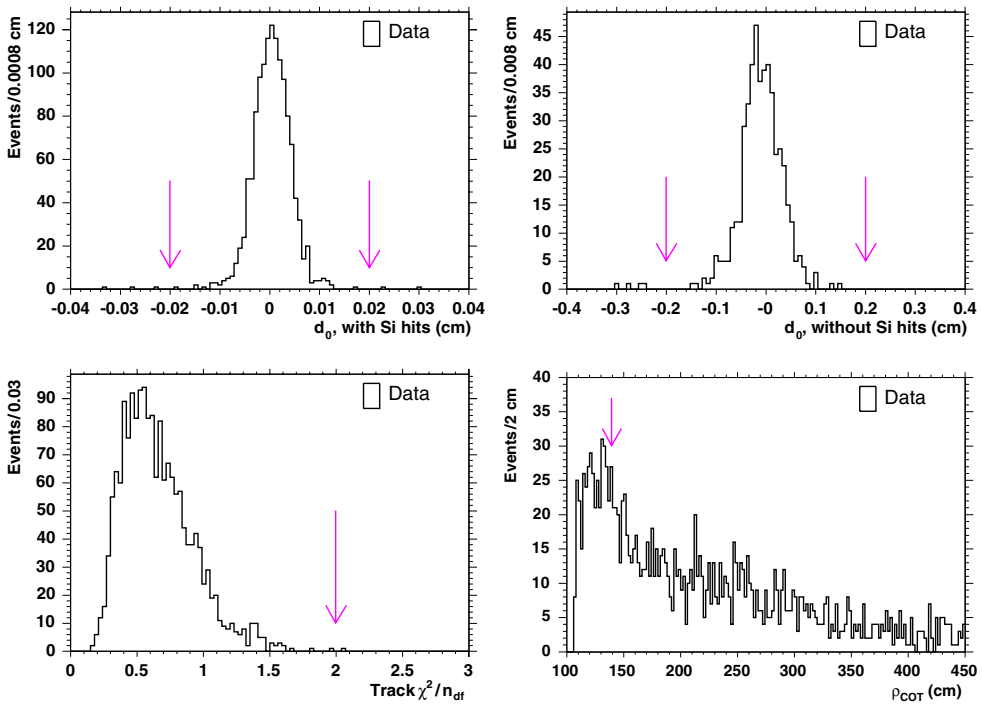

Figure 7. Distributions of the d_0 (with and without attached silicon hits), $\chi^2/n_{\rm df}$, and $\rho_{\rm COT}$. These track quality variables are for muons from unbiased, second muon legs of $Z \rightarrow \mu\mu$ candidate events in data. The arrows indicate the locations of selection cuts applied on these variables.

Table 4. Calorimeter variables and electron identification requirements.

Variable	Cut
Central	$\lvert\eta_{\rm det}\rvert < 1.0$
$E_{\rm had}/E_{\rm em}$	$<0.055 + 0.00045 \cdot E$[GeV]
E/p (for $E_T < 100$ GeV)	<2.0
$L_{\rm shr}$	<0.2
$Q \cdot \Delta x$	>-3.0 cm, < 1.5 cm
$\lvert\Delta z\rvert$	<3.0 cm
$\chi^2_{\rm strips}$	<10.0
Plug	$1.2 < \lvert\eta_{\rm det}\rvert < 2.8$
$E_{\rm had}/E_{\rm em}$	<0.05
$\chi^2_{\rm PEM}$	<10.0

there is substantial electron shower leakage into the hadronic part of the calorimeter. Finally, we exclude events in which the electron is reconstructed near the uninstrumented region surrounding the cryogenic connections to the solenoidal magnet ($0.77 < \eta_{\rm det} < 1.0, 75^\circ < \phi < 90^\circ$ and $|z| > 193$ cm).

The selection requirements listed in table 4 are applied to electron candidates in the well-instrumented regions of the central calorimeter. We cut on the ratio of the hadronic to electromagnetic energies, $E_{\rm had}/E_{\rm em}$, for the candidate clusters. Electron showers are typically

contained within the electromagnetic calorimeter, while hadron showers spread across both the hadronic and electromagnetic sections of the calorimeter. We require $E_{\text{had}}/E_{\text{em}} < 0.055 + 0.000\,45 \cdot E$ where E is the total energy of the cluster in GeV. The linear term in our selection criteria accounts for the increased shower leakage of higher energy electrons into the hadronic calorimeter sections.

We also cut on the ratio of the electromagnetic cluster transverse energy to the COT track transverse momentum, E/p. This ratio is nominally expected to be unity, but in cases where the electron radiates a photon in the material of the inner tracking volume, the measured momentum of the COT track can be less than the measured energy of the corresponding cluster in the calorimeter. In cases where the electron is highly energetic, the photon and electron will be nearly collinear and are likely to end up in the same calorimeter tower. The measured COT track momentum will, however, correspond to the momentum of the electron after emitting the photon and thus be smaller than the original electron momentum. We require $E/p < 2.0$ which is efficient for the majority of electrons which emit a bremsstrahlung photon. Since this cut becomes unreliable for very large values of track p_T, we do not apply it to electron clusters with $E_T > 100$ GeV.

The lateral shower profile variable, L_{shr} [37], is used to compare the distribution of adjacent CEM tower energies in the cluster as a function of seed tower energy to shapes derived from electron test-beam data. We also perform a χ^2 comparison of the CES lateral shower profile in the r–z view to the profile extracted from the electron test-beam data. For central electrons, we require $L_{\text{shr}} < 0.2$ and $\chi^2_{\text{strips}} < 10.0$.

Since central electron candidates include a COT track, we can further reduce electron misidentification by cutting on track-shower matching variables. We define $Q \cdot \Delta x$ as the distance in the r–ϕ plane between the extrapolated beam-constrained COT track and the CES cluster multiplied by the charge of the track to account for asymmetric tails originating from bremsstrahlung radiation. The variable Δz is the corresponding distance in the r–z plane. We require $-3.0\text{ cm} < Q \cdot \Delta x < 1.5\text{ cm}$ and $|\Delta z| < 3.0$ cm.

Distributions of central electron identification variables are shown in figures 8 and 9. The plotted electron candidates are the unbiased, second electron legs in $Z \rightarrow ee$ events in which both electrons are reconstructed within the central calorimeter and the first electron is found to satisfy the full set of identification criteria. Based on these distributions, we expect a high efficiency for our central electron selection criteria (see section 6).

4.2.2. Plug electron identification. Electron candidate clusters in the plug calorimeter are made from a seed tower and neighboring towers within two towers in η_{det} and ϕ from the seed tower. As for central electrons, the hadronic energy of the cluster is required to be less than 0.125 times the electromagnetic energy. We also require plug electrons to be reconstructed in a well-instrumented region of the detector, defined as $1.2 < |\eta_{\text{det}}| < 2.8$.

The additional selection criteria applied to plug electron candidates are summarized in table 4. Fewer variables are available for selecting plug electrons due to the lack of matching track information for candidates in the forward region of the detector. As in the case of central electrons, we cut on the ratio of hadronic to electromagnetic energies in the cluster, $E_{\text{had}}/E_{\text{em}}$, which is required to be less than 0.05. We also compare the distribution of tower energies in a 3×3 array around the seed tower to distributions from electron test-beam data, forming the variable χ^2_{PEM} which we require to be less than 10.0. Distributions of the plug electron selection variables are shown in figure 10. The plotted electron candidates are the unbiased, second plug electron legs in $Z \rightarrow ee$ events in which the first electron is reconstructed within the central calorimeter and found to satisfy a set of more restrictive cuts on the previously described central electron identification variables.

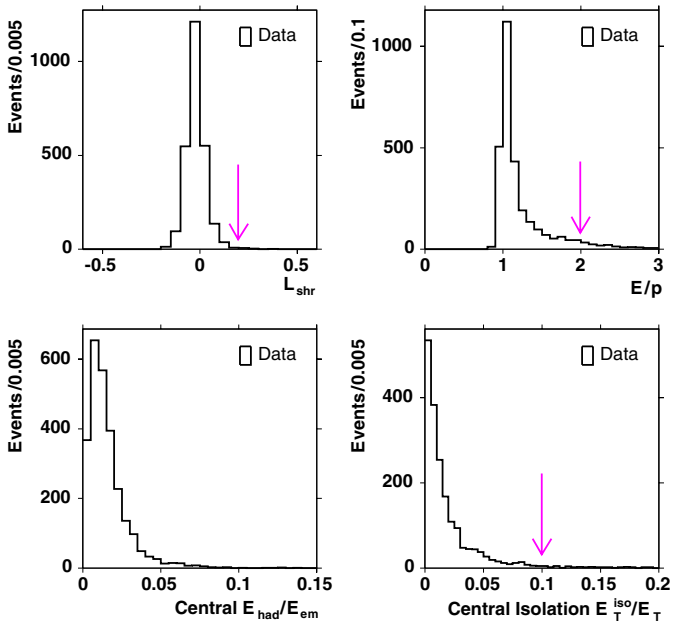

Figure 8. Distributions of $L_{\rm shr}$, E/p, $E_{\rm had}/E_{\rm em}$ and $E_T^{\rm iso}/E_T$ (see section 4.4) central calorimeter electron selection variables from unbiased, second electron legs of $Z \rightarrow ee$ candidate events in data. The arrows indicate the locations of selection cuts applied on these variables. No arrow is shown on the $E_{\rm had}/E_{\rm em}$ distribution since the cut on this variable is dependent on the electron energy.

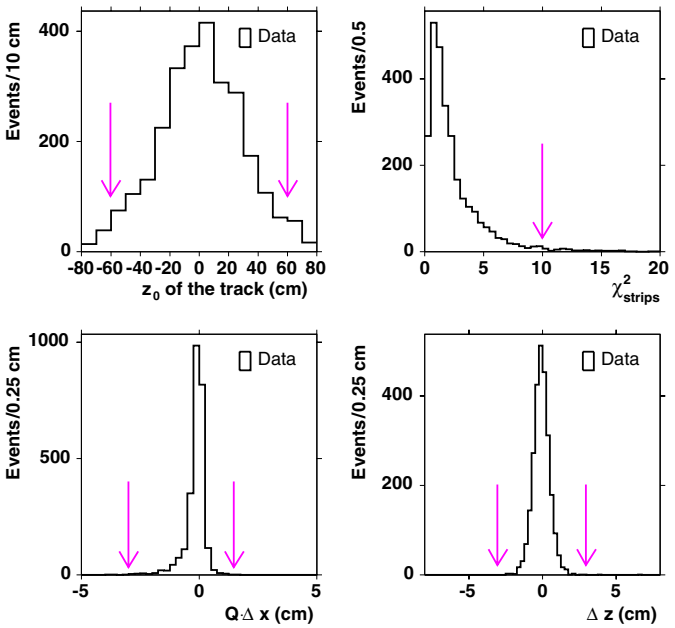

Figure 9. Distributions of the z_0, $\chi^2_{\rm strips}$, $Q \cdot \Delta x$ and Δz central calorimeter electron selection variables from unbiased, second electron legs of $Z \rightarrow ee$ candidate events in data. The arrows indicate the locations of selection cuts applied on these variables.

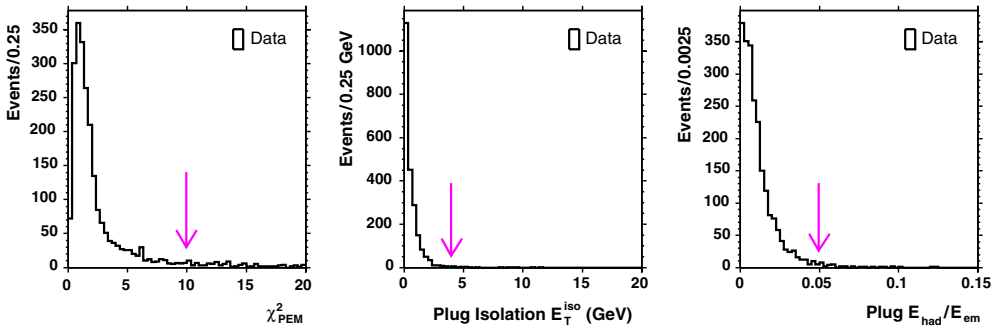

Figure 10. Distributions of the χ^2_{PEM}, E_T^{iso} (see section 4.4) and $E_{\text{had}}/E_{\text{em}}$ plug calorimeter electron selection variables from unbiased, second electron legs of $Z \to ee$ candidate events in data. The arrows indicate the locations of selection cuts applied on these variables.

4.3. Muon selection

Muon candidates used in these measurements must have reconstructed stubs in both the CMU and CMP chambers (CMUP muons) or a reconstructed stub in the CMX chambers. CMX chambers were offline for the first 16.5 pb^{-1} of integrated luminosity corresponding to our datasets, and the reduced muon detector coverage during this period is taken into account in our measured acceptances for events in the muon candidate samples (see section 5.3). The muon candidate tracks are required to extrapolate to regions of the muon chambers with high single wire hit efficiencies to ensure that chamber-edge effects do not contribute to inefficiencies in muon stub-reconstruction and stub-track matching (see section 6). We measure the location of an extrapolated muon track candidate with respect to the drift direction (local x) and wire axis (local z) of a given chamber. The extrapolation assumes that no multiple scattering takes place, and in some cases muons that leave hits in the muon detectors extrapolate to locations outside of the chambers. In the CMP and CMX chambers, we require that the extrapolation is within the chamber volume in local x and at least 3 cm away from the edges of the chamber volume in local z. Studies of unbiased muons in $Z \to \mu\mu$ events show that these regions of chambers are maximally efficient for hit-finding. No such requirement is needed for the CMU chambers. Some sections of the upgraded muon detectors were not yet fully commissioned for the period of data-taking corresponding to our datasets, and we exclude all muon candidates with stubs in those sections.

The selection criteria applied to muon candidates are summarized in table 5. We require that the measured energy depositions in the electromagnetic and hadronic sections of the calorimeters along the muon candidate trajectory, E_{em} and E_{had}, are consistent with those expected from a minimum-ionizing particle. The positions of the reconstructed chamber stubs are required to be near the locations of the extrapolated tracks. The track-stub matching variable $|\Delta X|$ is the distance in the r–ϕ plane between the extrapolated COT track and the CMU, CMP, or CMX stub. Figure 11 shows the ΔX distributions for unbiased, CMU, CMP and CMX second muons in $Z \to \mu\mu$ events.

Energetic cosmic ray muons traverse the detector at a significant rate, depositing hits in both muon chambers and the COT, and can in a small fraction of cases satisfy the requirements of the high p_T muon trigger paths and the offline selection criteria. We remove cosmic ray events from our sample using the previously discussed track quality cuts for muon candidates and a cosmic ray tagging algorithm (see section 7.5) based on COT hit timing information.

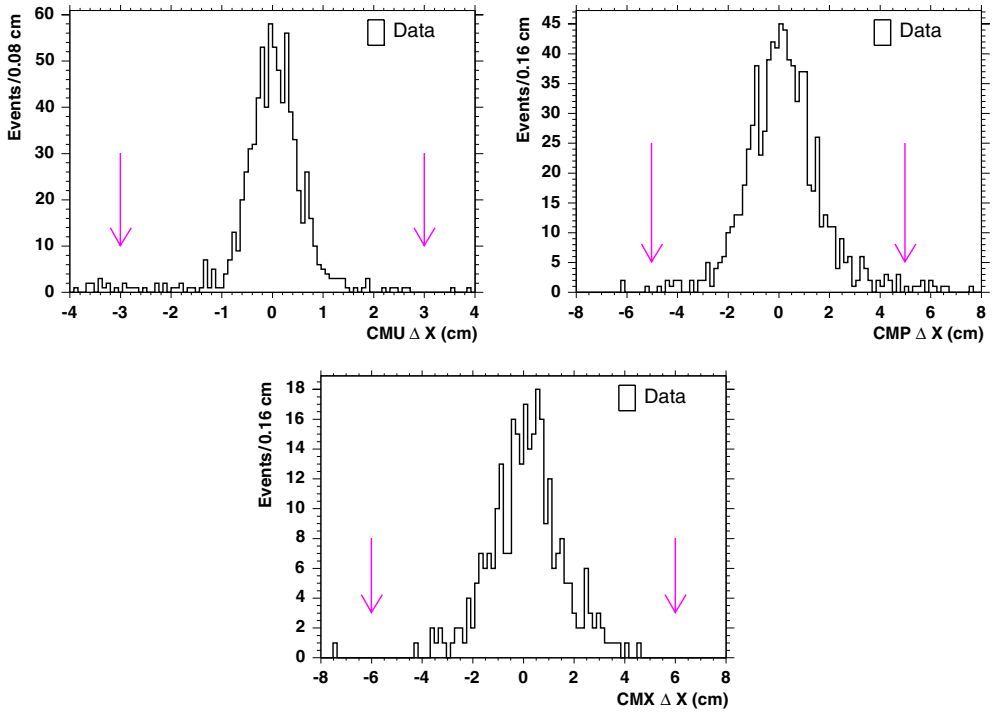

Figure 11. Distributions of the CMU, CMP and CMX ΔX muon selection variables from unbiased, second muon legs of $Z \rightarrow \mu\mu$ candidate events in data. The arrows indicate the locations of selection cuts applied on these variables.

Table 5. Calorimeter and muon chamber variables used in muon identification. The fiducial distance variables are defined as the extrapolated position of the muon track candidate with respect to the edges of a given muon chamber. The fiducial distance is negative if this position lies within the chamber and positive otherwise. CMUP muon candidates are those with reconstructed stubs in both the CMU and CMP detectors. CMX muon candidates have reconstructed stubs in the CMX detector.

Variable	Cut
Minimum ionizing cuts:	(GeV)
$E_{\rm em}$ ($p \leqslant 100$ GeV/c)	<2
$E_{\rm em}$ ($p > 100$ GeV/c)	$<2 + (p - 100) \cdot 0.0115$
$E_{\rm had}$ ($p \leqslant 100$ GeV/c)	<6
$E_{\rm had}$ ($p > 100$ GeV/c)	$<6 + (p - 100) \cdot 0.0280$
Muon stub cuts:	(cm)
$\lvert\Delta X_{\rm CMU}\rvert$ (CMUP)	<3.0
$\lvert\Delta X_{\rm CMP}\rvert$ (CMUP)	<5.0
$\lvert\Delta X_{\rm CMX}\rvert$ (CMX)	<6.0
CMP x-fiducial distance (CMUP)	<0.0
CMP z-fiducial distance (CMUP)	< -3.0
CMX x-fiducial distance (CMX)	<0.0
CMX z-fiducial distance (CMX)	< -3.0

4.4. $W \to \ell\nu$ selection

$W \to \ell\nu$ events are selected by first requiring a high-p_T charged lepton in the central detectors, as described above. Electrons must have electromagnetic-cluster E_T greater than 25 GeV and COT track p_T greater than 10 GeV/c. Muons must have COT track p_T greater than 20 GeV/c. The leptons from decays of W and Z bosons are often isolated from hadronic jets, in contrast to leptons originating from decays of heavy-flavor hadrons. We therefore require that the calorimeter energy in a cone of radius $\Delta R = \sqrt{\Delta\eta^2 + \Delta\phi^2} \leqslant 0.4$ around the lepton excluding the energy associated with the lepton, E_T^{iso}, be less than 10% the energy of the lepton (E_T for electrons and p_T for muons). Figure 8 shows the isolation distribution for unbiased central electrons from $Z \to ee$ decays.

We also require evidence for a neutrino in W candidate events in the form of an imbalance of the measured momentum of the event since neutrinos do not interact with our detector. The initial state of the colliding partons has $p_T \simeq 0$, but unknown p_z due to the unknown value of initial parton momentum. Therefore, we identify the missing transverse energy, $\not\!\!E_T$, in the event with the p_T of the neutrino. In muon events, we correct the $\not\!\!E_T$ measured in the calorimeter to account for the energy carried away by the muon, a minimum-ionizing particle. The muon momentum is used in place of the calorimeter energy deposits observed along the path of the muon. For $W \to \mu\nu$ candidate events we require $\not\!\!E_T > 20$ GeV and tighten the requirement for $W \to e\nu$ events, $\not\!\!E_T > 25$ GeV, to further reduce backgrounds from hadron jets.

A background to $W \to \ell\nu$ is the $Z \to \ell\ell$ channel, when one of the leptons falls into an uninstrumented region of the detector, creating false $\not\!\!E_T$. This is a bigger problem in the muon channel since the coverage of the muon detectors is in general less uniform than that of the calorimeter. Therefore, in the muon channel we reject events with additional minimum-ionizing tracks in the event with $p_T > 10$ GeV/c, $E_{\text{em}} < 3$ GeV ($E_{\text{em}} < 3 + 0.0140 \cdot (p - 100)$ GeV if $p > 100$ GeV/c) and $E_{\text{had}} < 6$ GeV ($E_{\text{had}} < 6 + 0.0420 \cdot (p - 100)$ GeV if $p > 100$ GeV/c). Studies of simulated $W \to \mu\nu$ and $Z \to \mu\mu$ event samples (see section 5) show that this additional rejection criteria removes 54.7% of the $Z \to \mu\mu$ background while retaining 99.6% of the $W \to \mu\nu$ signal. Further discussion of backgrounds to the $W \to \ell\nu$ channels is found in section 7.

4.5. $Z \to \ell\ell$ selection

We select events which contain an electron or muon that passes the same identification requirements as the lepton in $W \to \ell\nu$ candidate events. As described in section 1, systematic uncertainties are reduced by using a common lepton selection in the W and Z analyses. We identify a second lepton in these events using less restrictive ('loose') selection criteria to increase our $Z \to \ell\ell$ detection efficiency. The invariant mass of the two leptons is required to be between 66 and 116 GeV/c^2.

After selecting the first electron, $Z \to ee$ events are identified by the presence of another isolated electron in the central calorimeter with $E_T > 25$ GeV passing less restrictive selection criteria or an isolated electron in the plug calorimeter with $E_T > 20$ GeV. The selection criteria for each type of electron are summarized in table 6. In the calculation of E_T for the plug electron, the z-vertex is taken from the COT track of the central electron in the event. In the case of two central electrons, we also require they be oppositely charged, with both electron tracks passing the track quality criteria listed in table 3.

After selecting the first muon, $Z \to \mu\mu$ events are identified by the presence of another oppositely charged, isolated muon track with $p_T > 20$ GeV originating from a common

Table 6. $Z \rightarrow ee$ selection criteria.

Variable	'Tight' central e	'Loose' central e	Plug e
E_T	>25 GeV	>25 GeV	>20 GeV
p_T	>10 GeV/c	>10 GeV/c	
E_T^{iso}	$<0.1 \cdot E_T^{\text{cluster}}$	$<0.1 \cdot E_T^{\text{cluster}}$	<4 GeV
$E_{\text{had}}/E_{\text{em}}$	$<0.055 + 0.000\,45 \cdot \text{E}$	$<0.055 + 0.000\,45 \cdot \text{E}$	<0.05
E/p	<2.0 (or $p_T > 50$ GeV/c)		
L_{shr}	<0.2		
$Q \cdot \Delta x$	> -3.0cm, < 1.5 cm		
$\lvert\Delta z\rvert$	<3.0 cm		
χ^2_{strips}	<10.0		
χ^2_{PEM}			<10.0

Table 7. $Z \rightarrow \mu\mu$ selection criteria.

Variable	Cut
Fiducial and kinematic:	
$\lvert\eta_\mu^{(1)}\rvert$	<1.0 (CMUP+CMX)
$\lvert\eta_\mu^{(2)}\rvert$	<1.2 (Track)
$p_T^{\mu(1)}$	>20 GeV/c
$p_T^{\mu(2)}$	>20 GeV/c
Both muon legs:	
E_{em} ($p \leqslant 100$ GeV/c)	<2 GeV
E_{em} ($p > 100$ GeV/c)	$<2 + (p - 100) \cdot 0.0115$ GeV
E_{had} ($p \leqslant 100$ GeV/c)	<6 GeV
E_{had} ($p > 100$ GeV/c)	$<6 + (p - 100) \cdot 0.0280$ GeV
E_T^{iso}	$<0.1 \cdot p_T$
First muon leg:	
$\lvert\Delta X_{\text{CMU}}\rvert$	<3.0 cm (CMUP)
$\lvert\Delta X_{\text{CMP}}\rvert$	<5.0 cm (CMUP)
$\lvert\Delta X_{\text{CMX}}\rvert$	<6.0 cm (CMX)
CMP x-fiducial distance	<0.0 cm (CMUP)
CMP z-fiducial distance	<-3.0 cm (CMUP)
CMX x-fiducial distance	<0.0 cm (CMX)
CMX z-fiducial distance	<-3.0 cm (CMX)

vertex. The muon-stub criteria are dropped for the second leg to gain signal acceptance with very little increase in background; this second muon is merely a minimum-ionizing track. Table 7 shows the complete set of selection criteria used to identify $Z \rightarrow \mu\mu$ events. Again, we require both tracks to pass the track requirements of table 3.

4.6. Event selection summary

Using the selection criteria described here, we find a total of 37 584 $W \rightarrow e\nu$ candidate events. In the muon channel, we find 21 983 W boson candidates with CMUP muons and 9739 with CMX muons for a grand total of 31 722 $W \rightarrow \mu\nu$ candidates. In the Z boson decay

channel, we find 1730 events with two reconstructed electrons in the central calorimeter and 2512 events in which the second electron is reconstructed in the plug calorimeter giving a total of 4242 $Z \to ee$ candidates. From our high p_T muon dataset, we find 1371 CMUP + track and 677 CMX + track $Z \to \mu\mu$ candidates. There is an overlap of 263 events between these two samples in which one candidate track is matched to stubs in the CMU and CMP muon chambers and the other is matched to a stub in the CMX chamber. Taking this overlap into account, we obtain a total of 1785 $Z \to \mu\mu$ candidate events.

5. Signal acceptance

5.1. Introduction

The acceptance terms in equations (5) and (6) are defined as the fraction of $W \to \ell\nu$ or $Z \to \ell\ell$ events produced in $p\overline{p}$ collisions at $\sqrt{s} = 1.96$ TeV that satisfy the geometrical and kinematic requirements of our samples. Lepton reconstruction in our detector is limited by the finite fiducial coverage of the tracking, calorimeter and muon systems. Several kinematic requirements are also made on candidate events to help reduce backgrounds from non-W/Z processes. The reconstructed leptons in these events are required to pass minimum calorimeter cluster E_T and/or track p_T criteria. In addition, a minimum requirement on the total measured missing E_T is made on events in our $W \to \ell\nu$ candidate samples, and the invariant mass of $Z \to \ell\ell$ candidate events is restricted to a finite range around the measured Z boson mass.

The fraction of signal events that satisfy the geometrical and kinematic criteria outlined above for each of our samples is determined using simulation. One geometrical cut on candidate events for which we measure the acceptance directly from data is the requirement that the primary event vertex for each event lies within 60.0 cm of the detector origin along the z-axis (parallel to the direction of the beams). Our simulation does include a realistic model of the beam interaction region, but we obtain a more accurate estimation of the selection efficiency for the event vertex requirement from studies of minimum bias events in the data as described in section 6. Since the geometrical and kinematic acceptance for candidate events with a primary vertex outside our allowed region is significantly smaller, we remove the subset of simulated events with vertices outside this region from our acceptance calculations to avoid double-counting correlated inefficiencies.

There is one additional complication involved in determining the kinematic and geometrical acceptances for our $Z \to \ell\ell$ candidate samples. Because we make our $\gamma^*/Z \to \ell\ell$ production cross-section measurements in a specific invariant mass range, 66 GeV/c^2–116 GeV/c^2, we need to account for events outside this mass range that are reconstructed in the detector to sit within this range due to the effects of detector resolution and final state radiations. To include events of this type in our acceptance calculations, we use simulated $\gamma^*/Z \to \ell\ell$ event samples generated over a wider invariant mass range ($M_{\ell\ell} >$ 30 GeV/c^2). In order for an event to contribute to the denominator of our acceptance calculations, we require that the invariant mass of the lepton pair at the generator level prior to application of final state radiative effects lies within the range of our measurement (66 GeV/c^2 $< M_{\ell\ell} <$ 116 GeV/c^2). The generator-level invariant mass requirement is not made on events contributing to the numerator of our acceptance calculations, however, so that $\gamma^*/Z \to \ell\ell$ events generated outside the invariant mass range of our measurement which have reconstructed masses within this range are properly accounted for in the acceptance calculations.

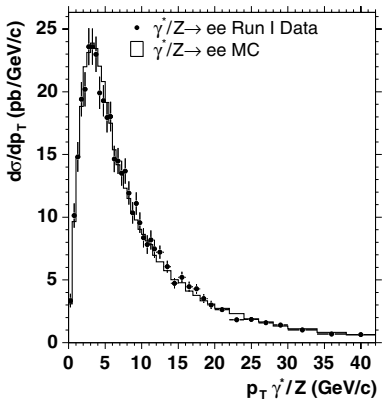

Figure 12. Tuned PYTHIA 6.21 $\mathrm{d}\sigma/\mathrm{d}p_T$ in pb per GeV/c (on average) of $\gamma^*/Z \to ee$ pairs in the mass region 66 GeV/c^2 $< M_{ee} <$ 116 GeV/c^2 (histogram) versus the measurement made by CDF in Run I (points).

5.2. Event and detector simulation

The simulated events used to estimate the acceptance of our samples were generated with PYTHIA 6.203 [59]. The default set of parton distribution functions (PDFs) used in the generation of these samples is CTEQ5L [60]. PYTHIA generates the hard, leading-order (LO) QCD interaction, $q + \bar{q} \to \gamma^*/Z$ (or $q + \bar{q}' \to W$), simulates initial-state QCD radiation via its parton-shower algorithms and generates the decay, $\gamma^*/Z \to \ell\ell$ (or $W \to \ell\nu$). No restrictions were placed at the generator level on the p_T of the final-state leptons or on their pseudorapidity. Both initial- and final-state radiation were turned on in the event simulation. In order to model the data accurately, the beam energy was set to 980 GeV, and the beam parameters were adjusted to provide the best possible match with data. The profile of the beam interaction region in z was matched to data by setting the mean of the vertex distribution to 3.0 cm in the direction along the beams and the corresponding Gaussian spread to 25.0 cm. The offset of the beam from the nominal center of the detector in the r–ϕ plane is also taken into account. In the simulation, the position of the beams at $z = 0$ is offset by -0.064 cm in x and +0.310 cm in y to provide a rough match with the measured offsets in data. The location of a given vertex within the r–ϕ plane is also observed to depend on its location along the z-axis due to the non-zero angle between the beams and the central axis of the detector. Slopes of $-0.000\,21$ and $0.000\,31$ are assigned in the simulation to the direction of the beams relative to the y–z and x–z detector planes to model this effect.

The intermediate vector boson p_T distribution in the simulation is tuned to match the CDF Run I measurement of the $\mathrm{d}\sigma/\mathrm{d}p_T$ spectrum for electron pairs in the invariant mass range between 66 GeV/c^2 and 116 GeV/c^2 [61]. The tuning is done using PYTHIA's nonperturbative 'K_T smearing' parameters, PARP(91) and PARP(93), and shower evolution Q^2 parameters, PARP(62) and PARP(64). The PARP(91) parameter affects the location of the peak in the $\mathrm{d}\sigma/\mathrm{d}p_T$ distribution in the vicinity of 3 GeV/c, and the PARP(62) and PARP(64) parameters affect the shape of the distribution in the region between 7 GeV/c and 25 GeV/c. A comparison between the 'tuned' $\gamma^*/Z p_T$ distribution from simulation and the measured Run I spectrum is shown in figure 12. We assume that the optimized PYTHIA tuning parameters obtained from data collected at the Run I center-of-mass energy ($\sqrt{s} = 1.80$ TeV) remain valid at the increased Run II center-of-mass energy ($\sqrt{s} = 1.96$ TeV). The underlying event model in PYTHIA is also tuned based on observed particle distributions in minimum bias events [62].

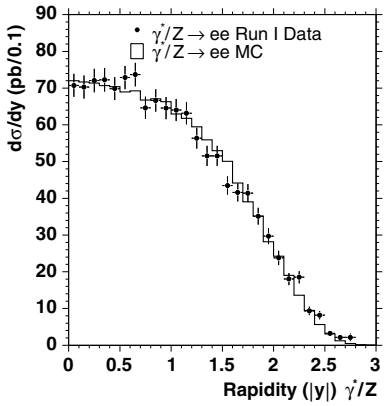

Figure 13. Tuned PYTHIA 6.21 $\mathrm{d}\sigma/\mathrm{d}y$ in pb per 0.1 of $\gamma^*/Z \to ee$ pairs in the mass region $66\ \text{GeV}/c^2 < M_{ee} < 116\ \text{GeV}/c^2$ (histogram) versus the measurement made by CDF in Run I (points).

Table 8. $W \to e\nu$ selection acceptance from PYTHIA Monte Carlo simulation. Statistical uncertainties are shown.

Selection criteria	Number of events	Net acceptance
Total events	1933 957	–
$\lvert z_{\text{vtx}}\rvert < 60$ cm	1870 156	–
Central EM cluster	927 231	0.4958 ± 0.0004
Calorimeter fiducial cuts	731 049	0.3909 ± 0.0004
Electron track $p_T > 10\ \text{GeV}/c$	647 691	0.3463 ± 0.0003
EM cluster $E_T > 25$ GeV	488 532	0.2612 ± 0.0003
Event $\not\!\!E_T > 25$ GeV	447 836	0.2395 ± 0.0003

The shape of the boson rapidity distribution is strongly dependent on the choice of PDFs. The shape of the $\mathrm{d}\sigma/\mathrm{d}y$ distribution for $\gamma^*/Z \to ee$ pairs in the mass region, $66\ \text{GeV}/c^2 < M_{ee} < 116\ \text{GeV}/c^2$, was measured by CDF in Run I [29]. The good agreement observed between the measured shape of $\mathrm{d}\sigma/\mathrm{d}y$ with that obtained from simulation using CTEQ5 L PDFs motivates the selection of this PDF set for our event generation. A comparison between the shape of the Run I measured $\mathrm{d}\sigma/\mathrm{d}y$ distribution and the shape of the same distribution from PYTHIA 6.21 simulated event samples generated with CTEQ5 L is shown in figure 13.

A detector simulation based on GEANT3 [63, 64] is used to model the behavior of the CDF detector. The GFLASH [65] package is used to decrease the simulation time of particle showers within the calorimeter.

5.3. *Signal acceptances from* PYTHIA

Additional tuning is performed after detector simulation to improve modeling of the data further. A detailed description of the techniques used to determine the post-simulation tunings described here and the associated acceptance uncertainties is provided in sections 5.8 and 5.9.

The tuned, simulated event samples are used to determine the acceptances of each W and Z event sample. As discussed in section 5.1, events with a primary event vertex outside our allowed region ($|z_{\text{vtx}}| < 60$ cm) are removed from both the numerator and denominator of

Table 9. $W \to \mu\nu$ selection acceptance from PYTHIA Monte Carlo simulation. Statistical uncertainties are shown.

Selection criteria	Number of events	Net acceptance
Total events	2017 347	–
$\lvert z_{\rm vtx}\rvert < 60$ cm	1951 450	–
CMUP or CMX Muon	545 221	0.2794 ± 0.0003
Muon chamber fiducial cuts	523 566	0.2683 ± 0.0003
Muon track $p_T > 20$ GeV/c	435 373	0.2231 ± 0.0003
Muon track fiducial cuts	411 390	0.2108 ± 0.0003
Event $\not\!\!E_T > 20$ GeV	383 787	0.1967 ± 0.0003

Table 10. $Z \to ee$ selection acceptance from PYTHIA Monte Carlo simulation. Statistical uncertainties are shown.

Selection criteria	Number of events	Net acceptance
Total events	507 500	–
$\lvert z_{\rm vtx}\rvert < 60$ cm	490 756	–
66 GeV/$c^2 < M_{ee}$(Gen) < 116 GeV/c^2	376 523	–
Central EM cluster	363 994	0.9667 ± 0.0003
Calorimeter fiducial cuts	299 530	0.7955 ± 0.0007
Electron track $p_T > 10$ GeV/c	252 881	0.6716 ± 0.0008
EM cluster $E_T > 25$ GeV	186 318	0.4948 ± 0.0008
Second EM cluster (central or plug)	176 417	0.4685 ± 0.0008
Second cluster calorimeter fiducial cuts	146 150	0.3882 ± 0.0008
Second electron track $p_T > 10$ GeV/c (central)	138 830	0.3687 ± 0.0008
Second EM cluster $E_T > 25$ GeV (central), 20 GeV (plug)	125 074	0.3322 ± 0.0008
Second EM cluster $E_{\rm had}/E_{\rm em} < 0.125$ (Plug)	124 881	0.3317 ± 0.0008
66 GeV/$c^2 < M_{ee}$(Rec) < 116 GeV/c^2	120 575	0.3202 ± 0.0008
Opposite charge (central–central)	119 925	0.3185 ± 0.0008

our acceptances. The $W \to \ell\nu$ acceptance calculations are outlined in tables 8 and 9 for the electron and muon candidate samples. The geometric and kinematic requirements listed in each table define the acceptances for the corresponding samples. The number of simulated events which satisfy each of the successive, cumulative criteria is shown in the tables along with the resulting net acceptances based on the total number of events with primary vertices inside our allowed region. The $W \to \mu\nu$ events which contain reconstructed muons with stubs in the CMX region of the muon detector are assigned a weight of 55.5/72.0 in the numerator of the acceptance calculation to account for the fact that the CMX detector was offline during the first 16.5 pb^{-1} of integrated luminosity that define our samples. The largest uncertainties attached to the individual luminosity measurements (see section 3.2) cancel in our weighting ratio for CMX events and the residual uncertainty on this ratio has a negligible effect on the overall acceptance uncertainty.

The $Z \to \ell\ell$ acceptance calculations are outlined in tables 10 and 11 for the corresponding electron and muon candidate samples. As previously stated in section 5.1, the acceptances that we define for these samples are for $\gamma^*/Z \to \ell\ell$ in the invariant mass range 66 GeV/$c^2 < M_{\ell\ell} <$ 116 GeV/c^2. The simulated event samples used to estimate the Z boson acceptances are generated with a looser invariant mass requirement, $M_{\ell\ell} > 30$ GeV/c^2. Generated events with an invariant mass outside our allowed range do not contribute to the denominator of these acceptance calculations but can contribute to the numerator if the final reconstructed invariant mass turns out to lie within our allowed region due to radiative and/or detector resolution

Table 11. $Z \to \mu\mu$ selection acceptance from PYTHIA Monte Carlo simulation. Statistical uncertainties are shown.

Selection criteria	Number of events	Net acceptance
Total events	507 500	–
$\lvert z_{\text{vtx}}\rvert < 60$ cm	490 755	–
$66\ \text{GeV}/c^2 < M_{\mu\mu}(\text{Gen}) < 116\ \text{GeV}/c^2$	375 981	–
CMUP or CMX muon	217 041	0.5773 ± 0.0008
Muon chamber fiducial cuts	209 693	0.5577 ± 0.0008
Muon track fiducial cuts	199 940	0.5318 ± 0.0008
Muon track $p_T > 20\ \text{GeV}/c$	157 244	0.4182 ± 0.0008
Second track with $p_T > 10\ \text{GeV}/c$	91 048	0.2422 ± 0.0007
Second track fiducial cuts	62 663	0.1667 ± 0.0006
Second track $p_T > 20\ \text{GeV}/c$	56 459	0.1502 ± 0.0006
$66\ \text{GeV}/c^2 < M_{\mu\mu}(\text{rec}) < 116\ \text{GeV}/c^2$	52 160	0.1387 ± 0.0006

effects. In order for an event to contribute to the denominator of the Z boson acceptance calculations, we require that the invariant mass of the dilepton pair at the generator level before application of any final state radiative effects lies within the correct invariant mass range, $66\ \text{GeV}/c^2 < M_{\ell\ell}(\text{Gen}) < 116\ \text{GeV}/c^2$. As in the case of the $W \to \mu\nu$ acceptance calculation, events in the numerator of the $Z \to \mu\mu$ acceptance calculation must be weighted to account for the fact that the CMX portion of the muon detector was offline for the first subset of integrated luminosity that defines our samples. In order to account for this effect, a weight of (55.5/72.0) is applied to events contributing to the numerator of the $Z \to \mu\mu$ acceptance calculation which contain a CMX muon candidate satisfying the three muon geometric and kinematic requirements listed in table 11 and no CMUP muon candidates satisfying these same three requirements.

5.4. Improved acceptance calculations

The tuned PYTHIA simulated event samples are designed to provide the best possible model for our W and Z boson candidate samples. However, the actual boson production cross-section calculation made by PYTHIA is done only at leading order (LO); see figure 1. The complex topologies of higher order contributions are modeled using a backward shower evolution algorithm which includes initial-state radiative effects and a separate, post-generation algorithm for including final-state radiation. A better description of boson production can be obtained from recently developed NNLO theoretical calculations of the double-differential production cross sections, $\mathrm{d}^2\sigma/\mathrm{d}y\,\mathrm{d}M$, as a function of boson rapidity (y) and mass (M), for both $W^{\pm}$ and Drell–Yan production [17]. The calculations are based on the MRST 2001 NNLL PDF set [66] and electroweak parameters taken from [20]. The single differential cross sections, $\mathrm{d}\sigma/\mathrm{d}y$, are obtained by integrating over the mass range, $66\ \text{GeV}/c^2 < M_{\ell\ell} < 116\,\text{GeV}/c^2$ for Drell–Yan production and $40\,\text{GeV}/c^2 < M_{\ell\nu} < 240\,\text{GeV}/c^2$ for $W^{\pm}$ production.

We use these NNLO theoretical calculations of $\mathrm{d}\sigma/\mathrm{d}y$ for Drell–Yan and $W^{\pm}$ production to obtain improved acceptance estimates for our candidate samples. First, the tuned PYTHIA event simulation is used to create acceptance functions for each candidate sample as a function of boson rapidity, $A(y)$. These functions provide the acceptance in each boson rapidity bin based on our modeling of the CDF detector contained in the event simulation. Figure 14 shows the $A(y)$ acceptance functions for each of our four candidate samples. The $Z \to ee$ sample has larger acceptance at higher boson rapidity due to the plug calorimeter modules which provide additional coverage in the forward part of the detector for the second electron in these events. Based on these distributions, the acceptance of each sample, $\overline{A}$, is then calculated as

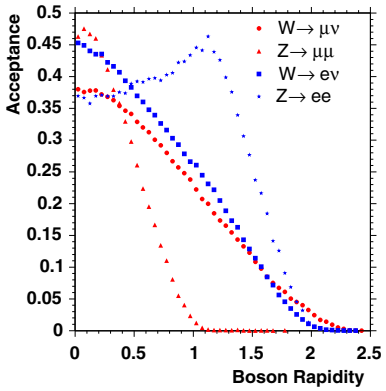

Figure 14. Acceptance as a function of boson rapidity, $A(y)$, for our four candidate samples: $W \to e\nu$ (squares), $W \to \mu\nu$ (points), $Z \to ee$ (stars) and $Z \to \mu\mu$ (triangles).

Table 12. Central acceptance values for our candidate samples based on $\mathrm{d}\sigma/\mathrm{d}y$ distributions obtained from both NNLO and PYTHIA simulation.

Acceptance	NNLO calculations	PYTHIA	Difference (%)
$A_{W\to\mu\nu}$	0.1970	0.1967	+0.15
$A_{W\to e\nu}$	0.2397	0.2395	+0.08
$A_{Z\to\mu\mu}$	0.1392	0.1387	+0.36
$A_{Z\to ee}$	0.3182	0.3185	−0.09
$A_{Z\to\mu\mu}/A_{W\to\mu\nu}$	0.7066	0.7054	+0.17
$A_{Z\to ee}/A_{W\to e\nu}$	1.3272	1.3299	−0.20

$$\overline{A} = \frac{\int \frac{\mathrm{d}\sigma}{\mathrm{d}y} \cdot A(y) \cdot \mathrm{d}y}{\int \frac{\mathrm{d}\sigma}{\mathrm{d}y} \cdot \mathrm{d}y}. \tag{11}$$

The acceptance values obtained with this approach are shown in table 12 and compared with values obtained directly from the PYTHIA simulated event samples. The results all agree within 0.4% indicating that the shapes of the NNLO $\mathrm{d}\sigma/\mathrm{d}y$ distributions are very similar to those computed with the PYTHIA simulation. The acceptance values obtained using the NNLO theoretical differential cross-section calculations are used for our measurements.

5.5. Uncertainties in NNLO calculation

Uncertainties in the NNLO calculations of the differential boson production cross sections lead to uncertainty on our calculated acceptance values. The theoretical calculations require a large number of input parameters taken from world average experimental results that have their own associated uncertainties. The renormalization scale used in the calculations is another source of uncertainty. The default renormalization scales used in the calculations are M_Z for Drell–Yan production and M_W for $W^{\pm}$ production. To study the effect of this scale on our central acceptance values, we recalculate the $\mathrm{d}\sigma/\mathrm{d}y$ production cross sections using renormalization scales twice and one-half of the default values. For both cases, we find the net change in our calculated acceptances to be less than 0.1% which has a negligible effect on our overall acceptance uncertainty.

Table 13. Comparison of acceptances for our candidate samples based on $\mathrm{d}\sigma/\mathrm{d}y$ distributions from the NNLO and NLO versions of our default theoretical calculation. The difference is taken as an uncertainty on higher order contributions.

Acceptance	NNLO	NLO	Difference (%)
$A_{W\to\mu\nu}$	0.1970	0.1975	0.25
$A_{W\to e\nu}$	0.2397	0.2404	0.29
$A_{Z\to\mu\mu}$	0.1392	0.1402	0.72
$A_{Z\to ee}$	0.3182	0.3184	0.06
$A_{Z\to\mu\mu}/A_{W\to\mu\nu}$	0.7066	0.7101	0.50
$A_{Z\to ee}/A_{W\to e\nu}$	1.3272	1.3246	0.20

We perform a computational consistency check on the NLO component of the NNLO $\mathrm{d}\sigma/\mathrm{d}y$ calculation [17] with a different $\overline{MS}$ NLO computation of $\mathrm{d}\sigma/\mathrm{d}y$ [11–13, 15]. We find that the resulting acceptance values differ by no more than 0.1%. Based on this agreement between the two calculations, we assign no additional uncertainty to our acceptance values based on the calculation itself. However, our default calculation is still susceptible to uncertainties from higher order effects beyond NNLO. To place a conservative limit on the magnitude of higher order uncertainties, we compare acceptance values based on the NLO and NNLO versions of our default $\mathrm{d}\sigma/\mathrm{d}y$ production cross-section calculations and assign an uncertainty based on the differences. The results are shown in table 13. The largest difference is seen in the acceptance for the $Z \to \mu\mu$ candidate sample, which has the narrowest acceptance window in boson rapidity.

5.6. Uncertainties from PDF model

The largest uncertainties on our acceptance values arise from uncertainties on the momentum distributions of quarks and gluons inside the proton modeled in the PDF sets used as inputs to our theoretical calculations. The choice of PDF input has a significant effect on the shape of the $\mathrm{d}\sigma/\mathrm{d}y$ distributions, and consequently a significant effect on the calculated acceptances for our candidate samples. As noted earlier, our theoretical calculations use the best-fit MRST 2001 NNLL PDF set [66]. The input PDF sets are created by fitting relevant experimental results to constrain the parameters which describe the quark/gluon momentum distributions in the proton. Currently, the NNLL PDF set provided by the MRST group is the only one available to us. NLL PDF sets are available from both groups (MRST01E [66, 67] and CTEQ6.1 [68]), however. To investigate differences between the CTEQ and MRST PDF sets, we calculate $\mathrm{d}\sigma/\mathrm{d}y$ at NLO using each group's NLL PDF set and check for differences in the acceptance values for our candidate samples based on each calculation. The results are shown in table 14. The differences are significant, especially for the $Z \to \mu\mu$ candidate sample.

Another recent development from the CTEQ and MRST groups is the release of 'error' PDF sets at NLL which map out the space of potential PDF parameter values based on the uncertainties of the experimental results used to constrain them. The CTEQ PDF parameterization is based on 20 parameters, P_i, which are tuned to their most likely values based on a minimization of the χ^2 of a global fit to the experimental data. The equivalent MRST parameterization uses only 15 parameters. As the covariance matrix of the P_i is not diagonal at the minimum, it is difficult to propagate fit errors on the P_i directly into uncertainties on experimentally measured quantities such as acceptances. However, both groups construct different sets of eigenvectors, Q_i, which do diagonalize the covariance matrix of the fit in the vicinity of the minimum. The Q_i are linearly independent by design, which allows

Table 14. Comparison of acceptances for our candidate samples based on $d\sigma/dy$ distributions from NLO theoretical calculations using NLL MRST and CTEQ PDF sets.

Acceptance	MRST	CTEQ	Difference (%)
$A_{W\to\mu\nu}$	0.1976	0.1960	0.82
$A_{W\to e\nu}$	0.2405	0.2385	0.84
$A_{Z\to\mu\mu}$	0.1401	0.1376	1.82
$A_{Z\to ee}$	0.3183	0.3164	0.60
$A_{Z\to\mu\mu}/A_{W\to\mu\nu}$	0.7088	0.7021	0.95
$A_{Z\to ee}/A_{W\to e\nu}$	1.3235	1.3264	0.22

Table 15. Contributions to the positive and negative acceptance uncertainties based on acceptance differences between the 'up' and 'down' error PDF sets associated with a given Q_i and the best-fit PDF set.

Direction of acceptance shifts	+Uncertainty	−Uncertainty
$\Delta A^i_\uparrow > 0$ and $\Delta A^i_\downarrow > 0$	$\sqrt{(\Delta A^{i\,2}_\uparrow + \Delta A^{i\,2}_\downarrow)/2}$	0
$\Delta A^i_\uparrow > 0$ and $\Delta A^i_\downarrow < 0$	$\Delta A^i_\uparrow$	$\Delta A^i_\downarrow$
$\Delta A^i_\uparrow < 0$ and $\Delta A^i_\downarrow > 0$	$\Delta A^i_\downarrow$	$\Delta A^i_\uparrow$
$\Delta A^i_\uparrow < 0$ and $\Delta A^i_\downarrow < 0$	0	$\sqrt{(\Delta A^{i\,2}_\uparrow + \Delta A^{i\,2}_\downarrow)/2}$

experimental uncertainties based on deviations in each parameter to be added in quadrature. The MRST and CTEQ groups transform individual $\pm1\sigma$ variations of each Q_i back into the P_i parameter space and generate sets of 'up' and 'down' error PDFs. This procedure outputs two PDF sets per parameter for a total of 40 CTEQ (30 MRST) error PDF sets. The $\pm1\sigma$ variations of each eigenvector for the MRST01E and CTEQ6.1 error PDFs are different. These variations are based on the following values for the global fit χ^2 from its minimum: $\Delta\chi^2 = 50$ for MRST01E and $\Delta\chi^2 = 100$ for CTEQ6.1.

To determine the uncertainty on the acceptance values for our candidate samples based on the CTEQ and MRST error PDF sets, we perform the NLO $d\sigma/dy$ production cross-section calculations for each error PDF set and check how much the acceptance values based on each calculation deviate from the values obtained using the best-fit NLL PDF set. The uncertainty associated with each Q_i is determined from the changes in acceptance between the best-fit PDF set and both the 'up' and 'down' error PDF sets associated with the given parameter, $\Delta A^i_\uparrow$ and $\Delta A^i_\downarrow$. In most cases the two acceptance differences lie in opposite directions and can be treated independently, but in a small number of cases both differences lie in the same direction and a different procedure needs to be followed. Table 15 defines both the positive and negative uncertainties assigned to the acceptance uncertainty for each Q_i based on the relative signs of $\Delta A^i_\uparrow$ and $\Delta A^i_\downarrow$.

The positive and negative uncertainties associated with each of the individual Q_i (20 CTEQ and 15 MRST) are summed in quadrature to determine the overall PDF model uncertainty on our acceptance values. The results of these calculations using both the CTEQ and MRST error PDF sets are shown in table 16. We note that the MRST uncertainties are a factor of 2–3 lower than the CTEQ uncertainties which is most likely related to different choices for the $\Delta\chi^2$ values used by the two groups to choose the $\pm1\sigma$ points associated with each of the Q_i. We choose to use the larger CTEQ uncertainties based on the fact that the magnitude of those uncertainties is more consistent with the differences observed between the

Table 16. PDF model acceptance uncertainties based on the CTEQ and MRST error PDF sets.

Acceptance	CTEQ +Uncertainty (%)	CTEQ −Uncertainty (%)	MRST +Uncertainty (%)	MRST −Uncertainty (%)
$A_{W\to\mu\nu}$	1.13	1.47	0.46	0.57
$A_{W\to e\nu}$	1.16	1.50	0.48	0.58
$A_{Z\to\mu\mu}$	1.72	2.26	0.67	0.87
$A_{Z\to ee}$	0.69	0.84	0.27	0.33
$A_{Z\to\mu\mu}/A_{W\to\mu\nu}$	0.67	0.86	0.26	0.31
$A_{Z\to ee}/A_{W\to e\nu}$	0.74	0.56	0.29	0.23

Table 17. Additional PDF model acceptance uncertainties based on the CTEQ and MRST error PDF sets.

Acceptance	CTEQ +Uncertainty (%)	CTEQ −Uncertainty (%)	MRST +Uncertainty (%)	MRST −Uncertainty (%)
$\sigma_W \cdot A_{W\to\mu\nu}/\sigma_Z \cdot A_{Z\to\mu\mu}$	1.03	1.06	0.52	0.42
$\sigma_W \cdot A_{W\to e\nu}/\sigma_Z \cdot A_{Z\to ee}$	0.70	1.06	0.42	0.62
$A_{W\to e\nu}/A_{W\to\mu\nu}$	0.03	0.04	0.01	0.01

acceptance values for our samples calculated with the best-fit NLL CTEQ and MRST PDF sets (see table 14). Based on the technique outlined above, we also determine the PDF model uncertainties associated with three additional quantities useful in the calculation of $\Gamma(W)$ and g_μ/g_e detailed in section 8. These values are given in table 17.

5.7. Uncertainties from boson p_T model

As discussed in section 5.2, the boson p_T distributions in our PYTHIA simulated event samples are tuned based on the CDF Run I measurement of the $d\sigma/dp_T$ spectrum of electron pairs in the mass region between 66 GeV/c^2 and 116 GeV/c^2 (see section 5.2). The simulated γ^*/Zp_T distribution at $\sqrt{s} = 1.8$ TeV after tuning is shown in figure 12 along with the measured distribution from Run I. The values for the four parameters we use in PYTHIA for this tuning are chosen using a χ^2 comparison of the Z boson p_T spectrum measured in Run I and the PYTHIA generated spectra obtained while varying the values of our tuning parameters.

The acceptance uncertainties related to our boson p_T model come primarily from the Run I measurement uncertainties. We quantify the effect of these uncertainties on our measured acceptances using the uncertainties returned from the χ^2 fits used to obtain the four PYTHIA tuning parameters. We choose to use conservative $\pm 3\sigma$ fit errors since the fit values for each of the tuning parameters, PARP(64) in particular, are somewhat inconsistent with expectation. We study the effects of changes in the boson p_T distributions on our measured acceptances by re-weighting events in the default simulated event samples based on differences between the default boson p_T distribution and those obtained from $\pm 3\sigma$ changes in our individual tuning parameters. Table 18 summarizes the best fit values and $\pm 3\sigma$ variations obtained for each tuning parameter and the corresponding acceptance uncertainties for each candidate sample. Changes to the PARP(93) tuning parameter were found to have a negligible effect on the boson p_T spectrum and the measured acceptances. Uncertainties associated with the other

Table 18. Fit results for PYTHIA boson p_T tuning parameters and corresponding uncertainties on the measured acceptances of our candidate samples.

Parameter	Best Fit	$\pm 3\sigma$ Variation	$\Delta A_{W\to\mu\nu}$ (%)	$\Delta A_{W\to e\nu}$ (%)	$\Delta A_{Z\to\mu\mu}$ (%)	$\Delta A_{Z\to ee}$ (%)
PARP(62)	1.26	0.30	0.01	0.00	0.01	0.01
PARP(64)	0.2	0.03	0.03	0.04	0.08	0.06
PARP(91)	2.0	0.3	0.02	0.02	0.00	0.02
PARP(93)	14	3	–	–	–	–
Combined			0.04	0.04	0.08	0.06

three tuning parameters are taken in quadrature to determine an overall acceptance uncertainty associated with the boson p_T model.

5.8. Uncertainties from recoil energy model

An accurate model of the event recoil energy in the simulation is important for estimating the acceptance of the event $\not\!\!E_T$ criteria applied to our $W \to \ell\nu$ candidate events. Simulated recoil energy distributions are dependent on the models for hadronic showering, the boson recoil energy and the underlying event energy. In addition, the simulation used in these measurements does not model other mechanisms that also contribute to the residual recoil energy in data events such as multiple interactions and accelerator backgrounds. To account for the effects of these differences, the simulated recoil energy distributions are tuned to match those in the data.

As discussed in section 5.3, the event recoil energy is defined as the total energy observed in the calorimeter after removing the energy deposits associated with the high p_T leptons in our $W \to \ell\nu$ and $Z \to \ell\ell$ candidates. To tune the simulated recoil energy distributions, we separate the observed recoil E_T in each event into components that are parallel and perpendicular to the transverse direction of the highest p_T lepton in the event. The two components, $U_{\parallel}^{\mathrm{recl}}$ and $U_{\perp}^{\mathrm{recl}}$, are each assigned energy shift (C) and scale (K) corrections in the form

$$\left(U_{\parallel}^{\mathrm{recl}}\right)' = \left(K_{\parallel} \times U_{\parallel}^{\mathrm{recl}}\right) + C_{\parallel}, \tag{12}$$

$$\left(U_{\perp}^{\mathrm{recl}}\right)' = \left(K_{\perp} \times U_{\perp}^{\mathrm{recl}}\right) + C_{\perp}. \tag{13}$$

The scale corrections are used to account for problems in the calorimeter response model and the effects of multiple interactions, the underlying event model, and accelerator backgrounds which are in principle independent of the lepton direction. The shift corrections are designed to account for simulation deficiencies that have a lepton-direction dependence such as the W boson recoil model and the model for lepton energy deposition in the calorimeter. Based on the nature of these effects, we expect that the scaling corrections in both directions, $K_{\parallel}$ and $K_{\perp}$, should be equivalent and that the shift correction in the perpendicular direction, $C_{\perp}$, should be zero. We check these assumptions, however, by keeping each parameter independent in the fitting procedure used to determine the best values for tuning the recoil energy in simulated events.

To determine the best values for these scaling and shifting constants, we perform χ^2 fits between the data recoil energy distributions and corrected distributions from the simulation based on a range of scaling and shifting constants. An iterative process is used in which we

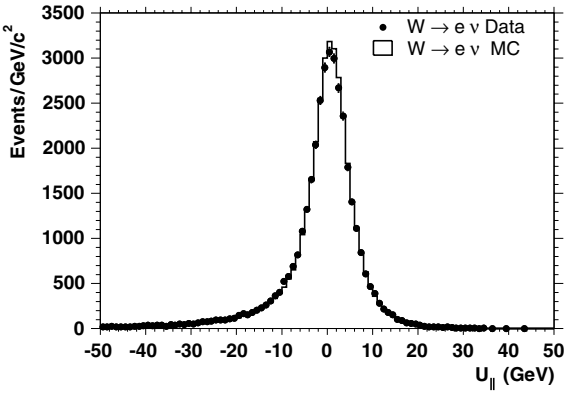

Figure 15. Comparison of $U_{\parallel}^{\text{recl}}$ recoil energy distributions for $W \to e\nu$ candidate events in tuned simulation and data.

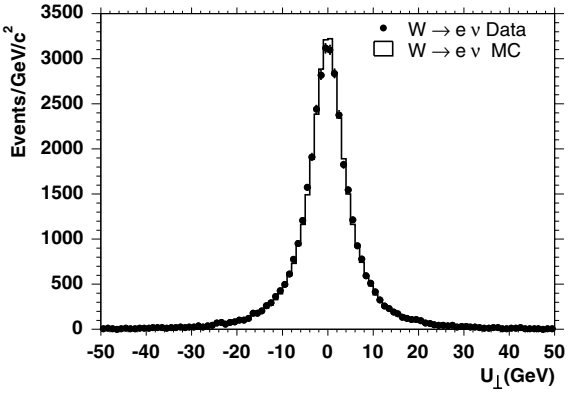

Figure 16. Comparison of $U_{\perp}^{\text{recl}}$ recoil energy distributions for $W \to e\nu$ candidate events in tuned simulation and data.

first determine the best possible shifting constants and then fit for scaling constants based on those values. We repeat this process until the χ^2 fits for both the scaling and shifting constants stabilize at set values. No effects are expected which can give rise to shifts in the energy perpendicular to the lepton momentum and the fitted shifts of these distributions are consistent with zero. We set $C_{\perp}$ to zero. We also find that the fitted scale factors for both recoil energy components agree well with each other in both the electron and muon candidate samples. Based on this agreement, we also make a combined fit to both components for a single correction scale factor. We use this single-scaling factor to correct both recoil energy components. A comparison of the $U_{\parallel}^{\text{recl}}$ and $U_{\perp}^{\text{recl}}$ distributions for $W \to e\nu$ candidate events in tuned simulation and data are shown in figures 15 and 16.

The uncertainties on our measured acceptances related to the recoil energy model in the simulation are estimated using the $\pm 3\sigma$ values of the scale and shift correction factors returned from our fit procedure. As in the case of boson p_T model uncertainties, we choose to use the $\pm 3\sigma$ values rather than the $\pm 1\sigma$ values as we are using these parameters to cover a wide range of effects that are potentially incorrectly modeled in our simulated event samples. Since

Table 19. Summary of simulation recoil energy tuning parameter values and uncertainties obtained from our fit procedure and the corresponding uncertainties on our measured acceptance values.

Tuning parameter	$W \to e\nu$ Fit value	$W \to e\nu$ $\pm 3\sigma$ variation	$W \to \mu\nu$ Fit value	$W \to \mu\nu$ $\pm 3\sigma$ variation	$\Delta A_{W\to e\nu}$ (%)	$\Delta A_{W\to \mu\nu}$ (%)
$K_\parallel$	1.06	0.02	1.06	0.03	–	–
$K_\perp$	1.04	0.02	1.05	0.02	–	–
K	1.05	0.02	1.05	0.02	0.17	0.20
$C_\parallel$	−0.4	0.1	−0.1	0.1	0.18	0.29
$C_\perp$	0.0	0.1	0.0	0.1	0.00	0.00
Combined					0.25	0.35

the tuning parameters are not directly related to the underlying mechanisms that affect the recoil energy distributions, we choose to be conservative in how we estimate the associated acceptance uncertainties via this procedure. We recalculate the acceptance of our candidate samples with each of the individual tuning parameters changed to its $\pm 3\sigma$ values and assign an uncertainty based on the differences between these results and our default acceptance values. The changes in acceptance found from modifying the overall scale correction K and the shift corrections for both directions, $C_\parallel$ and $C_\perp$, are added in quadrature to estimate the total uncertainties on our measured acceptances due to the recoil energy model in the simulation. To be conservative we choose to include an uncertainty based on fit results for $C_\perp$ even though this parameter is set to zero for tuning the simulated recoil energy distributions.

Table 19 summarizes the best fit values and $\pm 3\sigma$ variations with respect to the best fit values obtained for each of the scaling and shifting parameters used to tune the recoil energy model in simulation and the corresponding acceptance uncertainties for the $W \to \ell\nu$ candidate samples.

5.9. Uncertainties from energy and momentum scale/resolution

The modeling of COT track p_T scale and resolution in the simulation affects our acceptance estimates for the minimum track p_T requirements made on muon and electron candidates in our samples. Similarly, the model of cluster E_T scale and resolution for the electromagnetic sections of the calorimeter can change the acceptance estimates for the minimum cluster E_T requirements on electrons. Lepton energy and momentum measurements can also alter the event $\not\!\!E_T$ calculation, and incorrect modeling of these quantities can therefore also affect our acceptance estimates for the minimum $\not\!\!E_T$ criteria applied to our $W \to \ell\nu$ samples.

We check the scale and resolution of the track p_T and cluster E_T measurements in the simulation using the invariant mass distributions of $\gamma^*/Z \to \mu\mu$ and $\gamma^*/Z \to ee$ candidate events. A direct comparison of these distributions in data and simulation is possible due to the small level of background contamination in these samples. We first define scale factors for COT track p_T (K_{p_T}) and cluster E_T (K_{E_T}) in the simulation via the expressions

$$p'_T = K_{p_T} \times p_T, \tag{14}$$

$$E'_T = K_{E_T} \times E_T. \tag{15}$$

The best values for these scale factors are determined by making a series of χ^2 fits between the $\gamma^*/Z \to \ell\ell$ invariant mass distributions in data and tuned simulation based on a range of values for the scale factors. The best χ^2 fit for the track p_T scale factor is $K_{p_T} = 0.997$.

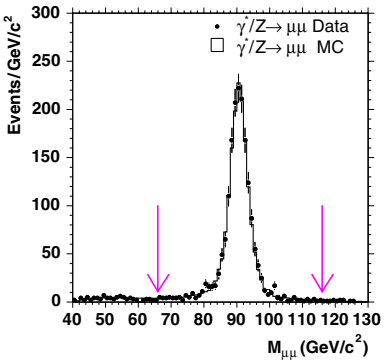

Figure 17. $\gamma^*/Z \to \mu\mu$ invariant mass distribution in data and tuned simulation normalized to the data. The arrows indicate the invariant mass range of our γ^*/Z cross-section measurement.

Since the mean of the $\gamma^*/Z \to \mu\mu$ invariant mass peak in the simulation is centered on the measured Z boson mass, the best fit value for K_{p_T} is indicative of the fact that the current p_T scale for reconstructed tracks in the data is low. This result is consistent with track p_T scaling factors for simulation obtained from similar fits to the $J/\Psi \to \mu\mu$ and $\Upsilon \to \mu\mu$ invariant mass peaks indicating that the resulting scale factor is not p_T dependent. The best fits for the cluster E_T scale factors in the central and plug calorimeter modules are $K_{E_T}(\text{central}) = 1.000$ and $K_{E_T}(\text{plug}) = 1.025$ indicative of a model that underestimates energy deposition in the plug modules but is accurate for the central module.

Comparisons of the $\gamma^*/Z \to \ell\ell$ invariant mass distributions in the data and the simulation are used to tune the track p_T and cluster E_T resolution in the simulation. We smear these values in simulated events by generating a random number from a Gaussian distribution with mean equal to 1 and width equal to a chosen σ for each lepton candidate in our samples. The resolution smearing is obtained by multiplying the track p_T and/or cluster E_T by the different random numbers obtained from our distribution. Setting σ equal to 0 adds no smearing since each generated random number equals one by definition. The best values for σ are obtained from χ^2 fits between the $\gamma^*/Z \to \ell\ell$ invariant mass distributions in data and tuned simulation corresponding to a range of values for σ. The best χ^2 fits for track p_T and central calorimeter E_T resolution are found to be for the case of σ equal to 0 indicating that these resolutions are well modeled in the simulation. The best χ^2 fit for plug calorimeter E_T resolution is for a value of σ above zero indicating that the simulation model for E_T resolution in the plug modules needs to be degraded to match the data better. Figures 17 and 18 show comparisons between the $\gamma^*/Z \to \mu\mu$ and $\gamma^*/Z \to ee$ invariant mass distributions in data and tuned simulation.

The effects of uncertainties in the simulation model for the scale and resolution of track p_T and cluster E_T on our measured acceptances are estimated based on the $\pm 3\sigma$ values of the corresponding tuning parameters obtained from our fit procedure. Our choice of using the $\pm 3\sigma$ values to estimate acceptance uncertainties is conservatively based on the idea that these tuning parameters are not directly related to the underlying mechanisms that set the scale and resolution of track p_T and cluster E_T in the detector. The acceptance uncertainties are estimated by observing the changes in measured acceptance for each candidate sample that occur when each individual tuning parameter is changed between its default and $\pm 3\sigma$ values. A summary of the fitted values and uncertainties of the scale and resolution tuning parameters

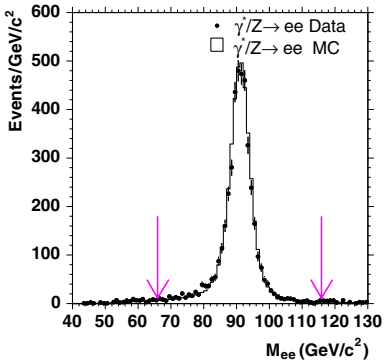

Figure 18. $\gamma^*/Z \to ee$ invariant mass distribution in data and tuned simulation normalized to the data. The arrows indicate the invariant mass range of our γ^*/Z cross-section measurement.

Table 20. Summary of simulation track p_T scale and resolution tuning parameters and corresponding uncertainties on our measured acceptance values.

Tuning parameter	$Z \to \mu\mu$ Fit value	$Z \to \mu\mu$ $\pm 3\sigma$ variation	$Z \to ee$ Fit value	$Z \to ee$ $\pm 3\sigma$ variation	$\Delta A_{W\to ev}$ (%)	$\Delta A_{W\to \mu v}$ (%)	$\Delta A_{Z\to ee}$ (%)	$\Delta A_{Z\to \mu\mu}$ (%)
K_{p_T}	0.997	0.003	–	–	0.03	0.21	0.04	0.05
σ_{p_T}	1.000	0.003	–	–	0.00	0.00	0.00	0.00
K_{E_T} (central)	–	–	1.000	0.003	0.34	0.00	0.23	0.00
σ_{E_T} (central)	–	–	1.000	0.015	0.03	0.00	0.05	0.00
K_{E_T} (plug)	–	–	1.025	0.006	0.00	0.00	0.11	0.00
σ_{E_T} (plug)	–	–	1.027	0.011	0.00	0.00	0.05	0.00

for track p_T and cluster E_T is given in table 20 along with the estimated uncertainties on the measured acceptances of our candidate samples associated with each parameter.

5.10. Uncertainties from detector material model

The acceptances of the kinematic selection criteria applied to electron candidates are dependent on the amount of material in the detector tracking volume since electrons can lose a significant fraction of their energy prior to entering the calorimeter via bremsstrahlung radiation originating from interactions with detector material.

The electron E/p distribution, because of its sensitivity to radiation, is used to compare the material description in the detector simulation in the central region with that of the real detector as observed in data. One measure of the amount of material that electrons pass through in the tracking region is the ratio of the number of events in the peak of the E/p distribution ($0.9 < E/p < 1.1$) to the number of events in the tail of the distribution ($1.5 < E/p < 2.0$). We study the uncertainty in the amount of material in the simulation by varying the thickness of a cylindrical layer of material in the detector simulation geometry description in the region between the silicon and COT tracking volumes. We choose to use copper as the material for this cylindrical layer as it best describes the silicon tracker copper readout cables and is also supported by independent studies of muon energy loss in the calorimeter. Based on electron candidates produced in decays of both W and Z bosons, we determine that the matching of the E/p distribution between data and simulation has an uncertainty corresponding to $\pm 1.5\%$

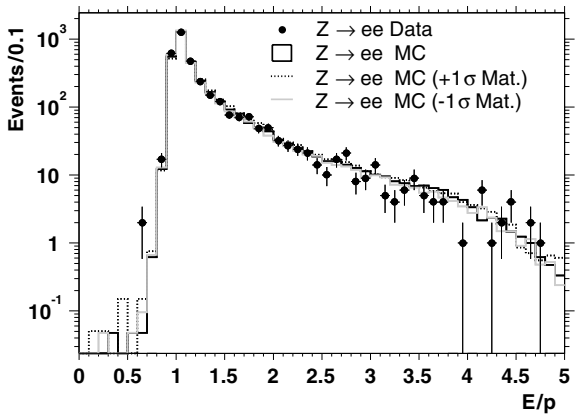

Figure 19. Comparison of E/p distribution for electron candidates in $Z \to ee$ events in data and simulation. The $\pm 1\sigma$ samples are simulated with $\pm 1.5\%$ of a radiation length of copper in the tracking volume.

of a radiation length (X_0) of copper. This variation in the thickness of the cylindrical layer is used to model the acceptance uncertainties originating from the model of the detector material in the simulation.

This result is cross-checked by counting the fraction of electrons in $W \to e\nu$ candidate events which form 'tridents' (see section 7). The probability of finding a trident, created when an electron radiates a photon which immediately converts into an electron-positron pair, is strongly dependent on the amount of material traversed by the electron inside the tracking volume. We also compare the resolution of the $Z \to ee$ invariant mass peak in data and simulation which is sensitive to the rate of radiative interactions within the tracking volume. The results of these studies are consistent with the E/p results.

Figure 19 shows the E/p distributions for electron candidates in our $Z \to ee$ data and simulated event samples. The $\pm 1\sigma$ material samples are simulated using $\pm 1.5\%$ of a radiation length of copper. We observe good agreement between data and our default simulation in the region below $E/p = 2.5$. In the high E/p tail above this value, the comparison is biased by dvips background events in the data.

The tracks associated with electron candidates in the calorimeter plug modules have a low reconstruction efficiency due to the limited number of tracking layers in the forward region. Therefore, the plug preradiator detector is used to study the detector material in the simulation for plug electron candidates. The amount of energy deposited in the plug preradiator depends on the shower evolution of the electron in front of the calorimeter which is itself dependent on the amount of material the electron passes through before entering the calorimeter. On average, electrons passing through more material inside the tracking volume will have more evolved showers at the inner edges of the calorimeter and therefore deposit more energy in the plug preradiator.

To study the detector simulation material description in the forward part of the tracking volume, we compare the ratio of energies observed in the plug preradiator and remaining plug calorimeter sections for forward electron candidates in data and simulation. As in the central region, we study the material in the simulation by varying the thickness of an iron disk in the volume between the tracking chamber endplate and the inner edge of the plug calorimeter. These studies indicate that our model for detector material in the forward region has an

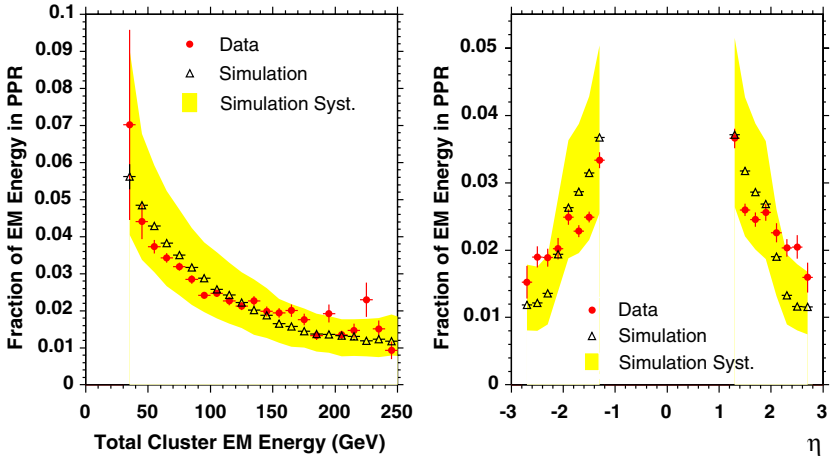

Figure 20. Comparison of observed ratio of energies in plug preradiator and plug electromagnetic calorimeter for electron candidates as a function of the combined energy (left) and pseudorapidity (right) of candidates. Data distributions are denoted by the filled circles. The open triangles and associated shaded band show the distribution and uncertainty range obtained from simulation when ±16.5% of a radiation length thick iron disk is used in the detector material description.

Table 21. Summary of acceptance uncertainties due to detector tracking volume material model in simulation.

Material model	$\Delta A_{W\to ev}$	$\Delta A_{Z\to ee}$
Central	0.73%	0.94%
Plug	–	0.21%

uncertainty corresponding to ±16.5% of a radiation length (X_0) in the iron disk. Figure 20 shows the ratio of energies observed in the plug preradiator (PPR) and the plug electromagnetic calorimeter (PEM) for electron candidates in data and simulation as a function of both the combined energy (PPR + PEM) and pseudorapidity of the candidates.

Acceptance uncertainties coming from the simulation material model are determined by generating simulated event samples with the thicknesses of the extra material layers set one at a time in the simulation to the lower and upper limits of their uncertainty ranges. The changes in measured acceptance for the $W \to ev$ and $\gamma^*/Z \to ee$ samples relative to the default simulation for the modified detector material models are summarized in table 21.

5.11. Acceptance uncertainty summary

The acceptance uncertainties on our event samples are summarized in table 22.

6. Efficiency

6.1. Introduction

The acceptance values estimated from our simulated samples are corrected for additional inefficiencies from event selection criteria that are either not modeled in the simulation or

Table 22. Summary of estimated uncertainties on the measured acceptances for our four candidate samples.

Uncertainty category	$\Delta A_{W\to e\nu}$ (%)	$\Delta A_{W\to \mu\nu}$ (%)	$\Delta A_{Z\to ee}$ (%)	$\Delta A_{Z\to \mu\mu}$ (%)
NNLO $\mathrm{d}\sigma/\mathrm{d}y$ calculation	0.29	0.25	0.06	0.72
PDF model (positive)	1.16	1.13	0.69	1.72
PDF model (negative)	1.50	1.47	0.84	2.26
Boson p_T model	0.04	0.04	0.06	0.08
Recoil energy model	0.25	0.35	0.00	0.00
Track p_T scale/resolution	0.03	0.21	0.04	0.05
Cluster E_T scale/resolution	0.34	0.00	0.26	0.00
Detector material model	0.73	0.00	0.96	0.00
Simulated event statistics	0.13	0.14	0.24	0.41
Total (positive)	1.46	1.22	1.23	1.94
Total (negative)	1.75	1.57	1.26	2.44

are better measured directly from data. We determine a combined efficiency, ϵ_{tot}, for each candidate sample based on measured efficiencies for the individual selection criteria. We account for correlations between different selection criteria by having a specific order in which individual efficiency measurements are made. The efficiency measurement for a given selection criterion is made using a subset of candidates that passes the full set of selection criteria ordered prior to the one being measured. In addition, since the efficiency is applied as a correction to the acceptance, candidates used to measure efficiencies are also required to meet the geometrical and kinematic requirements used to define these acceptances. The ordering and definitions of the individual selection criteria efficiencies are presented in this introductory section. The following two sections describe how these individual efficiencies are combined to obtain the total event efficiencies for our $W \to \ell\nu$ and $Z \to \ell\ell$ candidate samples. The remaining sections describe how each of the individual efficiency terms is measured.

The first efficiency term is ϵ_{vtx}, the fraction of $p\overline{p}$ collisions that occur within ± 60 cm of the center of the detector along the z-axis. We impose this requirement as a fiducial cut to ensure that $p\overline{p}$ interactions are well contained within the geometrical acceptance of the detector. The z-coordinate of the event vertex for a given event is taken from the closest intersection point of the reconstructed high p_T lepton track(s) with the z-axis. Since event selection criteria can bias our samples against events originating in the outer interaction region, the efficiency of our vertex position requirement, ϵ_{vtx}, is measured directly from the observed vertex distribution in minimum-bias events.

We define ϵ_{trk} as the efficiency for reconstructing the track of the high p_T lepton in the COT and ϵ_{rec} as the efficiency for matching the found track to either a reconstructed electromagnetic cluster in the calorimeter (electrons) or a reconstructed stub in the muon chambers (muons). The ϵ_{rec} term incorporates both the reconstruction efficiency for the cluster or stub and the matching efficiency for connecting the reconstructed cluster or stub with its associated COT track.

For reconstructed leptons (tracks matched to clusters or stubs), ϵ_{id} is the efficiency of the lepton identification criteria used to increase the purity of our lepton samples. To increase the number of events in our $Z \to \ell\ell$ candidate samples, we use a looser set of identification criteria on the second lepton leg in these events. The loose lepton selection criteria are a subset of the set of cuts applied to the single lepton in $W \to \ell\nu$ events and the first lepton leg in $Z \to \ell\ell$ events. The combined efficiency for the loose subset of cuts is referred to as ϵ_{lid},

and we define $\epsilon_{\rm tid}$ as the efficiency for the set of remaining identification cuts not included in the loose subset. The efficiency of our lepton isolation requirement, which helps to reduce non-W/Z backgrounds in our samples, is defined independently as $\epsilon_{\rm iso}$. It is important to avoid double-counting correlated efficiency losses when measuring the efficiencies for our two sets of identification cuts and the isolation requirement. We eliminate this problem by defining a specific ordering of these terms ($\epsilon_{\rm lid}$, $\epsilon_{\rm iso}$, $\epsilon_{\rm tid}$) and measuring each efficiency term using the subset of lepton candidates that meets the requirements associated with all of the efficiency terms ordered prior to that being measured. A natural consequence of using this procedure is that the total lepton identification efficiency, $\epsilon_{\rm id}$, is necessarily equal to the product of $\epsilon_{\rm lid}$ and $\epsilon_{\rm tid}$.

As discussed previously, the high p_T electron and muon data samples used to make the production cross-section measurements are collected with lepton-only triggers. We define $\epsilon_{\rm trg}$ as the efficiency for an isolated, high quality reconstructed lepton to have satisfied all of the requirements of the corresponding lepton-only trigger path. CDF has a three-level trigger system, and the value of $\epsilon_{\rm trg}$ is determined from the product of the efficiencies measured for each of the levels. The measured efficiency for a specific level of the trigger is based on the subset of reconstructed track candidates that satisfy the trigger requirements of the levels beneath it. This additional requirement is made to avoid double-counting correlated losses in efficiency observed in the different trigger levels.

Finally, there are two efficiencies that are applied only in measurements made in the muon-decay channels. We define $\epsilon_{\rm cos}$ as the efficiency for signal events not to be tagged as cosmic ray candidates via our tagging algorithm. The cosmic ray tagging algorithm is not based on the properties of a single muon, but rather on the full set of tracking data available from the COT in each event. As a result, $\epsilon_{\rm cos}$ is determined as an overall event efficiency rather than an additional lepton efficiency. Due to topological differences between $W \to \mu\nu$ and $Z \to \mu\mu$ events, the fraction of signal events tagged by the algorithm as cosmic rays is different for the two candidate samples. We refer to the efficiency term for the $W \to \mu\nu$ sample as $\epsilon^W_{\rm cos}$ and that for the $Z \to \mu\mu$ sample as $\epsilon^Z_{\rm cos}$. One additional event selection made only in the case of our $W \to \mu\nu$ candidate sample is the Z-rejection criteria. Due to the non-uniform coverage of the muon chambers, we find cases in which only one of the two high p_T muon tracks originating from a Z-boson decay has a matching stub in the muon detector. The additional selection criteria made to eliminate these events from our $W \to \mu\nu$ candidate sample has a corresponding efficiency defined as $\epsilon_{\rm z-rej}$.

6.2. $W \to \ell\nu$ efficiency calculation

The efficiency of detecting a $W \to \ell\nu$ decay that satisfies the kinematic and geometrical criteria of our samples is obtained from the formula shown in equation (16):

$$\epsilon_{\rm tot} = \epsilon_{\rm vtx} \times \epsilon_{\rm trk} \times \epsilon_{\rm rec} \times \epsilon_{\rm id} \times \epsilon_{\rm iso} \times \epsilon_{\rm trg} \times \epsilon_{\rm z-rej} \times \epsilon^W_{\rm cos}. \tag{16}$$

As described in detail above, the ordering of the cuts, as shown by their left to right order in the formula, is important. Each efficiency term is an efficiency for the subset of $W \to \ell\nu$ events that satisfies the kinematic and geometric criteria of our samples as well as the requirements associated with each of the efficiency terms to the left of the term under consideration. For example, the trigger efficiency term in the formula, $\epsilon_{\rm trg}$, is an efficiency for reconstructed leptons that satisfy the geometrical, kinematic, identification, and isolation criteria used to select the high p_T lepton in our $W \to \ell\nu$ candidate events. As noted previously, the $\epsilon_{\rm z-rej}$ and $\epsilon^W_{\rm cos}$ terms in the formula apply to the $W \to \mu\nu$ candidate sample only. Table 23 summarizes the measurements of the individual efficiency terms (described in detail below)

Table 23. Summary of the individual efficiency terms for $W \to \ell\nu$.

Selection criteria	Label	$W \to e\nu$	$W \to \mu\nu$
Fiducial vertex	ϵ_{vtx}	0.950 ± 0.004	0.950 ± 0.004
Track reconstruction	ϵ_{trk}	1.000 ± 0.004	1.000 ± 0.004
Lepton reconstruction	ϵ_{rec}	0.998 ± 0.004	0.954 ± 0.007
Lepton ID	ϵ_{id}	0.840 ± 0.007	0.893 ± 0.008
Lepton isolation	ϵ_{iso}	0.973 ± 0.003	0.982 ± 0.004
Trigger	ϵ_{trg}	0.966 ± 0.001	0.925 ± 0.011
Z-rejection cut	$\epsilon_{\text{z-rej}}$	–	0.996 ± 0.002
Cosmic ray tagging	$\epsilon_{\text{cos}}^{W}$	–	0.9999 ± 0.0001
Total	ϵ_{tot}	0.749 ± 0.009	0.732 ± 0.013

Table 24. Breakdown of loose and tight lepton identification efficiencies.

Selection criteria	Label	Central electron	Muon
Loose lepton ID	ϵ_{lid}	0.960 ± 0.004	0.933 ± 0.006
Tight lepton ID	ϵ_{tid}	0.876 ± 0.007	0.957 ± 0.005
All lepton ID	ϵ_{id}	0.840 ± 0.007	0.893 ± 0.008

and the resulting combined efficiencies for our $W \to \ell\nu$ candidate samples. The electron efficiencies shown in table 23 are for central calorimeter electrons only since our $W \to e\nu$ cross-section measurement is also restricted to candidates in this part of the detector.

6.3. $Z \to \ell\ell$ efficiency calculation

For both electrons and muons, we define a loose set of lepton selection criteria for the second leg of $Z \to \ell\ell$ events to increase the size of our candidate samples. The efficiency calculation for these samples is complicated by the fact that in many events both leptons from the Z boson decay can satisfy the tight lepton selection criteria which are required for only one of the two legs.

In the electron channel, we allow for two different types of loose lepton legs. The second leg can be either a central calorimeter electron candidate passing a looser set of selection criteria or an electron reconstructed in the forward part of the calorimeter (plug modules). For $Z \to \mu\mu$ candidates, a loose track leg is not required to have a matching reconstructed stub in the muon detectors. For this sample, the second muon leg is simply required to be a high p_T, isolated track satisfying the subset of muon identification cuts corresponding to the track itself. The breakdown of lepton identification cut efficiencies between the loose and tight criteria is shown in table 24 for both muons and central electrons. There is no reconstruction inefficiency associated with loose muon legs since track candidates are not required to have a matching muon detector stub.

Efficiencies for loose plug electrons are given in table 25. There is no track reconstruction component in the plug electron selection efficiency since a matched track is not required for candidates in the plug region of the calorimeter. Also, since no matching between tracks and clusters is done in this region, the plug lepton reconstruction efficiency is 100%. There are no dead calorimeter towers in the data-taking period used in these measurements. We also find that kinematic distributions for tight central electron legs in our central–plug $Z \to ee$ event sample are somewhat different from those in the central–central sample. These kinematic

Table 25. Plug electron efficiencies.

Selection criteria	Label	Plug electron
Lepton reconstruction	$\epsilon_{\rm rec}^{\rm plug}$	1.000
Lepton ID	$\epsilon_{\rm id}^{\rm plug}$	0.876 ± 0.015
Lepton isolation	$\epsilon_{\rm iso}^{\rm plug}$	0.993 ± 0.003
Central leg scale factor	$S_{\rm cl}^{\rm plug}$	1.014 ± 0.002
Total	$\epsilon_{\rm tot}^{\rm plug}$	0.883 ± 0.015

differences have a small effect on the electron identification efficiencies for the central legs in central–plug $Z \rightarrow ee$ events. In order to correct for this effect, we measure a central leg scale factor, $S_{\rm cl}^{\rm plug}$, which is the ratio of central leg efficiencies in central–plug $Z \rightarrow ee$ events to those in central–central events. The value of this scale factor given in table 25 is determined from simulation and is applied as an extra term in the overall selection efficiency for plug electrons.

To determine a total event selection efficiency for $Z \rightarrow ee$ events, we first calculate efficiencies for the central–central and central–plug samples which are independent of one another by definition. The total efficiency is a weighted sum of the efficiencies for the two samples. The weighting factors are determined from the relative numbers of central–central and central–plug events in our simulated sample. The fraction of central–plug events, $f_{\rm cp}$, is determined to be 0.655 ± 0.001. Equation (17) shows the efficiency calculation for central–central $Z \rightarrow ee$ events:

$$\epsilon_{\rm tot}^{\rm cc} = \epsilon_{\rm vtx} \times \epsilon_{\rm trk}^2 \times \epsilon_{\rm rec}^2 \times \epsilon_{\rm lid}^2 \times \epsilon_{\rm iso}^2 \times [\epsilon_{\rm tid} \times (2 - \epsilon_{\rm tid})] \times [\epsilon_{\rm trg} \times (2 - \epsilon_{\rm trg})]. \tag{17}$$

The squared terms in the formula apply to efficiency terms that are applied twice (we require two reconstructed central electrons passing loose identification and isolation criteria). In order for this treatment to be correct, the efficiencies of the two electron legs in the $Z \rightarrow ee$ candidates are required to be uncorrelated. Using our sample of simulated $Z \rightarrow ee$ events, we look for correlations between the efficiencies for the two electron legs and find them to be negligible. The tight identification and trigger criteria can be satisfied by either of the two electrons. The combined efficiency for one of two objects to satisfy a particular requirement can be written as $\epsilon^2 + 2 \times \epsilon \times (1 - \epsilon) = \epsilon \times (2 - \epsilon)$. The efficiency calculation for central–plug $Z \rightarrow ee$ events is given in equation (18).

$$\epsilon_{\rm tot}^{\rm cp} = \epsilon_{\rm vtx} \times \epsilon_{\rm trk} \times \epsilon_{\rm rec} \times \epsilon_{\rm lid} \times \epsilon_{\rm tid} \times \epsilon_{\rm iso} \times \epsilon_{\rm trg} \times \epsilon_{\rm rec}^{\rm plug} \times \epsilon_{\rm id}^{\rm plug} \times S_{\rm cl}^{\rm plug} \times \epsilon_{\rm iso}^{\rm plug}. \tag{18}$$

In these events only the central electron leg can satisfy the tight identification and trigger criteria so these efficiencies are only applied to the one central leg. Similarly, the plug efficiencies are applied only to the plug electron leg. Based on equations (17) and (18) the event efficiency for our combined $Z \rightarrow ee$ sample takes the form

$$\epsilon_{\rm tot}^{Z \rightarrow ee} = \epsilon_{\rm vtx} \times \epsilon_{\rm trk} \times \epsilon_{\rm rec} \times \epsilon_{\rm lid} \times \epsilon_{\rm tid} \times \epsilon_{\rm iso} \times \epsilon_{\rm trg} \times \big[(1 - f_{\rm cp}) \times \epsilon_{\rm trk} \times \epsilon_{\rm rec} \times \epsilon_{\rm lid} \times \epsilon_{\rm iso} \times (2 - \epsilon_{\rm tid}) \times (2 - \epsilon_{\rm trg}) + f_{\rm cp} \times \epsilon_{\rm rec}^{\rm plug} \times \epsilon_{\rm id}^{\rm plug} \times S_{\rm cl}^{\rm plug} \times \epsilon_{\rm iso}^{\rm plug}\big]. \tag{19}$$

The calculation of the total selection criteria efficiency for $Z \rightarrow \mu\mu$ candidate events is similar to that for events in the electron channel but involves some additional complications. As discussed above we increase our acceptance for $Z \rightarrow \mu\mu$ events by releasing the muon detector stub requirements for one of the two candidate track legs. The second muon leg in our candidate events can be any COT track passing the track quality, isolation and minimum ionizing calorimeter energy deposition criteria used in this analysis for selecting muon track

candidates. Since the track selection criteria are applied to both muon legs in our candidate events, the corresponding terms in the overall efficiency formula are squared. Only one of the two muon track candidates is required to have a matching stub in the muon detectors that satisfies our stub selection criteria. For roughly 40% of our candidate events, both of the muon track legs point to active regions of the muon detectors. In these cases, either of the two legs can have a matching stub in the muon detectors and satisfy the tight leg criteria. In other cases, one of the two legs will not point to an active detector region, and the stub-matching criteria must be satisfied by the one leg that is pointed at the muon detectors. In order to determine the total efficiency for $Z \to \mu\mu$ candidate events, we first determine the total selection efficiencies for both of these event classes. The event selection efficiency for the combined sample is then extracted as the weighted sum of the efficiencies for the two different event types.

The efficiency calculation for the subset of $Z \to \mu\mu$ events in which only one of the two muon tracks points to an active region of the muon detector is shown in equation (20). The efficiencies corresponding to selection criteria applied to both muon legs (track reconstruction, loose identification and isolation) enter into the formula as squared terms. The track leg pointing at the inactive regions of the muon detector can not have an associated reconstructed stub so the other track leg in the event must have a matching stub for the event to satisfy the $Z \to \mu\mu$ selection criteria. This leg must also satisfy the tight muon identification and event trigger requirements since an associated reconstructed muon detector stub is a necessary pre-condition for a muon leg to meet these criteria. Since the muon stub reconstruction, tight identification and trigger selection criteria can only be satisfied by one of the two muon legs in these events, the corresponding efficiency terms enter into equation (20) linearly. As previously mentioned, the efficiency for $Z \to \mu\mu$ events not to be tagged as cosmics, $\epsilon^{Z}_{\text{cos}}$, is independent of the measured value for $W \to \mu\nu$ events. As described subsequently, we measure this efficiency in $Z \to \mu\mu$ events to be $\epsilon^{Z}_{\text{cos}} = 0.9994 \pm 0.0006$:

$$\epsilon^{\mu\text{trk}}_{\text{tot}} = \epsilon_{\text{vtx}} \times \epsilon^{Z}_{\text{cos}} \times \epsilon^{2}_{\text{trk}} \times \epsilon^{2}_{\text{lid}} \times \epsilon^{2}_{\text{iso}} \times \epsilon_{\text{rec}} \times \epsilon_{\text{tid}} \times \epsilon_{\text{trg}}. \tag{20}$$

This situation is more complicated for the class of $Z \to \mu\mu$ events where both muon legs point to active regions of the muon detector. For these events both legs can individually satisfy the stub reconstruction, tight identification and trigger criteria of the sample. In order to simplify the efficiency calculation, we require that at least one of the two muon legs in each candidate event satisfies the requirements associated with all three of the above criteria. With this additional restriction, the overall event selection efficiency in the subset of $Z \to \mu\mu$ candidates where both muon legs point at active regions of the muon detector can be written as shown in equation (21). The combined efficiency for a muon leg to satisfy the stub reconstruction, tight identification and trigger criteria ($\epsilon^{*} = \epsilon_{\text{rec}} \times \epsilon_{\text{tid}} \times \epsilon_{\text{trg}}$) enters into equation (21) in the form $\epsilon^{*} \times (2 - \epsilon^{*})$ which, as described above, is the resulting efficiency for a set of criteria required for one of two identical objects within an event:

$$\epsilon^{\mu\mu}_{\text{tot}} = \epsilon_{\text{vtx}} \times \epsilon^{Z}_{\text{cos}} \times \epsilon^{2}_{\text{trk}} \times \epsilon^{2}_{\text{lid}} \times \epsilon^{2}_{\text{iso}} \times [\epsilon_{\text{rec}} \times \epsilon_{\text{tid}} \times \epsilon_{\text{trg}} \times (2 - \epsilon_{\text{rec}} \times \epsilon_{\text{tid}} \times \epsilon_{\text{trg}})]. \tag{21}$$

In order to combine equations (20) and (21) into a formula for the total event efficiency of our combined sample, we need to introduce an additional parameter, f_{dd}, which is defined as the fraction of $Z \to \mu\mu$ events within our geometric and kinematic acceptance in which both muon legs are found to point at active regions of the muon detector. This quantity is determined from the simulated event sample. For our candidate sample, we obtain $f_{\text{dd}} = 0.3889 \pm 0.0021$, which is a luminosity weighted average of the values for the different run periods in which the CMX was either offline or online. Using this additional factor, we determine a formula for the total event efficiency of our candidate sample by adding the expressions in equations (20) and (21) weighted by factors of $1 - f_{\text{dd}}$ and f_{dd} respectively. Finally, we obtain the expression shown in equation (22) for the total selection efficiency for events in our $Z \to \mu\mu$ candidate

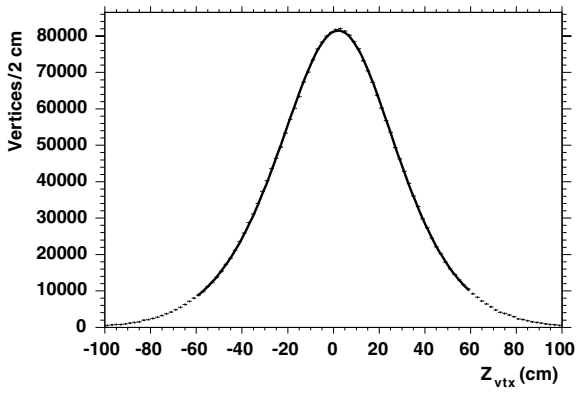

Figure 21. The measured $Z_{\rm vtx}$ distribution. The units on the horizontal axis are cm and there are a total of 100 bins from −100 cm to +100 cm. The curve is the fit to the luminosity function (equation (23)) for $|z| < 60$ cm, and the resulting fit with 55° of freedom has a χ^2 of 119.

Table 26. Results of $Z \to \ell\ell$ combined event efficiency calculations.

Candidate sample	$\epsilon_{\rm tot}$
$Z \to ee$	0.713 ± 0.012
$Z \to \mu\mu$	0.713 ± 0.015

sample:

$$\epsilon_{\rm tot}^{Z\to\mu\mu} = \epsilon_{\rm vtx} \times \epsilon_{\rm cos}^{Z} \times \epsilon_{\rm trk}^{2} \times \epsilon_{\rm lid}^{2} \times \epsilon_{\rm iso}^{2} \times \epsilon_{\rm rec} \times \epsilon_{\rm tid} \times \epsilon_{\rm trg} \times [1 + f_{\rm dd} \times (1 - \epsilon_{\rm rec} \times \epsilon_{\rm tid} \times \epsilon_{\rm trg})]. \tag{22}$$

Based on the expressions in equations (19) and (22), we can substitute our measured values for the individual efficiency terms and determine the combined event selection efficiencies for our $Z \to \ell\ell$ candidate samples. The resulting values are shown in table 26.

6.4. Vertex finding efficiency

Our requirement that the z-position of the primary event vertex be within 60 cm of the center of the CDF detector ($|Z_{\rm vtx}| \leqslant 60$ cm) limits the event acceptance to a fraction of the full luminous region for $p\overline{p}$ collisions. However, the luminosity estimate used in our cross-section measurements is based on the full luminous range of the beam interaction region. We use minimum-bias data to measure the longitudinal profile of the $p\overline{p}$ luminous region, and this profile is subsequently used to estimate the fraction of interactions within our fiducial range in z.

Figure 21 shows the distribution of measured positions along the z-axis (parallel to beams) for reconstructed primary vertices in minimum-bias events. The minimum-bias events are taken from the same set of runs from which our candidate samples are constructed. In addition, the minimum-bias data is weighted to ensure that it has the same run-by-run integrated luminosity as the cross-section event samples. We fit the distribution in figure 21 using the following form of the Tevatron beam luminosity function:

$$\frac{{\rm d}\mathcal{L}(z)}{{\rm d}z} = N_0 \frac{\exp\left(-z^2/2\sigma_z^2\right)}{\sqrt{\left[1 + \left(\frac{z-z_{01}}{\beta^*}\right)^2\right]\left[1 + \left(\frac{z-z_{02}}{\beta^*}\right)^2\right]}}. \tag{23}$$

The five free parameters of the fit are $N_0, \sigma_z, z_{01}, z_{02}$ and β^*. The Z_{vtx} distribution has some biases at large values of z due to increased contamination from non-$p\overline{p}$ interactions such as those originating from beam-gas collisions and due to the decrease of COT tracking acceptance far away from the center of the detector. We avoid these biases by only fitting the measured Z_{vtx} distribution to our function for $\mathrm{d}\mathcal{L}(z)/\mathrm{d}z$ in the region where $|z| < 60$ cm. Within this finite range in z, the fraction of events not from $p\overline{p}$ collisions is negligible and the COT tracking acceptance is high and uniform.

The acceptance of our requirement on the z-position of the primary event vertex ($|Z_{\text{vtx}}| < 60$ cm) is calculated as

$$\epsilon_{\text{vtx}}(|z| < 60) = \frac{\int_{-60}^{+60} [\mathrm{d}\mathcal{L}(z)/\mathrm{d}z]\,\mathrm{d}z}{\int_{-\infty}^{+\infty} [\mathrm{d}\mathcal{L}(z)/\mathrm{d}z]\,\mathrm{d}z}\,. \tag{24}$$

We perform the fit to the data and evaluate the acceptance for both the full sample and several sub-samples of our minimum-bias data set. We observe slight differences in the various sub-samples indicating small changes over time in the z-profile of $p\overline{p}$ collisions in the interaction region of our detector. The maximum shift seen in the measured acceptance among the various sub-samples is 0.6%, and we assign half of this value as a systematic uncertainty on the efficiency measurement. The statistical uncertainty on the measurement is assigned based on fit errors obtained from the z_{vtx} fit for the full minimum-bias sample. Using the techniques described above, we measure the signal acceptance of our cut on the z-position of the primary event vertex to be

$$\epsilon_{\text{vtx}} = 0.950 \pm 0.002\ (\text{stat.}) \pm 0.003\ (\text{syst.}).$$

6.5. Tracking efficiency

We define tracking efficiency as the fraction of high p_T leptons contained within our geometrical acceptance for which our offline tracking algorithm is able to reconstruct the lepton track from hits observed in the COT. We measure this quantity using a sample of clean, unbiased $W \to e\nu$ candidate events based on a tight set of calorimeter-only selection criteria. The events for this sample were collected using a trigger path based on calorimeter $\not\!\!E_T$ requirements to ensure that the sample is unbiased with respect to XFT tracking requirements in the hardware portion of the trigger and track reconstruction in the software portion. Events are required to have an electromagnetic calorimeter cluster with $E_T > 20\,\text{GeV}$ and overall event $\not\!\!E_T > 25\,\text{GeV}$. Since we can not use a track matching requirement to help reduce non-electron backgrounds, we apply a tighter than normal set of electron identification criteria on the electromagnetic cluster itself. We also remove candidate events containing additional reconstructed jets in the calorimeter with $E_T > 3$ GeV and require that the p_T of the reconstructed W boson is above 10 GeV/c. These cuts are designed to remove background events in our sample originating from QCD dijet processes.

Our tracking efficiency measurement is obtained from the fraction of events in this candidate sample which have a COT track pointing to the electromagnetic cluster. Matching, reconstructed tracks in the COT are required to point within 5 cm of the calorimeter electromagnetic cluster seed tower. In order to be absolutely sure that we are not including track-less background events in our efficiency calculation, we also require that our candidate events have a reconstructed track based entirely on hits in the silicon tracking detector (independent of the central outer tracking chamber) pointing at the electromagnetic cluster. A total of 1368 candidate events in our 72.0 pb^{-1} sample have a matching silicon track. Of these, 1363 events also contain a matching reconstructed track based solely on hits in the central outer

tracker yielding a COT tracking efficiency of $\epsilon_{\rm trk}(Data) = 0.9963^{+0.0035}_{-0.0040}$. The uncertainty on the measurement is primarily systematic and is based on studies of both silicon-only track fake rates and correlated failures in COT and silicon based tracking algorithms.

We compare the tracking efficiency measured in the data with an equivalent measurement based on our $W \rightarrow e\nu$ simulated event sample. Using the same technique, we obtain a simulation tracking efficiency of $\epsilon_{\rm trk}(MC) = 0.9966^{+0.0015}_{-0.0024}$, consistent with our measured value from data. A study of failing simulated events reveals that the small tracking inefficiency we measure is mainly due to bremsstrahlung radiation where the silicon-only track points in the direction of the hard photon and the COT track follows the path of the soft electron (pointing away from the high E_T electromagnetic cluster). Since the loss of events due to this process is already accounted for in our acceptance calculation, we avoid double counting by taking the ratio of the tracking efficiency measured in data to that measured in simulation as our net tracking efficiency. Based on this approach, our final value for the COT tracking efficiency is $\epsilon_{\rm trk} = 1.000 \pm 0.004$ where the uncertainty is the combined statistical and systematic uncertainty of our measurement technique.

6.6. Reconstruction efficiency

The lepton reconstruction efficiency is defined as the fraction of real leptons that is within our geometrical acceptance and has matching, reconstructed COT tracks which are subsequently reconstructed as leptons by our offline algorithms. In the case of electrons, this efficiency corresponds to the combined probability for forming the electromagnetic cluster and matching it to the associated COT track. For muons, it is the probability for reconstructing a stub in the muon detectors and matching the stub to the corresponding COT track.

The reconstruction efficiency is measured using the unbiased, second legs of $Z \rightarrow \ell\ell$ decays. The leptons from Z boson decays have a similar momentum spectrum to those originating from W boson decays and are embedded in a similar event environment. Events are required to have at least one fully reconstructed lepton leg that satisfies the complete set of lepton identification criteria used in the selection of our candidate samples. The same lepton leg must also satisfy the requirements of the corresponding high p_T lepton trigger path to ensure that the second leg is unbiased with respect to the trigger. A lepton leg satisfying these requirements is then paired with a second opposite-sign, high p_T track in the event. If the invariant mass of a lepton-track pair lies within the Z boson mass window, $80\ {\rm GeV}/c^2 < M_{\ell\ell} < 100\ {\rm GeV}/c^2$, the second track leg is utilized as a candidate for testing the lepton reconstruction efficiency. In the case of $Z \rightarrow \mu\mu$ candidate events only, the second track leg is also required to have associated calorimeter energy deposition consistent with a minimum ionizing particle which reduces backgrounds from fake muons without biasing the measurement. In the subset of $Z \rightarrow \ell\ell$ candidate events where each track leg is a reconstructed lepton passing the full set of identification and trigger criteria, both legs are unbiased lepton candidates and included in the efficiency measurement.

Each candidate track leg is extrapolated to determine if it points at an active area of the calorimeter or muon detectors as appropriate. If the track does point at an active detector region, it is expected to be reconstructed as a lepton. The fraction of this subset of candidate tracks which are in fact reconstructed as leptons provides our measurement of the reconstruction efficiency. Figure 22 shows the invariant mass distributions for muon-track pairs in cases where the second track is and is not reconstructed as a muon. The small peak seen near the Z boson mass in the latter case indicates that we do observe a non-negligible muon reconstruction inefficiency in the data. However, some of the measured inefficiency is attributable to the effects of multiple scattering. A particle associated with a track that points at an active

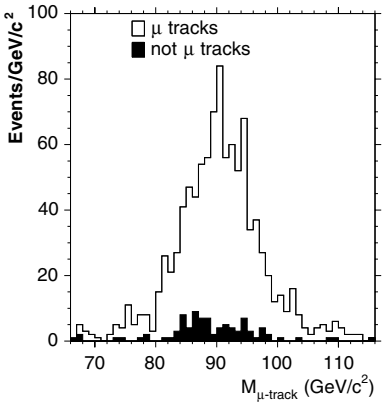

Figure 22. Invariant mass of muon-track pairs for the muon reconstruction-efficiency measurement. We show the distribution for pairs in which the track is a reconstructed as a muon track (open histogram) and for pairs in which the track is not reconstructed as a muon track (solid histogram). Only the region between 80 GeV/c^2 and 100 GeV/c^2 is used for the efficiency calculation.

Table 27. Summary of lepton reconstruction efficiency measurements. Because plug electron candidates are not required to have a matching reconstructed track, the corresponding reconstruction efficiency is one by definition.

Lepton	Data efficiency	Simulation efficiency	Net efficiency
Central electrons	0.990 ± 0.004	0.992 ± 0.001	0.998 ± 0.004
Plug electrons	1.000	1.000	1.000
Muons	0.935 ± 0.007	0.980 ± 0.001	0.954 ± 0.007

detector region can in some cases pass outside of this region due to the cumulative effects of interactions with material in the detector. This effect is modeled using the simulated event samples. All real reconstruction inefficiencies observable in the simulation are accounted for in the acceptance calculation and must not be double counted in the lepton reconstruction efficiency measurement. Therefore, we determine our net lepton reconstruction efficiency by dividing the value measured in data by the value obtained from an equivalent measurement using simulation. The lepton reconstruction efficiency measurements for electrons and muons are summarized in table 27. Plug electron candidates are not required to have a matching reconstructed track and therefore by our definition have a fixed reconstruction efficiency of 100%. We make additional checks to confirm that the leptons in our test samples are a good match for the leptons in our candidate samples and based on this agreement take the statistical uncertainty of our measurements as the total uncertainty on the reconstruction efficiencies.

6.7. Lepton identification isolation cut efficiencies

The efficiencies of our lepton identification and isolation cuts are also determined directly from the data using $Z \to \ell\ell$ events. We use slightly different techniques for measuring these efficiencies for electrons and muons. The motivation for using separate methods is the non-negligible fraction of background events in the $Z \to ee$ candidate sample in which at least one of the reconstructed electrons is either a fake or the direct semileptonic decay product

of a hadron. In order to accurately measure the selection efficiencies for electrons originating from W and Z boson decays, it is important to correct for the contribution of these background events to our efficiency calculation. Since these types of backgrounds are negligible in our $Z \to \mu\mu$ candidate sample, we are able to use a more aggressive approach which maximizes the statistical size of the muon candidates used to determine these efficiencies.

As previously mentioned, the identification and isolation efficiencies for leptons are determined in a specific order to avoid double-counting correlated inefficiencies between different groups of selection criteria. The order we employ in making these measurements is the following: efficiencies from loose identification cuts, isolation cut efficiencies, and efficiencies from tight identification cuts. This ordering is chosen to simplify the extraction of combined selection efficiencies for $Z \to \ell\ell$ events from our individual, measured efficiency terms. To protect this ordering, we require that lepton candidates used to measure each group of selection efficiencies satisfy the selection criteria associated with all groups defined to be earlier within our assigned order.

To minimize backgrounds in the $Z \to ee$ event sample used to make the efficiency measurements, we require that at least one of the two reconstructed electrons passes the full set of identification and isolation criteria used in the $W \to e\nu$ analysis. The second electron leg in each event, referred to here as the probe electron, is simply required to satisfy the geometric and kinematic cuts that define the acceptance of our candidate samples. In addition, the invariant mass of the electron pair is required to be within a tight window centered on the measured Z boson mass ($75\ \mathrm{GeV}/c^2 < M_{ee} < 105\ \mathrm{GeV}/c^2$), which further reduces non-Z backgrounds in the sample. By definition, the electron passing the complete set of identification and isolation criteria is a central electron. Central–central $Z \to ee$ events satisfying the criteria listed above are used to measure central electron efficiencies, and central–plug events are used to measure plug electron efficiencies.

We define the number of central–central $Z \to ee$ candidates passing our criteria as N_{tc}. As mentioned above, each event has at least one electron passing the full set of identification and isolation criteria. Electrons of this type are referred to as tight. In some number of events in our candidate sample, N_{tt}, both electrons are found to satisfy the tight criteria. In the remaining events, the probe electron necessarily fails at least one part of our selection criteria. However, some number of these remaining events will satisfy a particular subset of the identification and isolation requirements corresponding to an efficiency term that we want to measure. The total number of events where the probe leg is found to satisfy a given subset of cuts is referred to as $N_{\mathrm{t}i}$. In this case, the corresponding efficiency for the subset of cuts being studied is determined from the expression given in equation (25). The variable i in this expression refers to the three sets of selection cut efficiencies to be measured ($1 =$ loose identification, $2 =$ isolation, and $3 =$ tight identification). In the second two cases, we limit our sample of probe electrons to those that satisfy the criteria associated with the lower numbered efficiency terms to avoid the double-counting problem discussed above. The net result is that for the second two cases $N_{\mathrm{tc}} = N_{\mathrm{t}(i-1)}$ and $N_{\mathrm{t}i}$ is re-defined as the number of events where the probe leg is found to pass the requirements associated with the efficiency term being measured and those numbered below it. This new definition implies that for the final case $N_{\mathrm{t}i}$ is simply equal to N_{tt}:

$$\epsilon_i = \frac{N_{\mathrm{t}i} + N_{\mathrm{tt}}}{N_{\mathrm{tc}} + N_{\mathrm{tt}}}. \tag{25}$$

One additional complication is that we must subtract the contribution of background to each of the input event totals in equation (25) to accurately measure the efficiencies for electrons produced in W and Z boson decays. For central–central $Z \to ee$ events, the background in

Table 28. $Z \to ee$ event counts used as inputs to the calculation of electron identification and isolation efficiencies.

Efficiency measurement	Symbol	i	N_{tc}	N_{ti}	N_{tt}	N_{tc} background	N_{ti} background	N_{tt} background	Efficiency
Loose identification cuts	ϵ_{lid}	1	1901	1751	1296	28.3	6.1	0.6	0.960 ± 0.004
Isolation cut	ϵ_{iso}	2	1751	1663	1296	6.1	−0.4	0.6	0.973 ± 0.003
Tight identification cuts	ϵ_{tid}	3	1663	1296	1296	−0.4	0.6	0.6	0.876 ± 0.007

Table 29. Input parameters to plug electron identification and isolation efficiency measurements using central–plug $Z \to ee$ candidates.

Efficiency measurement	Symbol	Number of probe electrons	Number passing selection criteria	Probe electron background	Passing electron background	Efficiency
Identification cuts	$\epsilon_{\text{id}}^{\text{plug}}$	2517	2126	108.4	15.0	0.876 ± 0.015
Isolation cut	$\epsilon_{\text{iso}}^{\text{plug}}$	2126	2111	15.0	14.1	0.993 ± 0.003

each event subset is determined from the number of equivalent same-sign events observed in the data sample. A correction for tridents (real $Z \to ee$ events where the charge of one electron is measured incorrectly due to the radiation of a hard bremsstrahlung photon) in the same-sign event totals is made based on the relative numbers of opposite-sign and same-sign events in our $Z \to ee$ simulated event sample. The event counts and background corrections for each of the input parameters used in the efficiency calculations are given in table 28.

The fraction of background events in the central–plug $Z \to ee$ candidate sample used to measure plug electron efficiencies is much larger than that in the central–central sample. In order to eliminate some of this additional background, we make an even tighter set of requirements on the isolation and electron quality variables associated with the central electron to pick the candidate events used to measure these efficiencies. As the probe leg in these candidates is the only plug electron of interest in the event, efficiencies are measured simply as the fraction of probe legs that satisfy the associated set of selection criteria. In the analyses reported here, plug electrons are utilized only as loose second legs for selecting $Z \to ee$ candidate events. There is therefore no corresponding tight identification cut efficiency to measure for plug electrons. However, the ordering of the loose identification and isolation cuts for plug electrons is identical to that used for electrons in the central region. We account for this ordering by requiring that the probe electrons used to measure the efficiency of the isolation cut satisfy the full set of loose plug electron identification cuts. We correct the number of probe legs in both the numerator and denominator of our efficiency calculations for the residual backgrounds remaining in our candidate sample. These backgrounds are estimated using electron fake rate calculations outlined in section 7. Based on this method, we obtain independent estimates for the background contributions from both QCD dijet and $W \to e\nu$ plus jet processes and sum them to obtain our final background estimates. The inputs to our plug electron efficiency measurements and the resulting efficiency values are summarized in table 29.

The calculation of muon identification and isolation efficiencies is simplified by the lack of significant backgrounds in our $Z \to \mu\mu$ candidate samples. To obtain the largest possible

Table 30. Input parameters to muon identification and isolation efficiency measurements using $Z \to \mu\mu$ candidates.

Efficiency measurement	Symbol	Number of probe muons	Number passing selection criteria	Efficiency
Loose identification cuts	ϵ_{lid}	1574	1469	0.933 ± 0.006
Isolation cut	ϵ_{iso}	1469	1443	0.982 ± 0.003
Tight identification cuts	ϵ_{tid}	1443	1381	0.957 ± 0.005

sample of probe muons for measuring these efficiencies, we make only a minimal set of requirements on the first muon leg in these events. In order to avoid selection biases, we simply require that at least one muon leg in each event satisfies both the trigger requirements and loose cuts used to select events into our high p_T muon sample from which the candidate events are chosen. The second muon leg in each of these events is then utilized as an unbiased probe leg for measuring our selection efficiencies. In the subset of candidate events where both muon legs satisfy the trigger and loose selection requirements of our sample, both muons are unbiased and included in our sample of probe muons. To ensure that we are selecting probe muons from a clean (low background) sample of $Z \to \mu\mu$ candidate events, we do require that the invariant mass of each muon pair lies within a tight window around the measured Z boson mass ($80\ \text{GeV}/c^2 < M_{\mu\mu} < 100\ \text{GeV}/c^2$) and remove any events identified by our tagging algorithm as cosmic ray candidates. After applying these criteria, we find that only 3 of over 1500 probe muons come from same-sign candidate events confirming the negligible background fraction in the event sample used for these measurements.

As in the case of electrons, the full set of muon identification cuts is divided into loose and tight subsets to simplify the calculation of the combined event selection efficiency for $Z \to \mu\mu$ candidate events. The second muon track leg in these events is not required to have a matching stub in the muon detector. Therefore, the identification cuts for muons which we refer to as loose are those that are applied to the track itself. The remaining tight selection cuts are those applied only to muon track legs with matching muon detector stubs. In some sense, the reconstruction of a matching stub in the muon detector is therefore also a tight selection criteria although we choose to treat the efficiency for this requirement separately. We use the same ordering of selection criteria (loose identification, isolation, and tight identification) as that used for electrons to avoid the double counting of correlated muon inefficiencies. Muon probe legs used to measure the efficiency for each set of selection criteria are required to satisfy all selection cuts corresponding to previously ordered efficiency terms. Table 30 summarizes the inputs to the muon efficiency calculations and the resulting efficiency values.

6.8. Trigger efficiency

As described in section 3, the data samples used to select our candidate events are collected via high p_T lepton-only trigger paths. The three-level trigger system utilized by the upgraded CDF data acquisition system reduces the 2.5 MHz beam-interaction rate into a final event collection rate on the order of 75 Hz. The first two levels utilize dedicated hardware to select events for readout from the detector, and the third level is a processor farm that runs a fast version of the full event reconstruction to pick out the final set of events to be written to tape. Level 1 lepton triggers are constructed from high p_T COT tracks identified in the fast tracking hardware matched with single tower electromagnetic energy deposits in the calorimeter (electrons) or groups of hits in the outer wire chambers (muons). Level 2 hardware is used to perform a more sophisticated calorimeter energy clustering algorithm on electron candidates to obtain

Table 31. Efficiencies for tracking requirements in high E_T electron trigger path.

Trigger level	Track requirement	Measured efficiency
Level 1	Fast tracker ($p_T > 8$ GeV/c)	0.974 ± 0.002
Level 2	Fast tracker ($p_T > 8$ GeV/c)	1.000 ± 0.000
Level 3	Full reconstruction ($p_T > 9$ GeV/c)	0.992 ± 0.001
Combined	Level 1 $\rightarrow$ Level 3	0.966 ± 0.002

improved E_T resolution. The improved E_T variable is utilized at level 2 to make tighter kinematic cuts on the electron candidates. No additional requirements are made on muon candidates at level 2. Events selected at level 2 are read out of the detector and passed to the level 3 processor farm. A fast version of the offline lepton reconstruction algorithms are run on each event, and the identified leptons are subjected to both kinematic and loose quality selection cuts.

The measurement of trigger efficiencies for electrons is simplified by the availability of secondary trigger paths that feed into our $W \rightarrow e\nu$ candidate sample. A trigger path based solely on calorimeter quantities is used to measure the efficiency of tracking requirements at each of the three trigger levels. This path utilizes identical calorimeter cluster requirements to those in the default electron path but does not require matching tracks to be found at any level. Instead, events are selected based on the presence of large $\not\!\!E_T$ in the calorimeter (15 GeV at level 1/level 2 and 25 GeV at level 3) associated with the high-energy neutrino in the W boson decays. For $W \rightarrow \mu\nu$ candidate events, the muon deposits only a small fraction of its energy into the calorimeter and hence the residual $\not\!\!E_T$ in the calorimeter is too small to allow for an equivalent trigger path for muon candidates. To measure the efficiencies of the electron trigger path track requirements, we select events from the secondary trigger path that pass the complete set of $W \rightarrow e\nu$ selection criteria. The fraction of events in this unbiased sample that satisfy the track requirements of our lepton-only trigger path at each of the three levels gives the corresponding efficiency for those requirements. The double counting of correlated inefficiencies between the different trigger levels is avoided by requiring that events used to measure higher level trigger efficiencies pass all of the tracking requirements associated with levels below that being measured.

Due to slight changes in the track trigger requirements over time, the corresponding efficiencies are measured in three run ranges. A final efficiency is determined by taking the luminosity weighted average of the results obtained for each run range. The event samples used to make these measurements were studied to look for possible trigger efficiency dependencies on other event variables such as electron isolation, number of additional jets in the events, total event energy, and electron charge. No dependencies were found for these variables, within the statistical uncertainties of our sample. We did observe a small trigger efficiency dependence as a function of the measured pseudorapidity of the electron track. We observe a small inefficiency for tracks near $\eta_{\text{det}} \sim 0$ due to wire spacers in the tracking chamber and reduced overall charge collection due to the shorter track path length through the chamber. However, the effect of this dependence on our final efficiency results was found to be negligible within our measurement uncertainties. The final efficiency results for the electron trigger path tracking requirements at each trigger level are shown in table 31.

In order to measure the total efficiency of our electron trigger path, we additionally need to measure the efficiencies of the calorimeter cluster requirements at each level of the trigger. The requirement of an electromagnetic cluster with $E_T > 8$ GeV at level 1 is studied using reconstructed electromagnetic objects found in muon-triggered events. We determine the

highest energy trigger tower associated with each object and check to see if the level 1 trigger bit corresponding to this tower is turned on in the data. We measure a turn-on efficiency of 99.5% for trigger towers with a measured electromagnetic energy between 8 GeV and 14 GeV and 100% for those measured above 14 GeV. The small inefficiency observed for towers with measured energies below 14 GeV is due to an additional level 1 requirement placed on the ratio of hadronic and electromagnetic energies ($E_{\rm had}/E_{\rm em} < 0.05$) in towers with energies below this cut-off value. The effect of this inefficiency on the fully reconstructed electrons in our $W \to e\nu$ candidate events is determined by checking how often the associated trigger tower with the highest electromagnetic E_T has a measured energy below 14 GeV. We find that less than 1% of the reconstructed electrons in our candidate sample ($E_T > 25$ GeV) do not have at least one associated trigger tower with $E_T > 14$ GeV. Based on these numbers, we estimate the overall trigger efficiency for the level 1 electromagnetic cluster requirement to be 100% for the events in our candidate samples.

Additional secondary trigger paths are used to measure the efficiencies of the levels 2 and 3 cluster requirements in our default electron trigger path. The efficiency of the level 2 cluster requirement is obtained using events collected with two additional secondary trigger paths that have no level 2 selection requirements other than simple prescales. The levels 1 and 3 trigger requirements in these paths are equivalent to in one case those of the default path and in another those of the path used to collect events for measuring the efficiencies of track requirements. The subset of these events that pass our full set of $W \to e\nu$ selection criteria are also found to satisfy the level 2 cluster trigger criteria. Based on these samples we conclude that the efficiency of the level 2 electron cluster requirement is 100% for reconstructed electrons also satisfying our selection criteria for tight central electrons. Since the electron clustering algorithm run in the level 3 processor farms is nearly identical to that used in offline reconstruction, we expect candidate events with high E_T electrons to also satisfy the level 3 cluster requirements of our trigger path. However, due to slight differences in the calorimeter energy corrections applied at level 3 and offline, it is possible that we could observe trigger inefficiencies close to the E_T threshold utilized for level 3 clusters. To check for this inefficiency, we collect events on an additional secondary trigger path which is based on the levels 1 and 2 requirements of our default electron trigger path but no requirements at level 3 other than a simple prescale. We find that all of the events collected on this path which satisfy our event selection criteria also satisfy the level 3 cluster criteria of our default trigger path. Based on this study, the efficiency of the level 3 cluster requirement for events in our candidate samples is also 100%. Since we do not measure inefficiencies for the cluster requirements of our trigger path at any of the three levels, we conclude that the overall efficiency of our default trigger path for electrons is completely determined by the measured efficiencies of the track criteria given in table 31.

As mentioned above we do not have the benefit of an equivalent set of secondary trigger paths for collecting $W \to \mu\nu$ candidate events to measure the efficiencies of our muon trigger path requirements. Instead, we use $Z \to \mu\mu$ candidate events in which both muons satisfy the full set of isolation and identification cuts used to define our samples. To avoid background events we require that the invariant mass of the dimuon pair lies in a tight window around the Z boson mass ($76\ {\rm GeV}/c^2 < M_{\mu\mu} < 106\ {\rm GeV}/c^2$) and that the event has not been identified as a cosmic ray by our tagging algorithm. In this sample we know that at least one of the two muons in the event satisfied the muon trigger path requirements and can make a measurement of the muon trigger efficiency based on the fraction of events in which both muons meet the criteria of our trigger path. If we define $\epsilon_{\rm trg}$ as the single muon trigger efficiency we want to measure, then $(\epsilon_{\rm trg})^2$ is the fraction of events containing two triggered muons, and $2(\epsilon_{\rm trg})(1-\epsilon_{\rm trg})$ is the fraction of events with only one triggered muon. There is also a remaining fraction of events $(1-\epsilon_{\rm trg})^2$ which contain no triggered muons, but these events do not make it into our $Z \to \mu\mu$

Table 32. Efficiencies for high p_T muon trigger path.

Trigger level	Number of $Z \to \mu\mu$ candidate events	Number of events with 2 muon triggers	Efficiency
Level 1	338	293	0.929 ± 0.011
Level 3	138	137	0.996 ± 0.004
Combined	–	–	0.925 ± 0.011

candidate sample. Based on these definitions, the number of candidate events in our sample in which both muons meet the trigger criteria, $N_{2\text{trg}}$ divided by the total number of events in the sample, N_{tot}, can be expressed with equation (26). From this expression we obtain the formula shown in equation (27) which gives the muon trigger efficiency as a function of this fraction F:

$$F = \frac{N_{2\text{trg}}}{N_{\text{tot}}} = \frac{(\epsilon_{\text{trg}})^2}{(\epsilon_{\text{trg}})^2 + 2(\epsilon_{\text{trg}})(1 - \epsilon_{\text{trg}})} \tag{26}$$

$$\epsilon_{\text{trg}} = \frac{2 \cdot F}{1 + F}. \tag{27}$$

To check whether an individual muon in our candidate sample satisfies the requirements of our muon trigger path, we first look at the hits on the reconstructed muon stub to determine the position of the muon with respect to the 144 level 1 muon trigger towers (2.5° each in ϕ) defined in the hardware. We then check to see if the trigger bits corresponding to each individual requirement of our trigger path are set for the matched trigger tower. The level 1 requirements of our trigger path include both a high p_T COT track identified in the fast tracking hardware and a sufficient set of matching hits in the muon detector wire chamber(s) along the path of the reconstructed muon. Matching CSX scintillator hits are additionally required in the region of the muon detector between 0.6 and 1.0 in η_{det} (CMX region). No significant additional trigger requirements are made at level 2 for muon candidates. In order to measure the efficiency of the muon reconstruction algorithms at level 3, we use the subset of events in the $Z \to \mu\mu$ candidate sample described above in which both muons are found to satisfy the level 1 trigger criteria. This restriction is made to ensure that we do not double-count correlated inefficiencies between the different trigger levels. In addition, we require that one of the two muons is found in the region of the muon detector between 0.0 and 0.6 in η_{det} (CMUP region) while the other is found in the region between 0.6 and 1.0 in η_{det} (CMX region). Since different level 3 muon reconstruction algorithms are run in these two regions, it is simple to check if both or only one of the muons in these events satisfy the level 3 requirements of our muon trigger path. The input parameters to our muon trigger path efficiency calculations are shown in table 32 along with the final results of these calculations.

6.9. Cosmic tagger efficiency

The tagging algorithm used to remove cosmic ray events in our $W \to \mu\nu$ and $Z \to \mu\mu$ candidate samples is discussed in section 7.5. We measure the fraction of real events tagged as cosmic rays by this algorithm for both candidate samples using the corresponding electron decay mode samples. The tagging algorithm is based solely on the hit timing information associated with reconstructed tracks in the COT. Since the kinematics of W and Z boson decays into electrons and muons are nearly identical, we expect that the reconstructed electron tracks in $W \to e\nu$ and $Z \to ee$ candidate events are a good model for the muon tracks in the

corresponding decay channels. Unlike the muon channels, however, the electron decay mode candidate samples have a negligible cosmic background. Therefore, we obtain a measurement of the fraction of real $W \to \mu\nu$ and $Z \to \mu\mu$ signal events tagged as cosmic ray candidates directly from the observed fraction of events in the corresponding electron channels which our algorithm identifies as cosmic ray candidates. In order to make the tracks in the electron events match as closely as possible with those in the muon events, we first apply the muon track impact parameter cut described in section 4 to each of the electron candidate tracks in these samples. This additional requirement reduces the number of events in the $W \to e\nu$ candidate sample to 37 070. Of the remaining events, only five are tagged as cosmic ray candidates by our modified version of the cosmic tagging algorithm. The resulting efficiency for a W boson decay not to be tagged as a cosmic by our algorithm is $\epsilon^{W}_{\cos} = 0.9999 \pm 0.0001$. Applying the track impact parameter cut to the $Z \to ee$ sample reduces the total number of candidate events to 1680. Of these events, only one is tagged as a cosmic by our modified tagging algorithm. The resulting efficiency for a Z boson decay not to be tagged as a cosmic by our algorithm is $\epsilon^{Z}_{\cos} = 0.9994 \pm 0.0006$.

6.10. Over-efficiency of Z-rejection criteria

The criteria for rejecting $Z \to \mu\mu$ events in our $W \to \mu\nu$ candidate sample are defined in section 4. A small fraction of real signal events are also removed from our candidate sample via this selection criteria. We measure the efficiency for signal events to survive the Z-rejection cuts directly from simulation. The resulting value, 0.9961 ± 0.0001, is determined by the number of $W \to \mu\nu$ candidate events in our simulated sample that exclusively fail the Z-rejection criteria.

The systematic uncertainty on this efficiency is based on a comparison of the shape of the invariant mass spectrum for the muon plus track candidate events rejected solely due to this criteria to the shape of the same spectrum obtained from $\gamma^*/Z \to \mu\mu$ simulated events. A comparison of the ratio of rejected events inside and outside the Z-mass window ($66\ \text{GeV}/c^2 < M_{\mu\mu} < 116\ \text{GeV}/c^2$) to that found in the γ^*/Z simulation sample provides a good measure whether our rejected events are a relatively pure sample of γ^*/Z decays. Based on this approach, we measure an additional systematic of $\pm 0.17\%$ to apply to the Z-rejection efficiency value obtained from simulation. The final result is $\epsilon_{\text{z-rej}} = 0.9961 \pm 0.0017$.

7. Backgrounds

Other physics processes can produce events that mimic the signature of $W \to \ell\nu$ and $Z \to \ell\ell$ events in our detector. Some processes have similar final-state event topologies to those of our signal samples and others can fake similar topologies if a non-lepton object within the event is misidentified as an electron or muon. In this section, the sources of backgrounds to W and Z events are discussed. We separate the background sources into three main categories: events in which hadronic jets fake leptons; events from other electroweak processes; and events from non-collision cosmic ray backgrounds. The techniques used to estimate the contribution to our candidate samples from each background source are given in this section along with the final estimates.

7.1. Hadron jet background in $W \to \ell\nu$

Extracting the contribution of events to the $W \to \ell\nu$ candidate samples in which real or fake leptons from hadronic jets are reconstructed in the detector is one of the more challenging

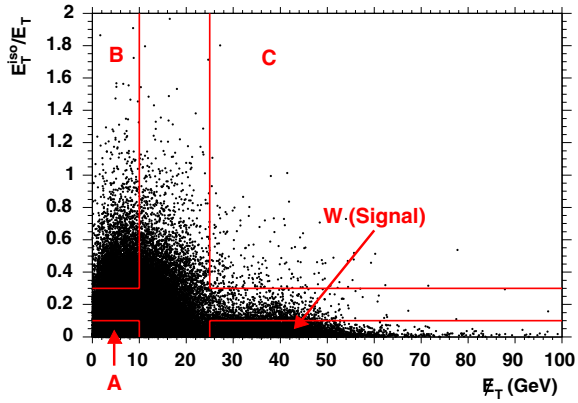

Figure 23. $E_T^{\rm iso}/E_T$ versus event $\not\!\!E_T$ for $W \to e\nu$ candidates (no cuts on the lepton isolation fraction variable or the event $\not\!\!E_T$). The definitions of regions A, B and C which are used in the calculation of the hadronic background are provided in the text.

components of our measurements. Real leptons are produced both in the semileptonic decay of hadrons and by photon conversions in the detector material. Some events also contain other particles in hadronic jets which are misidentified and reconstructed as leptons. Typically, these types of events will not be accepted into our W candidate samples because we require large event $\not\!\!E_T$. In a small fraction of these events, however, a significant energy mismeasurement does reproduce the $\not\!\!E_T$ signature of our samples. Because of the large total cross section for hadronic jets in our detector, even this small fraction results in a substantial number of background events in our W candidate samples. These events are particularly difficult to model in the simulation since the associated energy mismeasurement makes them unrepresentative of typical hadronic events. In order to estimate the background contribution of these sources to our samples, we release the selection criteria on lepton isolation and event $\not\!\!E_T$ and use events with low lepton isolation and low $\not\!\!E_T$ as a model of the background in the low lepton isolation and high $\not\!\!E_T$ W signal region. The contributions in the low and high $\not\!\!E_T$ regions are normalized to the number of events in those regions with high lepton isolation based on the assumption that there is no correlation between lepton isolation and $\not\!\!E_T$ in the hadronic background.

Figure 23 shows the lepton isolation fraction variable plotted against event $\not\!\!E_T$ for $W \to e\nu$ candidates (no cuts on lepton isolation fraction or event $\not\!\!E_T$). In the lepton isolation fraction versus $\not\!\!E_T$ parameter space, we define four regions as follows:

- Region A: $E_T^{\rm iso}/E_T < 0.1$ and $\not\!\!E_T < 10$ GeV
- Region B: $E_T^{\rm iso}/E_T > 0.3$ and $\not\!\!E_T < 10$ GeV
- Region C: $E_T^{\rm iso}/E_T > 0.3$ and $\not\!\!E_T > 25$ GeV (20 GeV for $W \to \mu\nu$)
- Region W: $E_T^{\rm iso}$
  $big/E_T < 0.1$ and $\not\!\!E_T > 25$ GeV (20 GeV for $W \to \mu\nu$).

Region W is the $W \to \ell\nu$ signal region and the others contain mostly hadronic background events. The background contribution to the W signal region, $N_W^{\rm bck}$, is estimated using

$$\frac{N_W^{\rm bck}}{N_{\rm evt}^{\rm C}} = \frac{N_{\rm evt}^{\rm A}}{N_{\rm evt}^{\rm B}}, \tag{28}$$

where $N_{\rm evt}^{\rm A}$, $N_{\rm evt}^{\rm B}$, $N_{\rm evt}^{\rm C}$ are the number of events in regions A, B and C, respectively, as defined above. This technique has been previously described in [27, 37] and more recently in [69].

Table 33. Summary of hadronic background event contribution estimates to the $W \to e\nu$ and $W \to \mu\nu$ candidate samples. The statistical and systematic uncertainties are indicated.

	Uncorrected $W \to e\nu$	Corrected $W \to e\nu$	Uncorrected $W \to \mu\nu$	Corrected $W \to \mu\nu$
Region A	30 023	26 655	3926	3575
Region B	5974	5972	5618	5615
Region C	228	131	496	345
Region W	37 584	37 584	31 722	31 722
Hadronic background	1146	587	346	220
Statistical error	78	52	17	13
Systematic error	–	294	–	110
Background fraction	$3.0 \pm 0.2\%$	$1.6 \pm 0.8\%$	$1.1 \pm 0.1\%$	$0.7 \pm 0.4\%$

A simple approach would be to assume that all of the events in regions A, B and C are hadronic background events. In that case, the observed number of data events in each region can be used directly in equation (28) to extract the hadronic background contribution to the W signal region. We further improve our estimate, however, by accounting for the fact that these regions contain small fractions of signal events and events from other electroweak background processes such as $Z \to \ell\ell$ and $W \to \tau\nu$ in addition to hadronic background events. Figure 24 shows distributions of lepton isolation fraction versus $\not\!\!E_T$ for simulated events passing the full set of selection criteria (no cuts on lepton isolation fraction or $\not\!\!E_T$) for the $W \to e\nu$ signal, $Z \to ee$ background, and $W \to \tau\nu$ background samples. From these distributions, and the equivalent ones for $W \to \mu\nu$ candidates, we obtain modeled event fractions in regions A, B and C relative to the signal region for the signal and other electroweak background processes. Based on these fractions and our estimates for the relative contributions of $W \to \ell\nu$, $Z \to \ell\ell$, and $W \to \tau\nu$ in the signal region (see section 7.3), we correct the observed numbers of events in regions A, B and C to remove the contributions from non-hadronic backgrounds. A more accurate estimate of the hadronic background in the W signal region is then obtained from equation (28) using these corrected inputs. Table 33 summarizes both the corrected and uncorrected hadronic background estimates for the W signal region obtained from equation (28) for the $W \to e\nu$ and $W \to \mu\nu$ decay channels.

Since the lower limit on lepton isolation fraction and upper limit on event $\not\!\!E_T$ used to define regions A, B and C are arbitrary choices, we check the robustness of our technique for obtaining the hadronic background estimates by raising and lowering the cuts used to define these regions. We take observed changes in the estimated hadronic backgrounds as a systematic uncertainty on our measurement technique. Figure 25 shows the dependence of the estimated hadronic background contribution to the signal region as a function of the lepton isolation fraction and event $\not\!\!E_T$ values used to define the non-signal regions both before and after correcting the number of observed events in regions A, B, C for $W \to e\nu$ signal and other background processes. We observe similar dependencies using the $W \to \mu\nu$ candidate sample. The background estimate is mostly independent of the selection of the lower $\not\!\!E_T$ border for regions A and B but does depend on the location of the upper lepton isolation fraction border for regions B and C. Although we observe some evidence from simulated event samples that the observed fluctuations are a feature of the hadronic background, we choose to use a conservative systematic uncertainty that covers the full range of the fluctuations seen in figure 25. We estimate the range of the observed fluctuations to be within 50% of our central values corresponding to uncertainty estimates of $\pm$ 294 events in the $W \to e\nu$ candidate event sample and $\pm$ 110 events in the $W \to \mu\nu$ candidate sample (see table 33).

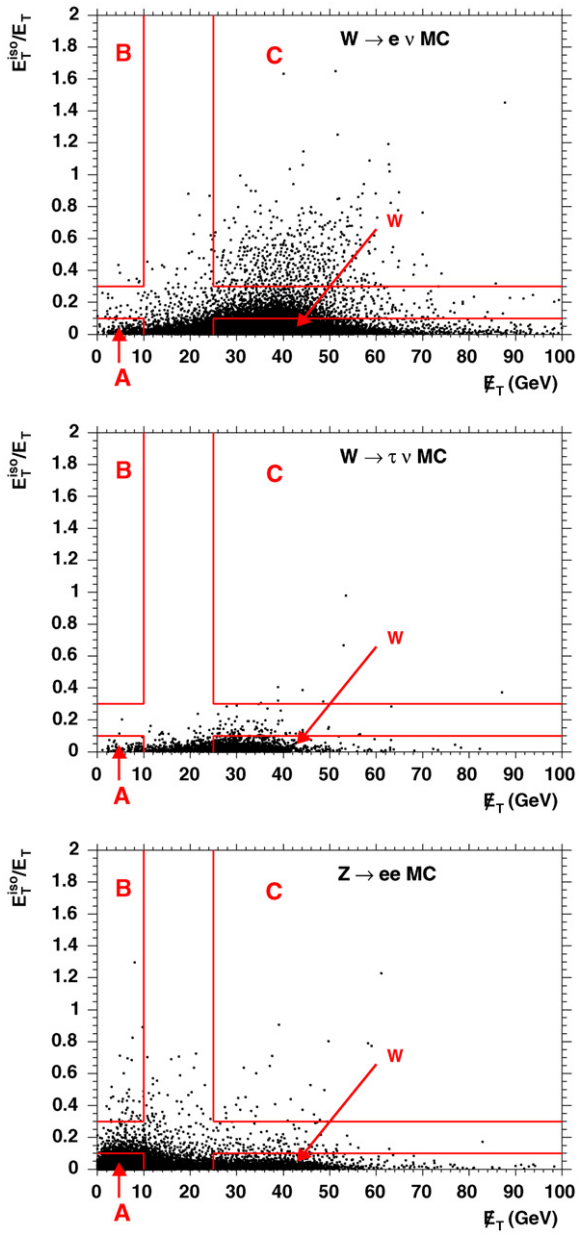

Figure 24. E_T^{iso}/E_T versus event $\not\!\!E_T$ for the simulated $W \to e\nu$ signal, $W \to \tau\nu$ background, and $Z \to ee$ background samples. We correct the observed number of data events in regions A, B, C to account for events from these processes when estimating the hadronic background in the $W \to \ell\nu$ candidate samples.

We make an independent cross-check of the estimated hadronic background in $W \to e\nu$ events by applying a measured rate for jets faking electrons to a generic hadronic jet sample. The rate for jets faking electrons is measured from events with at least two jets with $E_T >$ 15 GeV, $\not\!\!E_T < 15$ GeV, and no more than one loose electron. These requirements ensure that

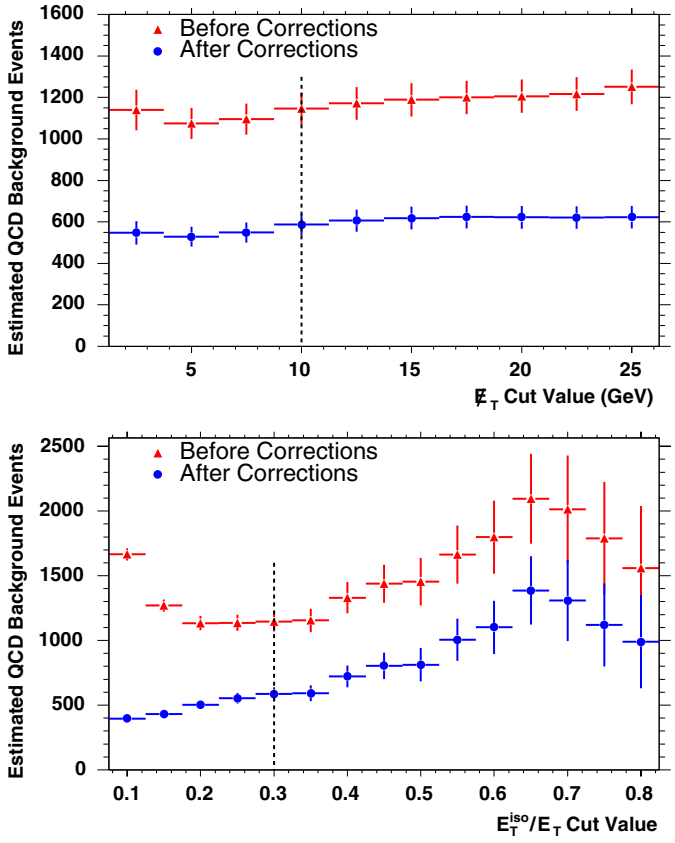

Figure 25. Dependence of hadronic background estimate on the $E_T^{\rm iso}/E_T$ and event $\not\!\!E_T$ cut values used to define the control regions for $W \to e\nu$. The results both before and after corrections for signal and electroweak background contributions to regions A, B and C are applied are shown in triangles and circles, respectively.

the input sample has a negligible contribution from real W and Z events. From this sample, the jet fake rate is defined as the fraction of reconstructed jets with $E_T > 30$ GeV that are also found to pass the standard set of tight electron cuts.

We use the E_T dependence of the jet fake rate in the background estimate. Because of differences in the clustering algorithms used for electrons and jets, the reconstructed energies of electrons originating from hadronic jets are smaller than the reconstructed energies of the jets. Scale factors are applied to convert the measured jet energies into corresponding electron cluster energies, and as a consequence the lowest E_T bins are not included in the fitted constant for the jet fake rate. A significant uncertainty on the final background estimate is assigned, however, based on the results obtained using different models for fitting the E_T dependence of the jet fake rate. The measured fake rate is applied to jets in an inclusive jet data sample to determine how often these types of hadronic events with fake electrons satisfy the additional selection criteria of our $W \to e\nu$ candidate sample. Jets in the inclusive sample are required to have $E_T^{\rm scaled} > 25$ GeV where $E_T^{\rm scaled}$ is the jet E_T scaled down to the E_T of the fake electron to match the electron selection criteria of our sample. The distribution in figure 26 is the resulting $\not\!\!E_T$ distribution for the inclusive jet sample weighted by the jet fake rate. The events

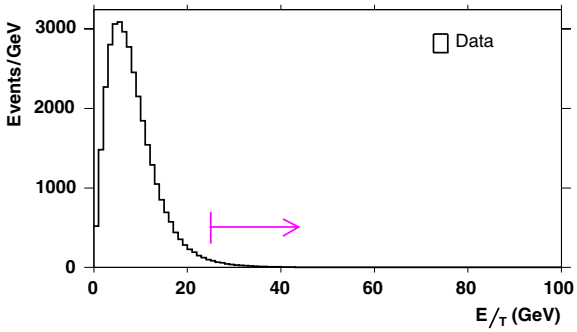

Figure 26. $\not\!\!E_T$ distribution for inclusive jet sample weighted by measured jet fake rate. The arrow indicates the location of the selection cut on $\not\!\!E_T$ used to select $W \to e\nu$ candidate events.

above the candidate sample $\not\!\!E_T$ cut of 25 GeV are integrated giving 800 ± 300 background events, consistent with the result obtained using our default technique.

7.2. Hadron jet background in $\gamma^*/Z \to \ell\ell$

Our $Z \to \ell\ell$ candidate samples have smaller overall contributions from background sources than the $W \to \ell\nu$ samples. One common background source is events in which one or both leptons are either real or fake leptons from hadronic jets. We expect that the two leptons in these types of events have no charge correlation so that the numbers of opposite-sign and same-sign lepton pairs from this source are roughly equal. Based on this assumption, we use the number of same-sign lepton pair candidates to place an upper limit on the number of hadronic background events in our opposite-sign dilepton pair candidate samples. This approach is only viable for events with two central leptons where the lepton charge is taken from the reconstructed track. As discussed later in this section, the background contribution to $Z \to ee$ events with one central electron and one plug electron is measured using a variation of the jet fake rate method described previously.

Since the calorimeter energy associated with muon candidates is required to be consistent with a minimum-ionizing particle, the probability for a hadronic jet to fake a muon is significantly smaller than that for an electron. Despite the fact that we make no opposite-sign charge requirement on the two muon legs in our $Z \to \mu\mu$ candidate events, none of the 1785 events in this sample are observed to contain a same-sign muon pair. Based on finding no such events, we estimate a background contribution of $0.0^{+1.1}_{-0.0}$ events from muons produced in hadronic jets.

The number of same-sign events observed in the $Z \to ee$ candidate sample needs to be corrected for a fraction of real $Z \to ee$ events that are reconstructed as same-sign electron pairs. We observe a total of 22 events with same-sign electron pairs corresponding to our sample 1730 $Z \to ee$ candidate events with two central electrons. The invariant mass distributions for both the opposite-sign and same-sign electron pairs in our candidate sample are shown in figures 18 and 27. Both distributions show a peak in the Z boson mass window indicating that at least some fraction of the same-sign electron pairs are produced in Z decays. These events result from decays in which one of the electrons radiates a high E_T photon which subsequently converts in the detector material producing an electron-positron pair. We call this type of event a 'trident' event. If the track associated with the positron from the photon conversion is matched to the corresponding electron cluster, both electrons in the event will

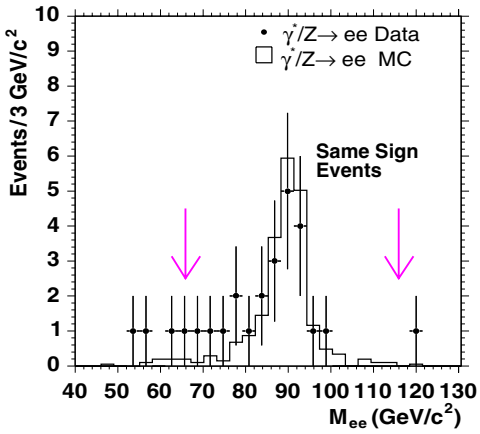

Figure 27. Reconstructed invariant mass of two central electrons in $Z \rightarrow ee$ candidate events in data (points) and simulation (histogram). This distribution is for events in which the electrons are reconstructed with the same charge. The distribution for events with two electrons of opposite sign is shown in figure 18. The number of events in the simulated distributions are normalized so that the number of opposite-sign events in the simulated sample is equal to the number of opposite-sign events in the data. The arrows indicate the location of the invariant mass cuts used to select our candidate samples.

be assigned the same charge. We remove the contribution of real $Z \rightarrow ee$ events from the number of observed same-sign electron pairs by subtracting the observed number of opposite-sign events in the data scaled by the fraction of same-sign to opposite-sign candidates in our simulated samples. The remaining number of same-sign electron pair candidate events is then used to estimate the background contribution from electrons produced in hadronic jets to the opposite-sign candidate sample.

Using this technique, we estimate 20.4 same-sign events from Z decays in the invariant mass window between 66 GeV/c^2 and 116 GeV/c^2. Subtracting this estimate from the total number of observed same-sign events (22), we estimate the contribution from electrons originating from hadronic jets to be $1.6^{+4.7}_{-1.6}$ where the uncertainty is based solely on the statistics of our sample.

The dominant source of systematic uncertainty on the background contribution from events with electrons originating from hadronic jets comes from the simulation detector material model. The probability for an electron to radiate a bremsstrahlung photon prior to entering the calorimeter is strongly dependent on the amount of material in the tracking volume. We study the effect of the material model using the two previously described samples of simulated events generated with $\pm 1.5\%$ of a radiation length of copper added in a cylinder between the silicon and COT tracking detectors. We estimate the systematic uncertainty based on differences in the number of same-sign events observed after subtracting the predicted number of real $Z \rightarrow ee$ events based on the default and modified simulations. The resulting systematic uncertainty on our estimate is 5.2 events which when added in quadrature with the statistical error results in a final background estimate of $1.6^{+7.0}_{-1.6}$.

This technique outlined above can not be used to estimate the background contribution from electrons originating from hadronic jets in $Z \rightarrow ee$ candidates with one central and one plug electron owing to the undetermined charge of the plug candidate. Instead, we estimate the background contamination based on a variation of the previously described method using

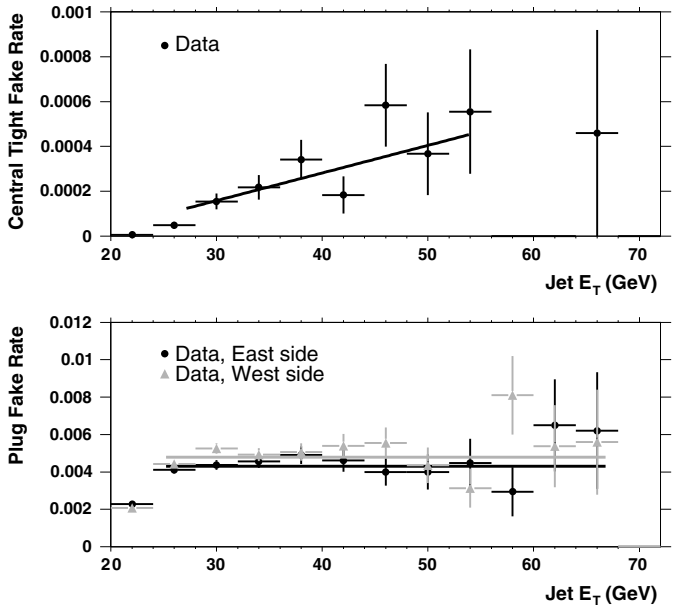

Figure 28. Measured tight central and plug electron jet fake rates as a function of jet E_T.

measured jet fake rates. In order to measure the background contribution to the combined $Z \to ee$ sample from hadronic events producing two fake electrons, we need to measure the jet fake rates for tight central, loose central, and plug electrons. We remove W and Z boson candidates from the inclusive jet sample used to make the fake rate measurements by selecting events with no more than one loose electron and $\not\!\!E_T < 15$ GeV. Based on this inclusive sample, the jet fake rates are defined as the fractions of central jets reconstructed as either tight or loose electrons and plug jets reconstructed as plug electrons. The measured jet fake rates for reconstructed tight central and plug electrons as a function of jet E_T are shown in figure 28.

As previously mentioned, the reconstructed energy of the electrons produced by hadronic jets is smaller than the reconstructed energy of the jets themselves. To account for these differences, we fit the distributions of $E_T^{\text{ele}}/E_T^{\text{jet}}$ to a Gaussian for the jets reconstructed as tight central, loose central, and plug electrons. The means of the fits are used as scaling factors to convert raw jet energies into scaled electron energies, E_T^{scaled}. To obtain the background contribution of events with two electrons originating from hadronic jets to the $Z \to ee$ sample, we apply the measured jet fake rates and energy scalings to a generic multi-jet data sample. Events containing either two central jets with $E_T^{\text{scaled}} > 25$ GeV or one central jet and a plug jet with $E_T^{\text{scaled}} > 20$ GeV are used to extract dijet invariant mass distributions to model the hadronic background for $Z \to ee$. The weights assigned to each event in these distributions is set equal to the product of the jet fake rates for the two jets based on the parameterizations shown in figure 28. The final weighted dijet invariant mass distributions for central–central and central–plug events are shown in figure 29. The resulting distributions are integrated over the invariant mass window of our measurements ($66\ \text{GeV}/c^2 < M_{ee} < 116\ \text{GeV}/c^2$) to obtain an estimate for the number of background events in the $Z \to ee$ candidate sample (after scaling upward by the trigger prescale used to collect events in the generic multi-jet sample).

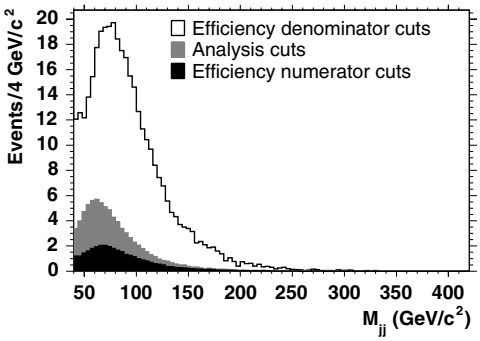

Figure 29. Di-jet invariant mass distributions for central–central and central–plug events in generic multi-jet data. Events are weighted by the product of the measured jet fake rates for each jet. The scaled energies of both jets must pass the electron E_T requirements of our $Z \to ee$ candidate sample (25 GeV for central electrons and 20 GeV for plug electrons).

As illustrated in figure 28, the jet fake rates measured as a function of jet E_T need to be assigned an additional uncertainty based on the assumed shape of the fit. We fit the jet fake rate distributions using several different functional forms and assign an additional systematic uncertainty of 30% based on the resulting spread in background estimates. Based on this technique the measured background contribution of events with two electrons originating from hadronic jets to the $Z \to ee$ candidate sample is 2.4 ± 1.0 central–central and 39 ± 17 central–plug events. The estimated number of central–central events is in good agreement with the result obtained using the observed number of same-sign events in our candidate sample. Using the central–central background estimate based on same-sign events and the central–plug estimate based on the jet fake rate method, we obtain a combined estimate for the background contribution of events with two electrons originating from hadronic jets of 41 ± 18 events.

7.3. Electroweak backgrounds in $W \to \ell\nu$

$Z \to \ell\ell$ events mimic the signature of $W \to \ell\nu$ events in cases where one of the two leptons passes through an uninstrumented region of the detector creating an imbalance in the observed event E_T. The $W \to \ell\nu$ signature can also be reproduced by $W \to \tau\nu$ events in which the τ lepton subsequently decays into an electron or muon. Background contributions from both diboson and $t\bar{t}$ production processes are negligibly small.

The contribution of these electroweak background sources to our $W \to \ell\nu$ candidate samples are obtained from simulation. The $\gamma^*/Z \to \ell\ell$ and $W \to \tau\nu$ simulated event samples are obtained from the equivalent PYTHIA event generation and detector simulation used to produce the signal samples (see section 5). The complete set of $W \to \ell\nu$ selection criteria as described in section 4 are applied to the simulated events in these samples to obtain the fraction of events from each process that satisfy the criteria of our candidate samples. Then, based on Standard Model predictions for the relative production rates of our signal process and the two background processes, we use the estimated acceptances from simulation to obtain the relative contributions of each process to our candidate samples.

The Standard Model predicts equivalent production cross sections for $W \to e\nu$, $W \to \mu\nu$ and $W \to \tau\nu$, while the $Z \to \ell\ell$ production cross sections are related to the corresponding $W \to \ell\nu$ cross sections via the ratio R defined in equation (1). In order to extract the relative contributions of $\gamma^*/Z \to \ell\ell$ events to our $W \to \ell\nu$ candidate samples, an input value for R

Table 34. Estimated $W \to \ell\nu$ backgrounds from other electroweak production processes.

Source	$W \to e\nu$ Background	$W \to \mu\nu$ Background
$Z \to \ell\ell$	426 ± 19	2229 ± 96
$W \to \tau\nu$	749 ± 17	988 ± 24

is required. We choose to use the value $R = 10.67 \pm 0.15$ for W and Z boson production at $\sqrt{s} = 1.96$ TeV obtained from the NNLO theoretical calculation [13–16]. However, to be conservative we inflate the uncertainty on the predicted value for R based on the CDF Run I measured value of $R = 10.90 \pm 0.43$ [26, 27]. The difference in the values of R at $\sqrt{s} = 1.80$ TeV and 1.96 TeV is expected to be negligible. Based on this prediction, the measured value is in good agreement with the theoretical value. To account for the current level of experimental uncertainty, we add an additional 3.9% systematic uncertainty to the NNLO prediction resulting in a value of $R = 10.67 \pm 0.45$.

The relative contributions of $W \to \ell\nu$, $Z \to \ell\ell$, and $W \to \tau\nu$ in our $W \to \ell\nu$ candidate samples are estimated based on the above value for R and the simulated acceptances for each process. The relative acceptances are normalized to the total number of events in each candidate sample after subtracting contributions from non-electroweak backgrounds (events with reconstructed leptons originating from hadronic jets and cosmic rays). The final background estimates for electroweak backgrounds in the $W \to \ell\nu$ candidate samples are summarized in table 34.

7.4. Electroweak backgrounds in $\gamma^*/Z \to \ell\ell$

Several electroweak processes also contribute background events to our $Z \to \ell\ell$ candidate samples. $Z \to \tau\tau$ events mimic the $Z \to \ell\ell$ event signature when both τ leptons decay into or are reconstructed as an electron or muon pair with a reconstructed invariant mass within the mass window of our $Z \to \ell\ell$ measurements. As in the previous section, this background is estimated using a simulated $Z \to \tau\tau$ event sample obtained from the equivalent PYTHIA event generation and detector simulation used to produce the $Z \to \ell\ell$ signal samples. The full set of $Z \to \ell\ell$ selection criteria is applied to the simulated $Z \to \tau\tau$ and $Z \to \ell\ell$ samples to determine the relative acceptances. Based on the Standard Model prediction of equivalent production cross sections for $Z \to ee$, $Z \to \mu\mu$, and $Z \to \tau\tau$, the number of $Z \to \tau\tau$ background events in each candidate sample is extracted using the relative acceptances from the total number of events after removing non-electroweak background contributions.

A comparison of the reconstructed invariant mass distributions for simulated $\gamma^*/Z \to ee$ and $\gamma^*/Z \to \tau\tau$ events passing the $Z \to ee$ selection criteria is shown in figure 30. The majority of $\gamma^*/Z \to \tau\tau$ events are observed to have a reconstructed invariant mass below the mass window used in our measurements. As a result, the contribution of this background source to our candidate samples is small, 3.7 ± 0.4 events in the $Z \to ee$ sample and 1.5 ± 0.3 events in the $Z \to \mu\mu$ sample. An identical approach is used to estimate $Z \to \ell\ell$ background contributions from both top quark and diboson production. The estimated background contributions from each of these sources is found in all cases to be less than one event and therefore considered to be negligible.

An additional source of background events to the $Z \to ee$ candidate sample is $W \to e\nu$ events with an associated hadronic jet that results in a second reconstructed electron within the event. We use our simulated $W \to e\nu$ sample to estimate the background contribution from this source by applying previously determined jet fake rates for the hadronic jets in these

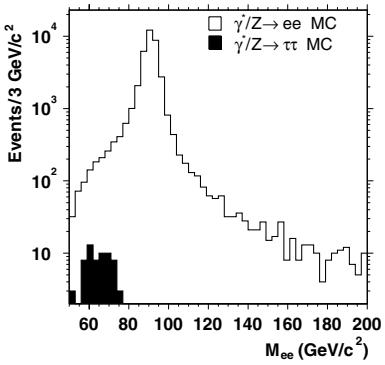

Figure 30. Reconstructed invariant mass distribution for simulated $\gamma^*/Z \rightarrow ee$ (open histogram) and $\gamma^*/Z \rightarrow \tau\tau$ (solid histogram) events satisfying the $Z \rightarrow ee$ candidate sample selection criteria.

events with scaled E_T above the corresponding electron thresholds. The relative acceptance of simulated $W \rightarrow e\nu$ events, weighted by the measured jet fake rates, and $Z \rightarrow ee$ signal events are used to extract the number of background events from this process based on the value for R presented in the previous section. Once again, the relative acceptances are applied to the final candidate sample after subtracting the estimated number of background events from non-electroweak sources. The estimated number of $W \rightarrow e\nu$ background events in the $Z \rightarrow ee$ sample is 16.8 ± 2.8 events.

7.5. Cosmic ray backgrounds in $W \rightarrow \mu\nu$

Energetic cosmic ray muons traverse the detector at a significant rate, depositing hits in both muon and COT chambers, and in some cases can mimic the signatures of our $W \rightarrow \mu\nu$ and $Z \rightarrow \mu\mu$ candidate events. A cosmic ray muon passing through the detector is typically reconstructed as a pair of incoming and outgoing legs relative to the beam line of the detector. The reconstructed muon legs tend to be isolated and pass our muon selection criteria. In some cases, one of the two cosmic legs is not reconstructed due to fiducial and/or timing constraints. These events typically satisfy both the Z-rejection and $\not\!\!E_T$ criteria of our $W \rightarrow \mu\nu$ candidate sample due to the lack of an additional track and the resulting transverse momentum imbalance.

We remove cosmic ray events from our $W \rightarrow \mu\nu$ candidate sample using a tagging algorithm based on the timing information associated with hits in the COT. The algorithm uses a multi-parameter fit over the full set of hits left by the incoming and outgoing cosmic legs. The leg belonging to the reconstructed muon serves as the seed track for the fit. The other leg is referred to as the opposite-side track. The algorithm performs the following steps to determine if an event is consistent with the cosmic ray hypothesis.

- Hits belonging to the seed track are refitted with the five helix parameters and a floating global time shift, t_0.
- Based on the best fit values, an incoming or outgoing hypothesis is assigned to the seed track.
- The refitted seed track is used to search for the hits belonging to the second cosmic leg on the opposite side of the COT.
- If enough hits are found on the other side of the COT, a similar fit procedure is performed to identify the opposite-side track.

- If both legs are found, a simultaneous fit is performed to combine all hits from the seed and opposite-side legs into a single helix.

The final decision of the cosmic tagger depends on the quality of the simultaneous fit to the hits on both legs. If one leg is recognized as incoming and fits well to an outgoing leg on the other side of the detector, the event is tagged as a cosmic ray. As described in greater detail below, we observe that our tagging algorithm identifies most of the cosmic background events in our candidate sample. We also find that the algorithm tags very few real events as cosmic rays (see section 6).

After removing tagged events from our $W \to \mu\nu$ sample, we need to estimate the remaining background from cosmic rays. This estimate is made by searching for hits in the muon chambers on the opposite side of the reconstructed muon track in our final candidate events. These hits are present for a large fraction of cosmic ray muons even in cases where the second leg is not identified by our algorithm. Since the muon chamber hits are not used in the tagging algorithm, their presence is unbiased with respect to its decision. The $\Delta\phi$ distribution for matched hits produced by cosmic ray muons with respect to the direction of the muon candidate track is sharply peaked in the region around 180°. These events sit on top of a flat event background in $\Delta\phi$ originating from random coincidences between the muon track and unrelated matched hits in the muon chambers. The contribution of cosmic ray events to the candidate $\Delta\phi$ distribution is determined by counting the number of events with matched muon chamber hits in a 10° window centered on $\Delta\phi = 180^\circ$ and subtracting a fitted contribution from the flat background. Using this approach, we would estimate a cosmic background contribution of 54.7 ± 5.0 events in our 31,722 event $W \to \mu\nu$ candidate sample.

Some of the cosmic ray background events in our candidate sample, however, do not have opposite-side muon chamber hits due to gaps in the muon detector coverage. In order to estimate the total cosmic ray background in our candidate sample from the observed number of events with matched opposite-side hits, we apply an acceptance correction based on the fraction of $W \to \mu\nu$ candidate events in which the reconstructed muon track points at an active region of muon chambers when extrapolated to the opposite side of the detector. We extrapolate the 31,722 muon tracks in our $W \to \mu\nu$ candidate events to the opposite side of the detector and find that $58 \pm 30\%$ point at active regions of the muon chambers. Our acceptance correction assumes that the spacial distribution of muons originating from cosmic rays is similar to that of our $W \to \mu\nu$ candidate sample. We assign a large systematic uncertainty on the measured acceptance to account for the non-uniform spacial distribution (most enter from the top side of the detector) of cosmic rays and the reconstruction biases associated with their entry locations and angles of incidence on the detector.

To complete the cosmic background measurement for our $W \to \mu\nu$ candidate sample, we also need to estimate the contribution of $Z \to \mu\mu$ events to the observed excess of events in the window around $\Delta\phi = 180^\circ$. $Z \to \mu\mu$ events that contain a second reconstructed track passing a loose set of minimum ionizing cuts are rejected from our candidate sample via the Z-rejection selection criteria. However, a small fraction of muon tracks from $Z \to \mu\mu$ events are embedded in jets and fail the loose minimum ionizing cuts or in other cases are simply not reconstructed. Since the muons in $Z \to \mu\mu$ decays are typically produced in roughly opposite directions to one another, the non-identified tracks in these events can also produce muon chamber hits on the opposite side of the one reconstructed muon in these events. This background is estimated from our simulated $Z \to \mu\mu$ event sample. Based on this sample, we estimate the number of $Z \to \mu\mu$ background events in our $W \to \mu\nu$ candidate sample with matched muon chamber hits in the 10° window centered on $\Delta\phi = 180^\circ$ to be 35.4 ± 9.1. The uncertainty assigned to this background is based on our use of different techniques for looking at opposite side muon chamber hits in data and simulation.

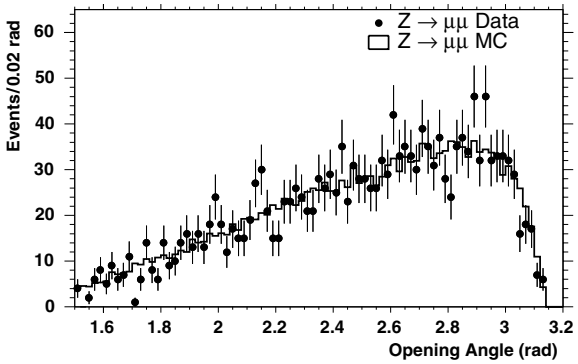

Figure 31. Comparison of the three-dimensional opening angle distribution for muon tracks in $Z \rightarrow \mu\mu$ candidate events with the same distribution from simulated events. The simulated distribution is scaled to match the data in the region below 2.8 radians.

The final estimate of the cosmic ray background in the $W \rightarrow \mu\nu$ sample, $N_{\rm bg}^{\rm cos}$, is obtained from

$$N_{\rm bg}^{\rm cos} = \frac{N_{\rm evt}^{\rm MH} - N_{Z\rightarrow\mu\mu}^{\rm MH}}{A_{\mu}^{\rm opp}}, \tag{29}$$

where $N_{\rm evt}^{\rm MH}$ is the number of $W \rightarrow \mu\nu$ candidate events with matched hits in the tight window centered on $\Delta\phi = 180^{\circ}$, $N_{Z\rightarrow\mu\mu}^{\rm MH}$ is the predicted number of $Z \rightarrow \mu\mu$ background events with matched hits in the same window, and $A_{\mu}^{\rm opp}$ is muon chamber acceptance for muon tracks in $W \rightarrow \mu\nu$ candidate events extrapolated to the opposite side of the detector. Using the input values obtained above, we estimate a total cosmic background of 33.1 ± 22.9 events for our $W \rightarrow \mu\nu$ candidate sample.

7.6. Cosmic ray backgrounds in $Z \rightarrow \mu\mu$

Cosmic rays also contribute to the $Z \rightarrow \mu\mu$ candidate sample. The majority of these events are removed using the cosmic ray tagging algorithm described in the previous section. The remaining cosmic ray background is estimated based on the distribution of the three-dimensional opening angle between the muon tracks in candidate events. The two reconstructed muon legs in the cosmic ray background events are typically back-to-back with opening angles at or near 180°. The residual background is estimated by fitting the opening angle distribution for data events in the region below 2.8 radians (assumed to be background free) to the same distribution for simulated $Z \rightarrow \mu\mu$ events. The output of the fit is a scale factor for the distribution from simulation which is also applied in the region above 2.8 radians. The number of scaled simulation events with an opening angle greater than 2.8 radians is compared to the number of data candidate events in the same region. The observed excess in data over simulation is taken as our estimate of the cosmic ray background. Using this technique, we estimate a total of 12 ± 12 cosmic ray background events in our $Z \rightarrow \mu\mu$ candidate sample where the quoted uncertainties are based on the statistics of our data sample. A comparison of the opening angle distribution between data and scaled simulation is shown in figure 31.

Table 35. Summary of background event estimates for the $W \to \ell\nu$ and $Z \to \ell\ell$ candidate samples.

Background source	$W \to e\nu$	$W \to \mu\nu$	$Z \to ee$	$Z \to \mu\mu$
Multi-jet	587 ± 299	220 ± 112	41 ± 18	0^{+1}_{-0}
$Z \to \ell\ell$	426 ± 19	2229 ± 96	–	–
$Z \to \tau\tau$	negl.	negl.	3.7 ± 0.4	1.5 ± 0.3
$W \to \tau\nu$	749 ± 17	988 ± 24	negl.	negl.
$W \to \ell\nu$	–	–	16.8 ± 2.8	negl.
Cosmic rays	negl.	33 ± 23	negl.	12 ± 12
Total	1762 ± 300	3469 ± 151	62 ± 18	13 ± 13

7.7. Background summary

Based on the information presented in the preceding sections, the estimated background contributions to the $W \to e\nu$, $W \to \mu\nu$, $Z \to ee$ and $Z \to \mu\mu$ candidate samples are summarized in table 35.

8. Results

Using the measured event counts, kinematic and geometric acceptances, event selection efficiencies, background estimates, and integrated luminosities for our candidate samples, we extract the W and γ^*/Z boson production cross sections multiplied by the leptonic (e and μ) branching ratios. We also determine a value for the ratio of $W \to \ell\nu$ to $Z \to \ell\ell$ cross sections, R, taking advantage of correlated uncertainties in the two cross-section measurements which cancel in the ratio. To test for lepton universality, we use the measured ratio of $W \to \ell\nu$ cross sections in the muon and electron channels to extract a ratio of the $W \to \ell\nu$ coupling constants, g_μ/g_e. Then, based on the assumption of lepton universality, we increase the precision of our results by combining the production cross section and cross-section ratio measurements obtained from the electron and muon candidate samples. The resulting combined value of R is used to extract the total decay width of the W boson, $\Gamma(W)$, and the W leptonic branching ratio, $\text{Br}(W \to \ell\nu)$, which are compared with Standard Model predictions. The measurement of $\Gamma(W)$ is also used to constrain the CKM matrix element V_{cs}.

8.1. $W \to \ell\nu$ cross section

The cross section $\sigma(p\overline{p} \to W)$ times the branching ratio $\text{Br}(W \to \ell\nu)$ is calculated using equation (5) given in section 1. The measurements of the required input parameters for the electron and muon candidate samples are described in the previous sections and summarized in table 36. Based on these values, we obtain

$$\sigma_W \cdot \text{Br}(W \to e\nu) = 2.771 \pm 0.014(\text{stat.}) \pm^{0.062}_{0.056} (\text{syst.}) \pm 0.166\,(\text{lum.})\text{nb} \tag{30}$$

and

$$\sigma_W \cdot \text{Br}(W \to \mu\nu) = 2.722 \pm 0.015\,(\text{stat.}) \pm^{0.066}_{0.061} (\text{syst.}) \pm 0.163\,(\text{lum.})\text{nb}. \tag{31}$$

We compare our measurements to a recent NNLO total cross-section calculation for $\sqrt{s} = 1.96$ TeV [66] which utilizes the MRST 2002 NNLL PDF set [66, 67]. The resulting predicted $W \to \ell\nu$ cross section is 2.687 ± 0.054 nb, which agrees well with our measured values in both lepton channels. The uncertainty on the predicted cross section is mostly due to PDF model uncertainties derived from the MRST error PDF sets. We also perform an independent

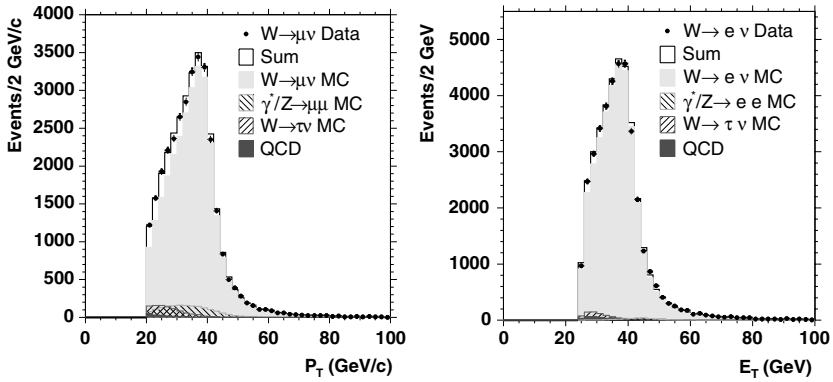

Figure 32. Muon p_T (left) and electron E_T (right) distributions for $W \to \ell\nu$ candidate events in data (points). The solid lines are the sum of the predicted shapes originating from the signal and background processes weighted by their estimated contributions to our candidate samples. The separate contributions originating from the signal and each individual background process are also shown.

Table 36. Summary of the input parameters to the $W \to \ell\nu$ cross-section calculations for the electron and muon candidate samples.

	$W \to e\nu$	$W \to \mu\nu$
$N_W^{\rm obs}$	37584	31722
$N_W^{\rm bck}$	1762 ± 300	3469 ± 151
A_W	$0.2397\ ^{+0.0035}_{-0.0042}$	$0.1970\ ^{+0.0024}_{-0.0031}$
ϵ_W	0.749 ± 0.009	0.732 ± 0.013
$\int \mathcal{L}\,dt$ (pb^{-1})	72.0 ± 4.3	72.0 ± 4.3

calculation of the uncertainty on the total $W \to \ell\nu$ cross section originating from uncertainties in the PDF model using the method described in section 5. Based on this method, we obtain a consistent 1.3% uncertainty based on the MRST error PDF sets and a 3.9% uncertainty based on the CTEQ6 error PDF sets.

Distributions of electron E_T, muon p_T, event $\not\!\!E_T$, and W transverse mass ($M_T = \sqrt{2[E_T \not\!\!E_T - (E_x \not\!\!E_{T,x} + E_y \not\!\!E_{T,y})]}$) for events in our $W \to \ell\nu$ candidate samples are shown in figures 32–34. The data distributions are compared against a sum of the predicted shapes of these distributions for the $W \to \ell\nu$ signal and each contributing background process ($Z \to \ell\ell$, $W \to \tau\nu$, and hadronic jets). The predicted shapes are obtained from our simulated event samples except in the case of the background arising from hadronic jets, which is modeled using events in the data containing non-isolated leptons that otherwise satisfy the $W \to \ell\nu$ selection criteria. In the sum, the predicted shape obtained for each process is weighted by the estimated number of events in our $W \to \ell\nu$ candidate samples originating from that process (see table 35). In the case of the $\not\!\!E_T$ distribution, we remove the selection cut on the $\not\!\!E_T$ variable to include events with low $\not\!\!E_T$ in the comparison and highlight the significant background contribution from hadronic jets in this region.

8.2. $\gamma^*/Z \to \ell\ell$ cross section

Similarly, the cross section $\sigma(p\overline{p} \to \gamma^*/Z)$ times the branching ratio $\mathrm{Br}(\gamma^*/Z \to \ell\ell)$ is calculated using equation (6) given in section 1. The measurements of the required input

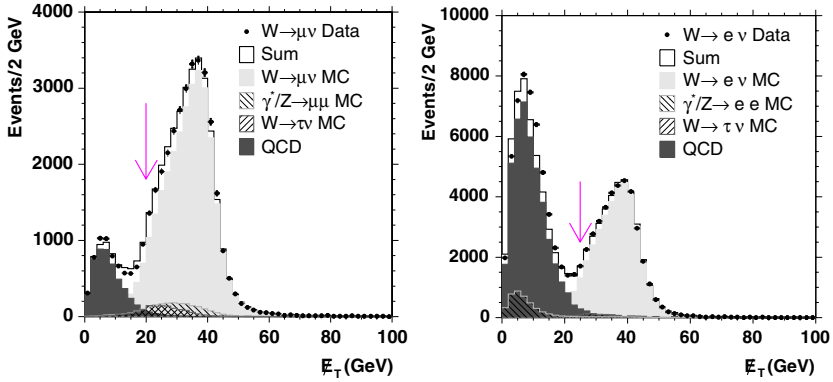

Figure 33. Event $\not\!\!E_T$ distributions for $W \to \ell\nu$ candidate events in data (points). The selection requirement on event $\not\!\!E_T$ has been removed to include candidate events with low $\not\!\!E_T$. The solid lines are the sum of the predicted shapes originating from the signal and background processes weighted by their estimated contributions to our candidate samples. The separate contributions originating from the signal and each individual background process are also shown. The arrows indicate the location of the event $\not\!\!E_T$ selection criteria used to define our candidate samples.

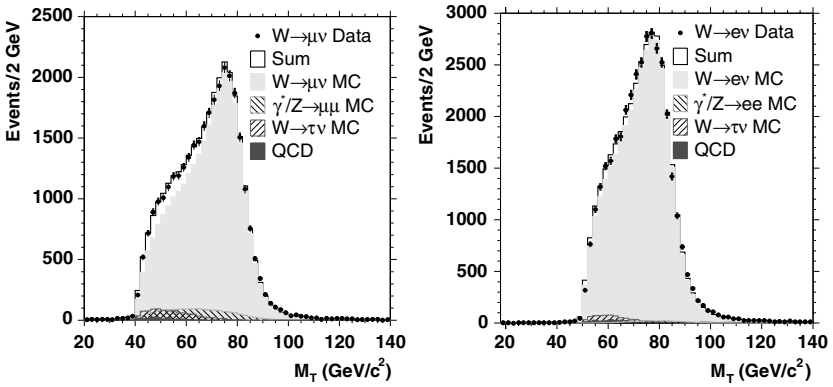

Figure 34. Transverse mass (M_T) distributions for $W \to \ell\nu$ candidate events in data (points). The solid lines are the sum of the predicted shapes originating from the signal and background processes weighted by their estimated contributions to our candidate samples. The separate contributions originating from the signal and each individual background process are also shown.

parameters for the electron and muon candidate samples are described in the previous sections and summarized in table 37. Based on these values, we obtain

$$\sigma_{\gamma^*/Z} \cdot \text{Br}(\gamma^*/Z \to ee) = 255.8 \pm 3.9\,(\text{stat.}) \pm^{5.5}_{5.4}\,(\text{syst.}) \pm 15.3\,(\text{lum.})\text{pb} \tag{32}$$

and

$$\sigma_{\gamma^*/Z} \cdot \text{Br}(\gamma^*/Z \to \mu\mu) = 248.0 \pm 5.9\,(\text{stat.}) \pm^{8.0}_{7.2}\,(\text{syst.}) \pm 14.8\,(\text{lum.})\text{pb}\,. \tag{33}$$

These measurements are the cross sections for dileptons produced in the mass range 66 GeV/c^2 $< M_{\ell\ell} <$ 116 GeV/c^2 where both γ^* and Z boson exchange contribute. A correction factor of $F = 1.004 \pm 0.001$ determined from a NNLO $\text{d}\sigma/\text{d}y$ calculation, PHOZPR [14–16], using MRST 2002 NNLL PDFs [67], is needed to convert these measured cross

Table 37. Summary of the input parameters to the $\gamma^*/Z \to \ell\ell$ cross-section calculations for the electron and muon candidate samples.

	$\gamma^*/Z \to ee$	$\gamma^*/Z \to \mu\mu$
N_Z^{obs}	4242	1785
N_Z^{bck}	62 ± 18	13 ± 13
A_Z	$0.3182\ ^{+0.0039}_{-0.0041}$	$0.1392\ ^{+0.0027}_{-0.0033}$
ϵ_Z	0.713 ± 0.012	0.713 ± 0.015
$\int \mathcal{L}\,dt$ (pb^{-1})	72.0 ± 4.3	72.0 ± 4.3

sections into those for pure Z boson exchange over the entire dilepton mass range; the measured cross sections need to be multiplied by F. We compare the corrected cross sections for pure Z boson exchange to the recent NNLO total cross-section calculations for $\sqrt{s} = 1.96$ TeV [66]. The $Z \to \ell\ell$ production cross section predicted by these calculations is 251.3 ± 5.0 pb, which is in good agreement with the corrected, measured values obtained in both lepton channels. The uncertainty on the predicted Z boson production cross section is also primarily due to uncertainties in the PDF model derived from the MRST error PDF sets. Our independent estimates for these uncertainties using the method described in section 5 are a consistent 1.2% uncertainty based on the MRST error PDF sets and a somewhat larger 3.7% uncertainty based on the CTEQ6 error PDF sets.

Figures 17 and 18 show the invariant mass distributions for events in our $Z \to \ell\ell$ candidate samples. The data distributions are compared against predicted shapes from our simulated $Z \to \ell\ell$ event samples. The predicted shapes are normalized to the total number of events in the candidate samples. In making these comparisons, we ignore background processes which account for less than 1% of the events in these samples (see table 35).

8.3. Ratio of $W \to \ell\nu$ to $Z \to \ell\ell$

Precision measurements of the ratio of $W \to \ell\nu$ to $Z \to \ell\ell$ production cross sections, R, are used to test the Standard Model. The Standard Model parameters $\Gamma(W)$ and $\text{Br}(W \to \ell\nu)$ can be extracted from our measured values of this ratio and are sensitive to non-Standard Model processes that result in additional decay modes for the W boson. A new high-mass resonance which decays to either W or Z bosons could also have a direct effect on the measured value for R.

The ratio of cross sections can be expressed in terms of measured quantities:

$$R = \frac{1}{F} \cdot \frac{N_W^{\text{obs}} - N_W^{\text{bck}}}{N_Z^{\text{obs}} - N_Z^{\text{bck}}} \cdot \frac{A_Z}{A_W} \cdot \frac{\epsilon_Z}{\epsilon_W}, \tag{34}$$

where F is the correction factor for converting the measured $\gamma^*/Z \to \ell\ell$ cross section into the cross section for pure Z boson exchange and the other parameters are as defined for the W and Z production cross-section measurements. The integrated luminosity terms in the W and Z cross-section calculations along with their associated uncertainties cancel completely in the R calculation, allowing for a significantly more precise measurement of the ratio than is possible for the individual cross sections. In addition, we take advantage of many correlated uncertainties in the event selection efficiencies and kinematic and geometric acceptances of our W and Z candidate samples which cancel in the ratios A_Z/A_W and ϵ_Z/ϵ_W. For example, uncertainties on the acceptances arising from the PDF model are significantly smaller for the ratio of the $Z \to \ell\ell$ and $W \to \ell\nu$ acceptances than for either individual acceptance. The calculation of A_Z/A_W and ϵ_Z/ϵ_W for our electron and muon candidate samples and the treatment of the correlated uncertainties in these ratios are discussed in sections 5 and 6. The

Table 38. Summary of the input parameters to the R calculations for the electron and muon candidate samples.

	R_e	R_μ
N_W^{obs}	37584	31722
N_W^{bck}	1762 ± 300	3469 ± 151
N_Z^{obs}	4242	1785
N_Z^{bck}	62 ± 18	13 ± 13
$\frac{A_Z}{A_W}$	1.3272 ± 0.0109	0.7066 ± 0.0068
$\frac{\epsilon_Z}{\epsilon_W}$	0.952 ± 0.011	0.974 ± 0.010
F	1.004 ± 0.001	1.004 ± 0.001

event counts and background estimates for the $W \to \ell\nu$ and $Z \to \ell\ell$ candidate samples are the same as those used in the individual cross-section calculations. Table 38 summarizes the input parameters used to calculate R using the electron and muon candidate samples. Substituting these values into equation (34), we obtain

$$R_e = 10.79 \pm 0.17\,(\text{stat.}) \pm 0.16\,(\text{syst.}) \tag{35}$$

and

$$R_\mu = 10.93 \pm 0.27\,(\text{stat.}) \pm 0.18\,(\text{syst.})\,. \tag{36}$$

Based on the calculations of the production cross sections for $W \to \ell\nu$ and $Z \to \ell\ell$ provided by [12–16], the expected value for R at $\sqrt{s} = 1.96$ TeV is 10.69. To obtain an accurate estimate for the uncertainty on this prediction, we need to account for correlated uncertainties in the individual cross-section predictions. The error originating from PDF model uncertainties has the largest contribution to the total uncertainty. We estimate the magnitude of this contribution using the previously defined method in section 5 and obtain a 0.45% uncertainty based on the MRST error PDF sets and a larger 0.56% uncertainty based on the CTEQ6 error PDF sets. We also need to account for the effect of additional uncertainties in the values of the electroweak parameters and CKM matrix elements used in the cross-section calculations. We estimate these uncertainties using the $\overline{MS}$ NNLO total cross-section calculation, ZWPROD [14, 15]. We have updated the calculation code to incorporate the CTEQ and MRST PDFs and variations of the electroweak parameters and CKM matrix elements. We obtain an uncertainty of 0.15% for the σ_Z calculation and 0.40% for the σ_W calculation. The larger uncertainty associated with the σ_W calculation is due primarily to experimental uncertainties on the CKM matrix values. To be conservative, we add the larger PDF model uncertainty (0.56%) in quadrature with the individual cross-section calculation uncertainties (0.15% and 0.40%) to obtain a combined uncertainty on the prediction for R of 0.70%. The resulting prediction, 10.69 ± 0.08, agrees with the measured values of R in both lepton channels.

8.4. μ-e universality in W decays

Stringent tests of lepton universality at LEP provide strong evidence for lepton universality in $Z \to \ell\ell$ production. We make a similar test for lepton universality in $W \to \ell\nu$ production by extracting the ratio of $W \to \ell\nu$ couplings, g_μ/g_e, from the measured ratio of the $W \to \mu\nu$ and $W \to e\nu$ cross sections. The $W \to \ell\nu$ couplings are related to the measured ratio U of the cross sections, defined as

$$U \equiv \frac{\sigma_W \cdot \text{Br}(W \to \mu\nu)}{\sigma_W \cdot \text{Br}(W \to e\nu)} = \frac{\Gamma(W \to \mu\nu)}{\Gamma(W \to e\nu)} = \frac{g_\mu^2}{g_e^2}\,. \tag{37}$$

Table 39. Uncertainties on the measured ratio of $W \to \mu\nu$ and $W \to e\nu$ cross sections, U.

Category	Uncertainty
Statistical uncertainty	0.0075
Acceptance ratio:	
Simulation statistics	0.0019
Boson p_T model	0.0001
PDF model	$^{+0.0003}_{-0.0004}$
p_T Scale and resolution	0.0018
E_T Scale and resolution	0.0034
Material model	0.0072
Recoil energy model	0.0010
Efficiency ratio:	
Uncorrelated	0.0199
Backgrounds:	
Hadronic	0.0043
Electroweak	0.0030
Cosmic ray	0.0008

As in the case of the R measurements described in the previous section, many of the uncertainties associated with the individual cross-section measurements cancel in the ratio. Table 39 summarizes the uncorrelated uncertainties between the two cross-section measurements that contribute to the overall uncertainty on g_μ/g_e. The uncertainties due to the PDF model cancel almost completely in the ratio. The major remaining contributions to the systematic uncertainty come from the uncorrelated event selection efficiencies for the electron and muon candidate samples. Since these efficiencies are measured directly from $Z \to \ell\ell$ candidate events in the data, the associated uncertainties will decrease as additional data are analyzed. In this sense, the remaining uncertainty on g_μ/g_e is primarily statistical in nature and can be reduced with larger data samples. Using the input parameters to our $W \to \ell\nu$ cross-section measurements, we obtain

$$\frac{g_\mu}{g_e} = 0.991 \pm 0.012. \tag{38}$$

Using equation (37) and the current world average of experimental results for $\mathrm{Br}(W \to \mu\nu) = 0.1057 \pm 0.0022$ and $\mathrm{Br}(W \to e\nu) = 0.1072 \pm 0.0016$ [20], the expected value of g_μ/g_e is 0.993 ± 0.013 which is in good agreement with our measured value.

8.5. Combined results from the electron and muon channels

Since our measurement of g_μ/g_e supports the conclusion of lepton universality in $W \to \ell\nu$ production, we proceed to combine our measurements of the $W \to \ell\nu$ and $Z \to \ell\ell$ production cross-section measurements in the electron and muon channels to increase the overall precision of these results. We also combine our measurements of R_e and R_μ to determine a precision value for R which is used to test the Standard Model.

8.5.1. Combination of the cross sections. We use the best linear unbiased estimate (BLUE) [70, 71] method to combine measurements in the electron and muon channels. For the $W \to \ell\nu$ measurements, we identify twenty categories of uncertainties, several of which are correlated in the electron and muon channels. Table 40 lists these categories and summarizes the raw contribution of each (in pb) to the W cross-section measurements in the electron and

Table 40. Uncertainty categories for the inclusive W cross-section measurements. These values are absolute contributions to σ_W in pb. The uncertainties in the electron and muon channels for each category are treated as either 100% correlated (1.0) or uncorrelated (0.0).

Category	Electron	Muon	Correlation
Statistical uncertainty	14.3	15.3	0.0
Acceptance:			
Simulation statistics	3.6	3.9	0.0
Boson p_T model	1.2	1.0	1.0
PDF model	36.9	35.4	1.0
p_T Scale and resolution	0.8	5.6	1.0
E_T Scale and resolution	9.5	0.0	0.0
Material model	20.2	0.0	0.0
Recoil energy model	6.8	9.4	1.0
Efficiencies:			
Vertex z_0 cut	11.7	11.5	1.0
Track reconstruction	11.1	10.9	1.0
Trigger	2.9	32.7	0.0
Lepton reconstruction	11.1	19.7	0.0
Lepton identification	24.1	23.8	0.0
Lepton isolation	9.4	9.7	0.0
Z-rejection cut	0.0	4.6	0.0
Cosmic ray algorithm	0.0	0.3	0.0
Backgrounds:			
Hadronic	23.1	10.8	1.0
$Z \to \ell\ell$	1.5	9.2	1.0
$W \to \tau\nu$	1.3	2.3	1.0
Cosmic ray	0.0	2.2	0.0

muon channels. Based on the information in this table, we combine the measurements in the two lepton channels and obtain

$$\sigma_W \cdot \text{Br}(W \to \ell\nu) = 2.749 \pm 0.010\,(\text{stat.}) \pm 0.053\,(\text{syst.}) \pm 0.165\,(\text{lum.})\,\text{nb}, \tag{39}$$

which has a precision of 2.0%, not including the uncertainty associated with the measured integrated luminosity of our samples. The uncertainty on luminosity is not included in the calculation of the combined value.

The combination of the $Z \to \ell\ell$ cross-section measurements in the electron and muon channels is based on the same procedure. In this case, we identify seventeen categories of uncertainties, some of which are correlated between channels. Table 41 provides a list of these categories and summarizes the raw contribution of each (in pb) to the Z cross-section measurements in the electron and muon channels. The additional acceptance for forward electrons in the plug calorimeter modules reduces the statistical uncertainty associated with the Z cross-section measurement in the electron channel, which thus has a larger weight in the final combination. The combined result is

$$\sigma_{\gamma^*/Z} \cdot \text{Br}(\gamma^*/Z \to \ell\ell) = 254.9 \pm 3.3\,(\text{stat.}) \pm 4.6\,(\text{syst.}) \pm 15.2\,(\text{lum.})\,\text{pb}, \tag{40}$$

which has a precision of 2.2%, not including the uncertainty associated with the measured integrated luminosity of our samples. As discussed previously, the combined cross section given here is the cross section for dileptons in the mass range $66\,\text{GeV}/c^2 < M_{\ell\ell} < 116\,\text{GeV}/c^2$ including contributions from both γ^* and Z boson exchange. In order to convert the measured cross section into a cross section for pure Z boson exchange over the entire mass range, one

Table 41. Uncertainty categories for the inclusive Z cross-section measurements. These values are absolute contributions to σ_Z in pb. The uncertainties in the electron and muon channels for each category are treated as either 100% correlated (1.0) or uncorrelated (0.0).

Category	Electron	Muon	Correlation
Statistical uncertainty	3.93	5.87	0.0
Acceptance:			
Simulation statistics	0.61	1.01	0.0
Boson p_T model	0.16	0.19	1.0
PDF model	1.96	4.94	1.0
p_T Scale and resolution	0.10	0.13	1.0
E_T Scale and resolution	0.67	0.00	0.0
Material model	2.45	0.00	0.0
Recoil energy model	0.00	0.00	0.0
Efficiency:			
Vertex z_0 cut	1.08	1.04	1.0
Track reconstruction	1.42	1.98	1.0
Trigger	0.17	2.05	0.0
Lepton reconstruction	1.43	1.24	0.0
Lepton identification	3.39	3.48	0.0
Lepton isolation	1.21	1.77	0.0
Cosmic ray algorithm	0.00	0.15	0.0
Backgrounds:			
Hadronic	1.10	0.08	1.0
$Z \to \tau\tau$	0.02	0.04	1.0
$W \to \ell\nu$	0.17	0.00	1.0
Cosmic Ray	0.00	1.76	0.0

must multiply the measured value by the correction factor presented earlier, $F = 1.004 \pm 0.001$.

A comparison of the predictions from [12–16] for $\sigma_W \cdot \mathrm{Br}(W \to \ell\nu)$ and $\sigma_Z \cdot \mathrm{Br}(Z \to \ell\ell)$ as a function of the $p\overline{p}$ center-of-mass energy, E_{CM}, with our measured values and other experimental results [25, 32, 72] are shown in figure 35.

8.5.2. Combination of the R measurements. The same BLUE method is also used to combine our measurements of R_e and R_μ. For our cross-section ratio measurements we identify fifteen categories of uncertainties, some of which are correlated between our measurements in the electron and muon channels. Table 42 lists these categories and summarizes the raw contribution of each to the R_e and R_μ measurements. Since most of the uncertainties related to efficiency factors are uncorrelated in the electron and muon channels, the corresponding uncertainties are combined into a single net uncertainty for uncorrelated efficiencies. The exception is the uncertainty on COT track reconstruction efficiency which is 100% correlated between the two channels. The combined result is

$$R = 10.84 \pm 0.15\,(\mathrm{stat.}) \pm 0.14\,(\mathrm{syst.}) \tag{41}$$

which is precise to 1.9%.

8.6. Extraction of standard model parameters

As previously discussed, the precision value for R obtained from the combination of our measurements in the electron and muon channels can be used to measure various Standard

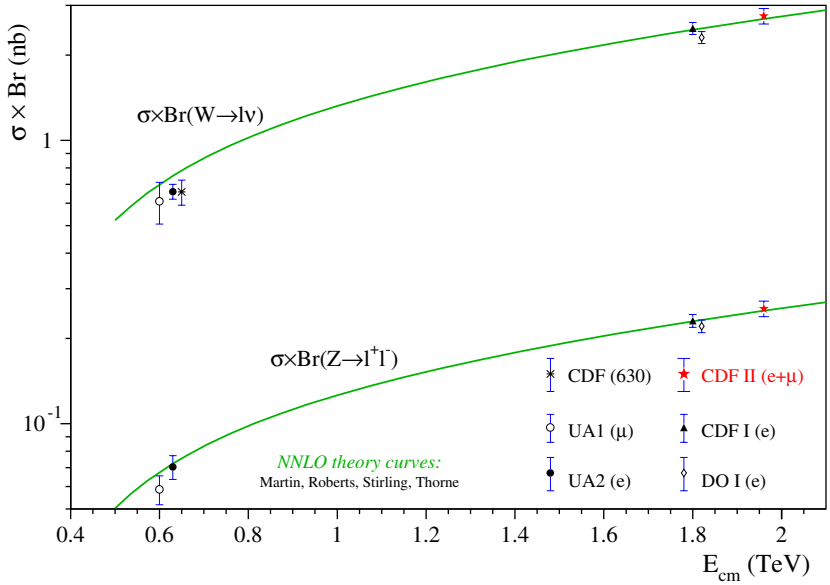

Figure 35. $W \to \ell\nu$ and $Z \to \ell\ell$ cross-section measurements as a function of the $p\overline{p}$ center-of-mass energy, E_{CM}. The solid lines correspond to the theoretical NNLO Standard Model calculations from [12–16].

Table 42. Uncertainty categories for the R measurements. The uncertainties in the electron and muon channels for each category are treated as either 100% correlated (1.0) or uncorrelated (0.0).

Category	Electron	Muon	Correlation
Statistical uncertainty	0.1748	0.2659	0.0
Acceptance ratio:			
Simulation statistics	0.0293	0.0472	0.0
Boson p_T model	0.0020	0.0044	1.0
PDF Model	0.0701	0.0836	1.0
p_T Scale and resolution	0.0012	0.0167	1.0
E_T Scale and resolution	0.0184	0.0000	0.0
Material model	0.0322	0.0000	0.0
Recoil energy model	0.0267	0.0377	1.0
Efficiency ratio:			
Uncorrelated	0.1204	0.0999	0.0
Track reconstruction	0.0169	0.0437	1.0
Backgrounds:			
Hadronic	0.0437	0.0399	1.0
Uncorrelated electroweak	0.0089	0.0094	0.0
Correlated electroweak	0.0057	0.0369	1.0
Cosmic ray	0.0000	0.0689	0.0
Correction factor, F	0.0107	0.0109	1.0

Model parameters and in the process test the predictions of the model. The ratio of cross sections can be expressed as

$$R = \frac{\sigma(p\overline{p} \to W)}{\sigma(p\overline{p} \to Z)} \frac{\Gamma(W \to \ell\nu)}{\Gamma(Z \to \ell\ell)} \frac{\Gamma(Z)}{\Gamma(W)}. \tag{42}$$

Using the precision LEP measurements for $\Gamma(Z \to \ell\ell)/\Gamma(Z)$ at the Z pole mass and the NNLO calculation of $\sigma(p\overline{p} \to W)/\sigma(p\overline{p} \to Z)$ by [12–16], we extract the Standard Model parameter $\mathrm{Br}(W \to \ell\nu) = \Gamma(W \to \ell\nu)/\Gamma(W)$ from equation (42) using our measured value of R. Using the Standard Model prediction for $\Gamma(W \to \ell\nu)$, we also make an indirect measurement of $\Gamma(W)$ and based on this value place a constraint on the CKM matrix element V_{cs}.

8.6.1. Extraction of $\mathrm{Br}(W \to \ell\nu)$. The required parameters to extract $\mathrm{Br}(W \to \ell\nu)$ from our measured R value using equation (42) are the predicted ratio of W and Z production cross sections and the measured value of $\mathrm{Br}(Z \to \ell\ell) = \Gamma(Z \to \ell\ell)/\Gamma(Z)$. The value of σ_W/σ_Z obtained from the NNLO calculations provided by [12–16] is 3.3696 with associated relative uncertainties of 0.0056 coming from the PDF model and 0.0043 coming from electroweak and CKM matrix parameters used in the calculations (see section 8.3). The experimental value of $\mathrm{Br}(Z \to \ell\ell) = 0.033658 \pm 0.000023$ as measured at LEP is taken from [20].

When extracting $\mathrm{Br}(W \to \ell\nu)$ from R, it is important to consider correlated uncertainties in the ratio of predicted cross sections and the ratio of acceptances, A_Z/A_W, used in the measurement of R. In a sense, we measure $\mathrm{Br}(W \to \ell\nu)$ by equating R_{phys} to R_{meas}, where

$$R_{\mathrm{phys}} \equiv \frac{\sigma_W}{\sigma_Z} \frac{\mathrm{Br}(W \to \ell\nu)}{\mathrm{Br}(Z \to \ell\ell)} \tag{43}$$

and

$$R_{\mathrm{meas}} \equiv \frac{N_W^{\mathrm{obs}} - N_W^{\mathrm{bck}}}{A_W \epsilon_W} \frac{A_Z \epsilon_Z}{N_Z^{\mathrm{obs}} - N_Z^{\mathrm{bck}}}\,. \tag{44}$$

Then,

$$\mathrm{Br}(W \to \ell\nu) = \frac{N_W^{\mathrm{obs}} - N_W^{\mathrm{bck}}}{N_Z^{\mathrm{obs}} - N_Z^{\mathrm{bck}}} \frac{\epsilon_Z}{\epsilon_W} \times \left(\frac{A_Z \sigma_Z}{A_W \sigma_W}\right) \mathrm{Br}(Z \to \ell\ell)\,. \tag{45}$$

The ratio of the acceptance times the cross section for Z and W bosons on the right-hand side of equation (45) is affected by uncertainties in the PDF model. To account properly for correlations between the PDF uncertainties associated with each of these four quantities, we independently calculate a PDF model uncertainty for the quantity contained within the parentheses using the method described in section 5. The measured PDF model uncertainties on this quantity are found to be slightly larger than for those on A_Z/A_W alone (0.9% versus 0.6% in the electron channel and 1.0% versus 0.8% in the muon channel). These correlated uncertainties are separately accounted for in our extraction of $\mathrm{Br}(W \to \ell\nu)$ from the measured value of R. We obtain

$$\mathrm{Br}(W \to \ell\nu) = 0.1082 \pm 0.0022 \tag{46}$$

where the uncertainty contributions are from R (± 0.00212), the predicted ratio of cross sections (± 0.00047), and the $Z \to \ell\ell$ branching ratio (± 0.00007). The Standard Model value for this parameter is 0.1082 ± 0.0002, and the world average of experimental results is 0.1068 ± 0.0012 [20], both of which are in good agreement with our measured value. A summary of $\mathrm{Br}(W \to \ell\nu)$ measurements is shown in figure 36.

8.6.2. Extraction of $\Gamma(W)$. An indirect measurement of $\Gamma(W)$ can be made from our measured value of $\mathrm{Br}(W \to \ell\nu)$ using the Standard Model value for the leptonic partial width, $\Gamma(W \to \ell\nu)$. We use the fitted value for $\Gamma(W \to \ell\nu)$ of 226.4 ± 0.4 MeV [20]. Based on this value, we obtain

$$\Gamma(W) = 2092 \pm 42\,\mathrm{MeV} \tag{47}$$

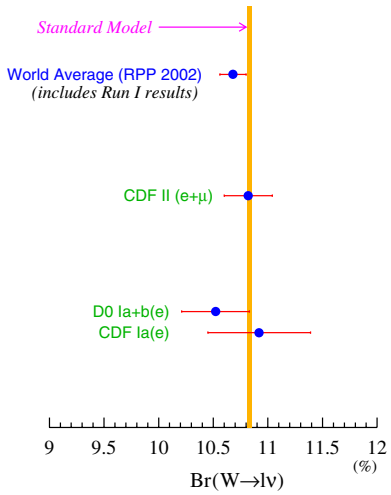

Figure 36. Comparison of our measured value of $\text{Br}(W \to \ell\nu)$ with previous hadron collider measurements [26, 27, 32], the current world average of experimental results [20], and the Standard Model expectation [20].

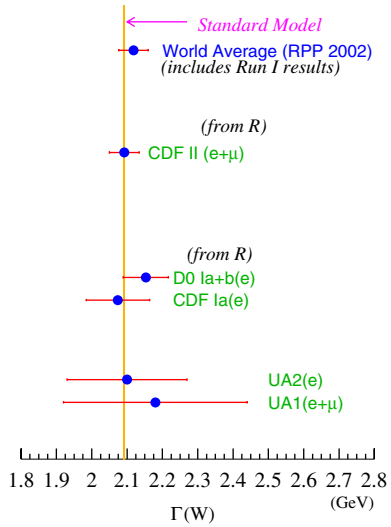

Figure 37. Comparison of our measured value of $\Gamma(W)$ with previous hadron collider measurements [26, 27, 32, 72, 73], the current world average of experimental results [20], and the Standard Model expectation [20].

which can be compared to Standard Model prediction of 2092 ± 3 MeV [20] and the world average of experimental results, 2118 ± 42 MeV [20]. A summary of $\Gamma(W)$ experimental measurements is shown in figure 37. Our indirect measurement is in good agreement with the fit [20] and the theoretical prediction as well as other measurements in literature.

An alternative approach for obtaining $\Gamma(W)$ is to first use the predicted values for both $\Gamma(W \to \ell\nu)$ and $\Gamma(Z \to \ell\ell)$ to extract a ratio of the total widths, $\Gamma(W)/\Gamma(Z)$, from

Table 43. Standard Model parameters extracted from the measured ratio of W and Z production cross sections, R.

Quantity	Our measurement	World average	SM value
$\mathrm{Br}(W \to \ell\nu)$	0.1082 ± 0.0022	0.1068 ± 0.0012	0.1082 ± 0.0002
$\Gamma(W)$ in MeV	2092 ± 42	2118 ± 42	2092 ± 3
$\Gamma(W)/\Gamma(Z)$	0.838 ± 0.017	0.849 ± 0.017	0.838 ± 0.001
V_{cs}	0.976 ± 0.030	0.996 ± 0.013	N/A
g_μ/g_e	0.991 ± 0.012	0.993 ± 0.013	1

the measured value of R. The precisely measured value of $\Gamma(Z)$ from the LEP experiments (2495.2 ± 2.3 MeV [20]) is then used to extract a value for $\Gamma(W)$. Using this approach we obtain

$$\frac{\Gamma(W)}{\Gamma(Z)} = 0.838 \pm 0.017 \tag{48}$$

for the ratio of total widths, which can be compared to the Standard Model prediction of 0.8382 ± 0.0011 [20]. Based on the measured value of $\Gamma(Z)$ we obtain

$$\Gamma(W) = 2091 \pm 42\,\mathrm{MeV}\,, \tag{49}$$

where the uncertainty on the measured value for $\Gamma(Z)$ makes a negligible contribution to the total uncertainty. Since the measurement of $\Gamma(Z)$ is independent of the measurement of the branching ratio $\mathrm{Br}(Z \to \ell\ell)$, both extracted values of $\Gamma(W)$ are independent to some degree.

8.6.3. Extraction of V_{cs}. In the Standard Model the total W width is a sum over partial widths for leptons and quarks where the latter subset involves a sum over certain CKM matrix elements [20]:

$$\Gamma_W \simeq 3\Gamma_W^0 + 3\left(1 + \frac{\alpha_s}{\pi} + 1.409\left(\frac{\alpha_s}{\pi}\right)^2 - 12.77\left(\frac{\alpha_s}{\pi}\right)^3\right)\sum_{[\mathrm{notop}]} |V_{qq'}|^2\Gamma_W^0. \tag{50}$$

Only the first two rows of the CKM matrix contribute as decays to the top quark are kinematically forbidden. Thus the relevant CKM matrix elements are V_{ud}, V_{us}, V_{cd}, V_{cs}, V_{ub}, and V_{cb}. Of these, V_{cs} contributes the largest uncertainty. We use the indirect measurement of $\Gamma(W)$ from our measured value of $\mathrm{Br}(W \to \ell\nu)$ as a constraint on V_{cs} based on world average measurements of all the other CKM matrix elements and find

$$|V_{cs}| = 0.976 \pm 0.030, \tag{51}$$

using $\alpha_s = 0.120$ and $\Gamma_W^0 = 226.4$ MeV [20]. Our measured value is more precise than the direct measurement at LEP, $|V_{cs}| = 0.97 \pm 0.11$ [74, 75], but not as precise as the combined value from LEP and Run I at the Tevatron, $|V_{cs}| = 0.996 \pm 0.013$ [76].

8.7. Summary

We have performed measurements for the W and Z boson production cross sections in the electron- and muon-decay channels based on 72 pb^{-1} of $p\overline{p}$ collision data at $\sqrt{s} = 1.96$ TeV. We calculate the ratio of the W and Z cross sections, R, in each lepton channel and combine them to obtain a value which is precise to 1.9%. The precision will improve when more data are analyzed. From this ratio we extract the leptonic W branching ratio, the W width, the ratio of the W and Z widths and constrain the CKM matrix element V_{cs}. A summary of extracted quantities is given in table 43.

Acknowledgments

We thank the Fermilab staff and the technical staffs of the participating institutions for their vital contributions. This work was supported by the US Department of Energy and National Science Foundation; the Italian Istituto Nazionale di Fisica Nucleare; the Ministry of Education, Culture, Sports, Science and Technology of Japan; the Natural Sciences and Engineering Research Council of Canada; the National Science Council of the Republic of China; the Swiss National Science Foundation; the AP Sloan Foundation; the Bundesministerium fuer Bildung und Forschung, Germany; the Korean Science and Engineering Foundation and the Korean Research Foundation; the Particle Physics and Astronomy Research Council and the Royal Society, UK; the Russian Foundation for Basic Research; the Comision Interministerial de Ciencia y Tecnologia, Spain; in part by the European Community's Human Potential Programme under contract HPRN-CT-2002-00292; and the Academy of Finland.

References

[1] Acosta D *et al* 2005 *Phys. Rev. Lett.* **94** 091803
[2] Weinberg S 1967 *Phys. Rev. Lett.* **19** 1264
[3] Salam A 1968 *Elementary Particle Theory: Relativistic Groups and Analyticity (Nobel Symposium No. 8)* ed N Svartholm (Stockholm: Almqvist and Wiksell) p 367
[4] Glashow S 1961 *Nucl. Phys.* **22** 579
[5] Arnison G *et al* 1983 *Phys. Lett.* B **122** 103
[6] Banner M *et al* 1983 *Phys. Lett.* B **122** 476
[7] Arnison G *et al* 1983 *Phys. Lett.* B **126** 398
[8] Bagnaia P *et al* 1983 *Phys. Lett.* B **129** 130
[9] The LEP Collaborations: ALEPH, DELPHI, L3 and OPAL, the LEP Electroweak Working Group and the SLD Electroweak and Heavy Flavor Working Group 2004 *Preprint* hep-ex/0412015
[10] Drell S and Yan T-M 1970 *Phys. Rev. Lett.* **25** 316
[11] Kubar J, Le Bellac M, Meunier J L and Plaut G 1980 *Nucl. Phys.* B **175** 251
[12] Sutton P, Martin A, Roberts R and Stirling W 1992 *Phys. Rev.* D **45** 2349
[13] Rijken R and van Neerven W 1995 *Phys. Rev.* D **51** 44
[14] Hamberg R, van Neerven W and Matsuura T 1991 *Nucl. Phys.* B **359** 343
Hamberg R, van Neerven W and Matsuura T 2002 *Nucl. Phys.* B **644** 403 (erratum)
[15] Harlander R and Kilgore W 2002 *Phys. Rev. Lett.* **88** 201801
[16] van Neerven W and Zijlstra E 1992 *Nucl. Phys.* B **382** 11
van Neerven W and Zijlstra E 2004 *Nucl. Phys.* B **680** 513 (erratum)
[17] Anastasiou C, Dixon L, Melnikov K and Petriello F 2004 *Phys. Rev.* D **69** 094008 (*Preprint* hep-ph/0312266)
[18] 't Hooft G 1973 *Nucl. Phys.* B **61** 455
[19] Bardeen W A, Buras A J, Duke D W and Muta T 1978 *Phys. Rev.* D **18** 3998
[20] Hagiwara K *et al* 2002 *Phys. Rev.* D **66** 010001
[21] Denner A and Sack T 1990 *Z. Phys.* C **46** 653
[22] Sirlin A 1980 *Phys. Rev.* D **22** 971
[23] Hollik W 1990 *Fortschr. Phys.* **38** 165
[24] Cabibbo N 1983 *3rd Topical Conference on Proton–Antiproton Collider Physics, Rome,* Jan 1983
[25] Abe F *et al* 1996 *Phys. Rev. Lett.* **76** 3070
[26] Abe F *et al* 1994a *Phys. Rev. Lett.* **73** 220
[27] Abe F *et al* 1995 *Phys. Rev.* D **52** 2624
[28] Abe F *et al* 1999 *Phys. Rev.* D **59** 052002
[29] Affolder T *et al* 2001a *Phys. Rev.* D **63** 011101
[30] Abachi S *et al* 1995 *Phys. Rev. Lett.* **75** 1456
[31] Abbott B *et al* 1999 *Phys. Rev.* D **60** 052003
[32] Abbott B *et al* 2000 *Phys. Rev.* D **61** 072001
[33] Affolder T *et al* 2001b *Phys. Rev.* D **64** 032002
[34] Kalinowski J and Zerwas P 1997 *Phys. Lett.* B **400** 112
[35] Blair R *et al* The CDF-II detector *Technical Design Report FERMILAB-PUB-96-390-E*

[36] Abe F *et al* 1988 *Nucl. Instrum. Methods* A **271** 387
[37] Abe F *et al* 1994b *Phys. Rev.* D **50** 2966
[38] Sill A *et al* 2000 *Nucl. Instrum. Methods* A **447** 1
[39] Affolder T *et al* 2004 *Nucl. Instrum. Methods* A **526** 249
[40] Pitts K T 1998 *Nucl. Phys. Proc. Suppl.* B **61** 230
[41] Bedeschi F *et al* 1988 *Nucl. Instrum. Methods* A **268** 50
[42] Balka L *et al* 1988 *Nucl. Instrum. Methods* A **267** 272
[43] Bertolucci S *et al* 1988 *Nucl. Instrum. Methods* A **267** 301
[44] Oishi R 2000 *Nucl. Instrum. Methods* A **453** 227
[45] Albrow M G *et al* 2002 *Nucl. Instrum. Methods* A **480** 524
[46] de Barbaro P *et al* 1995 *IEEE Trans. Nucl. Sci.* **42** 510
[47] Yasuoka K, Mikamo S, Kamon T and Yamashita A 1988 *Nucl. Instrum. Methods* A **267** 315
[48] Abe F *et al* 1993 *Phys. Rev.* D **47** 4857
[49] Apollinari G, Goulianos K, Melese P and Lindgren M 1998 *Nucl. Instrum. Methods* A **412** 515
[50] Ascoli G *et al* 1988 *Nucl. Instrum. Methods* A **268** 33
[51] Artikov A *et al* 2005 *Nucl. Instrum. Methods* A **538** 358
[52] Elias J *et al* 2000 *Nucl. Instrum. Methods* A **441** 366
[53] Acosta D *et al* 2001 *Nucl. Instrum. Methods* A **461** 540
[54] Winer B L 2001 *Int. J. Mod. Phys.* A **16S1C** 1169
[55] Anikeev K *et al* 2001 *Comput. Phys. Commun.* **140** 110
[56] Thomson E J *et al* 2002 *IEEE Trans. Nucl. Sci.* **49** 1063
[57] Ashmanskas B *et al* 2004 *Nucl. Instrum. Methods* A **518** 532
[58] Klimenko S, Konigsberg J and Liss T M Averaging of the inelastic cross sections measured by the CDF and the E811 experiments *FERMILAB-FN-0741*
[59] Sjöstrand T *et al* 2001 *Comput. Phys. Commun.* **135** 238 (*Preprint* hep-ph/0010017)
[60] Lai H L *et al* 2000 *Eur. Phys. J.* C **12** 375
[61] Affolder T *et al* 2000 *Phys. Rev. Lett.* **84** 845
[62] Dobbs M *et al* 2004 The QCD/SM Working Group: Summary Report *Preprint* hep-ph/0403100
[63] Brun R, Hagelberg R, Hansroul M and Lassalle J C 1978 GEANT: simulation program for particle physics experiments *User Guide and Reference Manual* CERN-DD-78-2-REV
[64] Agostinelli S *et al* 2003 *Nucl. Instrum. Methods* A **506** 250
[65] Grindhammer G, Rudowicz M and Peters S 1990 *Nucl. Instrum. Methods* A **290** 469
[66] Martin A D, Roberts R G, Stirling W J and Thorne R S 2004 *Eur. Phys. J.* C **35** 325
Stirling W J 2004 $\sigma_W \cdot Br(W \to \ell\nu) = 2.687 \pm 0.054\,\text{nb}$, $\sigma_Z \cdot Br(Z \to \ell\ell) = 251.3 \pm 5.0\,\text{pb}$ (using $Br(W \to \ell\nu) = 0.1068$ and $Br(Z \to \ell\ell) = 0.033658$) private communication
[67] Martin A D, Roberts R G, Stirling W J and Thorne R S 2003 *Eur. Phys. J.* C **28** 455
[68] Pumplin J *et al* 2002 *J. Help Energy Phys.* JHEP07(2002)012 (*Preprint* hep-ph/0201195)
[69] Acosta D *et al* 2005b *Phys. Rev.* D **71** 052003
[70] Lyons L, Gibaut D and Clifford P 1988 *Nucl. Instrum. Methods* A **270** 110
[71] Valassi A 2003 *Nucl. Instrum. Methods* A **500** 391
[72] Albajar C *et al* 1991 *Phys. Lett.* B **253** 503
[73] Alitti J *et al* 1990 *Z. Phys* C **47** 11
[74] Abreu P *et al* 1998 *Phys. Lett.* B **439** 209
[75] Barate R *et al* 1999 *Phys. Lett.* B **465** 349
[76] Renton P B 2002 *Rept. Prog. Phys.* **65** 1271 (*Preprint* hep-ph/0206231)